Diploma Thesis

Computational analysis of mechanical strains in mouse models of bone adaptation

submitted for acquiring the academic degree
“Diplom-Ingenieur” (equivalent to Master of Science)
at the Vienna University of Technology, Faculty of Civil Engineering

---

Diplomarbeit

Computergestützte Analyse mechanischer Beanspruchung in Knochenadaptionsmodellen von Mäusen

eingereicht zur Erlangung des akademischen Grades „Diplom-Ingenieur”
an der Technischen Universität Wien, Fakultät für Bauingenieurwesen

von

Paul Vallaster, BSc

Matr.Nr.: 01228069

unter der Anleitung von

Prof. Dipl.-Ing. Dr. **Ralph Müller**
Graeme Paul, MSc
Ariane Scheuren, MSc

Laboratory for Bone Biomechanics
Institute for Biomechanics
Eidgenössische Technische Hochschule (ETH) Zürich
Leopold-Ruzicka-Weg 4, 8093 Zürich, Schweiz

und

Dipl.-Ing. Dr. **Stefan Scheiner**

Institut für Mechanik der Werkstoffe und Strukturen
Technische Universität Wien
Karlsplatz 13/202, 1040 Wien, Österreich

Wien, im November 2019

Danksagung

Ich möchte mich bei allen bedanken, die mich in den letzten eineindrittel Jahren unterstützt haben und sich mein Gejammer regelmäßig angehört haben. Ich hatte nie Gedanken aufzuhören, auch wenn es vielleicht manchmal so gewirkt hat. Es hilft einfach sich manchmal die Ärgernisse von der Seele zu reden.

Danke an Ralph Müller und das gesamte Laboratory for Bone Biomechanics für die Möglichkeit an der ETH mitarbeiten zu dürfen und dabei einen sehr interessanten Einblick in den Alltag des wissenschaftlichen Arbeitens zu erlangen! Dieses wissenschaftliche Arbeiten durfte ich auch mit Stefan Scheiner weiterführen und konnte dadurch zusätzliche Perspektiven gewinnen. Danke an Ariane, Graeme und Stefan für die persönliche und hervorragende Betreuung!

Ein besonderer Dank gilt meiner Familie, FreundInnen, StudienkollegInnen und MentorInnen für den regen Austausch, welcher in den letzten sieben Jahren Studienzeit stattfand. Ohne diese Anregungen und Reflexionen wäre ich nicht der, der ich heute bin und hätte vielleicht in mancher mühsamen Zeit das Handtuch geworfen. Danke!

Kurzfassung

Knochengewebe passt sich an seine mechanische Umgebung an. Dies geschieht mittels Knochengewebeformation und -resorption. Ein besseres Verständnis dieser Knochengewebe(re)modellierung könnte zu besserem Verständnis von Krankheiten und gezielteren Behandlungen führen. Ziel dieser Arbeit ist es, den Einfluss von statischer und dynamischer Belastung auf die lokale Knochen(re)modellierung zu untersuchen.

Hierzu wurde der sechste Schwanzwirbel von 15 Wochen alten, weiblichen Mäusen *in vivo* mittels einer axialen Druckvorrichtung 4 Wochen lang belastet. Die Studie umfasste fünf Gruppen: scheinbelastet, statisch belastet, dynamisch belastet mit den Frequenzen 2 Hz, 5 Hz und 10 Hz. Die Knochenadaption wurde mittels *in vivo* Mikro-CT gemessen.

Morphometrische Parameter der Knochen wurden berechnet, um eine mögliche Frequenzabhängigkeit der Knochenadaption zu analysieren. Mechanische Größen (Verzerrungsenergiedichte und deren Gradient), welche als Maß für direkte, mechanische Belastung an Osteozyten betrachtet werden, wurden mit lokalem Knochen(re)modellierungsverhalten korreliert. Poromikromechanische Modelle wurden angewendet, um den Porendruck in den Lakunen und den Flüssigkeitsstrom in den Canaliculi zu untersuchen.

Die morphometrischen Parameter zeigten eine signifikant größere Adaption in den dynamisch belasteten Gruppen. Diese Ergebnisse deuten auf einen logarithmischen Zusammenhang zwischen Belastungsfrequenz und Knochenadaption hin. Höhere Werte der Verzerrungsenergiedichte und deren Gradienten führten zu einer erhöhten Formations- und verminderten Resorptionswahrscheinlichkeit. Trabekulärer und kortikaler Knochen zeigen leicht unterschiedliche Ansprechverhalten auf. Der ermittelte Porendruck in den Lakunen war größer als der hydrostatische Druck, der bekanntermaßen Knochenzellen stimuliert. Die berechneten Fließgeschwindigkeiten in den Canaliculi betrugen bis zu 120 μm/s, waren jedoch nicht hoch genug um eigenständig Knochenzellen zu stimulieren.

Zusammenfassend konnte gezeigt werden, dass eine dynamische Belastung notwendig ist, um Knochenadaption hervorzurufen. Um Letztere zu maximieren, sollte die Belastungsfrequenz im Bereich von 5–10 Hz liegen. Selten auftretende, stoßartige Belastung mit hohen Verzerrungsraten, könnte ein wichtiger Bestandteil von Knochenadaption sein. Hohe Verzerrungsraten führen zu hoher, direkter mechanischer Belastung und großem Porendruck in den Lakunen, was sich beides positiv auf die Knochenadaption auswirkt.

Abstract

Bone adapts to its mechanical environment by coupled (remodelling) and uncoupled (modelling) bone formation and resorption. A better understanding of bone (re)modelling could lead to insights into diseases and a more targeted disease treatment. The general objective of this thesis is to investigate the influence of static and dynamic mechanical loading on local bone (re)modelling behaviour.

To that end, the sixth caudal vertebrae of 15-week-old female mice were loaded *in vivo* by means of an axial compression device over the course of 4 weeks. The study consisted of five groups, which differed in type of loading: sham-loaded, static loading, dynamic loading with 2 Hz, 5 Hz, and 10 Hz. Bone adaptation was measured with *in vivo* micro-CT scans. Trabecular and cortical bone regions were analysed independently.

Bone morphometric parameters were computed to analyse a possible frequency dependency of bone adaptation. Mechanical quantities (strain energy density, SED, and its gradient), which are considered to be a measure of direct mechanical stress to an osteocyte, were correlated with local bone (re)modelling behaviour. Poromicromechanical models were applied to investigate lacunar pore pressure and canalicular fluid flow.

Bone morphometric parameters showed significantly greater adaptation in the dynamic-loading groups. These results suggest a logarithmic relation between loading frequency and bone adaptation. Greater SED and SED gradient values lead to an increase in formation and decrease in resorption probability. Trabecular and cortical bone show slightly different responses. The resulting lacunar pore pressure is greater than the hydrostatic pressure known to stimulate bone cells. The estimated canalicular fluid velocity is in the range of up to 120 μm/s, but not great enough to stimulate bone cells by itself. The underlying theoretical concepts of pore pressure and fluid flow could be combined with viscoelastic material behaviour to further study frequency or strain rate dependency.

In conclusion, it could be shown that dynamic loading is needed to induce bone adaptation.In order to maximize bone adaptation, a loading frequency from a certain range (5–10 Hz) is ideally applied. Infrequent impact loading with high strain rates could be a key component of bone adaptation. High strain rates cause greater direct mechanical strains and great lacunar pore pressure, which both influence bone adaptation positively.

Contents

Chapter 1

Introduction

1.1 Motivation

Load-bearing tissue in mammalian bodies consists of proteins and minerals. Although the basic building blocks are very similar, the force transmission requirements vary greatly. While tendons, ligaments and fasciae transfer tensile forces, bone and cartilage mainly have to resist compressive or shear forces. This leads to the notion that—depending on the type, amount and arrangement of these basic building blocks—tissues can have vastly different properties [1]. These differences also originate from the way the constituents are arranged on the micro- and nano-scale [2]. Bone tissue is therefore not a single material, but a hierarchical structure. Embedded in this structure are tissue-specific cells, which produce the structural proteins. The presence of cells allows regeneration and adaptation to changing environments. Thus, tissue cannot only be manipulated directly (intervention by extracellular matrix), but also indirectly (intervention by cells). As a result, biomechanics and biology cannot be investigated independently and possible interactions need to be considered.

Bone consists of an extracellular calcified matrix, containing collagen fibres, with several types of cells embedded in this matrix. It acts as a supportive structure for the body, protecting vital organs, storing calcium and phosphorus, and containing marrow for producing blood cells [3].

As shown as early as the 19th century by Julius Wolff, bone constantly adapts to its environment and remodels after damage (fracture). The adaptation process is known as Wolff's law and is described in his seminal book "The Law of Bone Remodelling" ("Das Gesetz der Transformation der Knochen") [4]:

> [T]*he law of bone remodelling is the law according to which alterations of the internal architecture clearly observed and following mathematical rules, as well as secondary alterations of the external form of the bones following the*

> *same mathematical rules, occur as a consequence of primary changes in the shape and stressing or in the stressing of the bones.*

Rephrasing this statement: Bone adapts to its mechanical environment by means of bone resorption and formation. The term bone modelling has been used to describe the adaptation of bone to its mechanical environment, i.e. *uncoupled* resorption and formation on distinct bone surfaces. It is typically observed during growth and adaptation of skeletal shape and size. Bone repair (or bone maintenance) involves the temporal and spatial *coupling* of resorption and formation. This is referred to as bone remodelling [5, 6]. As these processes can hardly be distinguished from each other in this thesis, the term (re)modelling is used to refer to both modelling and remodelling.

Bone (re)modelling is directed by the interaction of osteoblasts, osteoclasts and osteocytes. Osteoblasts are responsible for the addition of bone tissue, while osteoclasts act as antagonists removing bone tissue. These processes are directed by mechanically sensitive cells known as osteocytes [7, 8]. The interaction and activity of these cell types are sensitive to their biochemical and mechanical environment. These stimuli are coupled with hormonal, pathological and mechanical influences [9–13]. Comprehensive insights into bone (re)modelling are important for a better and more targeted disease treatment, e.g. regulation of disease-causing pathways or supply of extracellular matrix material.

The precise mechanical stimuli that are sensed by cells *in vivo* are not yet fully understood and are still a matter of ongoing discussions. Rosa et al. concluded that there is *"strong evidence favouring direct cell strain and interstitial fluid-flow as the most likely stimuli for mechanosensation"* [12]. Both have been extensively reported in the literature [14–20]. Additionally, it has been shown experimentally that hydrostatic pressure stimulates bone cells [21, 22] and that the required pressure could potentially arise in lacunar pores [23].

Efforts have been made to understand the propagation and amplification from macroscopic to microscopic strain, the *in vivo* mechanical environment and how cells experience this strain [24–26]. Poromicromechanics has been introduced to set up multiscale models, which allow e.g. calculation of fluid flow velocity and pore pressure across multiple length scales [23, 27–29].

Currently, the only way to study bone (re)modelling on the organ-scale is through *in vivo* studies. Bone adaptations over time need to be visualised and quantified, and can be tracked with a combination of staining and histology or using longitudinal micro-CT scans [39]. Stains and histologies are limited because they cannot detect sites of bone resorption, while micro-CT with sufficient resolution and registration algorithms allow investigation of those sites. Sites of bone resorption and formation and the change of bone micro-structure can then be directly linked to the present mechanical environment [40].

It is advantageous to alter the physiological environment in order to see adaptation, and hence studying the influence of the mechanical environment greatly benefits from *in* *vivo* loading. Several animal adaptation models for rodents have been established: many of these are non-invasive models that load the rodent's ulna or tibia [41–44]; others use exercise as mode of loading [45, 46]. Currently, two invasive models to study vertebrae are available [47, 48].

An advantage of direct *in vivo* mechanical loading are the controlled and repeatable mechanical forces which are applied to the bone. In contrast, in exercise studies the mechanical environment is more difficult to quantify and less well-controlled [49]. This is important when locally correlating a specific mechanical environment with bone (re)modelling. If the knowledge of the mechanical environment is scarce, assumptions and simplifications need to be made, leading to significant limitations for possible conclusions. Schulte et al. showed that local mechanical stimuli regulate bone (re)modelling [50]. The ability to locally predict bone (re)modelling via the mechanical environment is one of the primary goals in bone biomechanics.

Using the aforementioned loading models, influence of loading cycles, loading frequency, strain rate, and strain magnitude have been studied on the organ scale [42, 51–54]. Presuming a sufficient strain magnitude, frequency and bone adaptation have an inverted U-shaped relation with a greatest bone adaptation between 5–10 Hz (cortical bone) [54–56]. A similar relation for trabecular bone was hypothesised, which was the foundation for the study design laid out in Section 2.

Motivated by the notion that bone is a hierarchical structure and adaptations could originate from smaller scales, the multiscale paradigm formed in the 1990s, aiming to establish relations between micro-structural properties and processes on the macroscopic scale [30–32]. Subsequently, more developed multiscale models were established to describe bone tissue more precisely [27, 28, 33]. These models need to include and connect knowledge and experimental results from the molecule-, cell-, tissue- and organ-scale. Furthermore, multiscale models need to include and link various disciplines [34]. In bone research, the development of such models has been a focus in recent years, to ultimately increase the understanding of the *in vivo* mechanosensitive aspects and mechanisms of bone (re)modelling.

Furthermore, the advent of computers led to the suggestion that computer simulations may be employed in complement to experimental studies, for the sake of better-informed inter- and extrapolation of experimental data [27, 35–38]. Computer simulations indeed provide a cheaper, less time-consuming alternative. Simulations are able to connect mechanisms and findings on different scales and from different disciplines. Computational approaches allow for reasonable inter- and extrapolation of experimental results, and minimization of parameters which have to measured. While simulation of the behaviour of bone cannot replace experimental testing, it can be used as a complementary measure. In this way, computer simulations help explain or quantify results obtained experimentally, thereby working towards models which can predict bone adaptation in complex biochemical and mechanical environments. Thus, both multiscale models and computer simulations are effective counterparts to the traditional approach.

1.2 Objectives

The general objective of this thesis is to investigate the influence of static and dynamic mechanical loading on local bone (re)modelling behaviour. This is achieved by the following, more specific tasks:

- Establishment of an image processing and data analysis pipeline.
- Investigation of the influence of static and dynamic mechanical loading on bone adaptation (organ-scale).
- Adaptation and application of multiscale models estimating pore pressure and fluid flow.
- Correlation of mechanical quantities with local bone (re)modelling behaviour.

Chapter 2

Materials and experimental methods

This thesis is based on data from an experimental campaign conducted at the Laboratory of Bone Biomechanics, ETH Zürich, Switzerland.

2.1 Study design

All animal procedures were approved by the local authorities (Kantonales Veterinäramt Zürich, Zurich, Switzerland). In order to ensure consistent load application onto the sixth caudal vertebra (CV6), stainless steel pins were surgically inserted in the fifth and seventh caudal vertebrae of $N = 53$ 12-week-old female C57BL/6J mice (Charles River Laboratories). After three weeks of settling, loading was applied. The mice were split into five groups, differentiated by loading frequency. Several mice had to be excluded from the experiment due to swollen tissue around the pins. The group sizes for the analysis in this thesis are as follows: $N = 8$ for sham loading (control), $N = 8$ for static loading, $N = 7$ for dynamic loading at a frequency of 2 Hz, $N = 5$ for dynamic loading at a frequency of 5 Hz, and $N = 8$ for dynamic loading at a frequency of 10 Hz.

2.2 In vivo cyclic loading

For mechanical loading, pins were fixated in a previously developed caudal vertebral axial compression device (CVAD), see Fig. 2.1 [48]. The proximal pin was clamped tightly (such that subsequent movement of it was completely suppressed), while the distal pin was connected to a load cell which applied sinusoidal or constant forces at a peak load of 8.5 N, see Fig. 2.1(b) and 2.2. The loading frequency differed between groups: static (1 cycle, 5 min), 2 Hz (600 cycles, 5 min), 5 Hz (1500 cycles, 5 min), 10 Hz (3000 cycles, 5 min). This loading protocol was applied three times per week for four weeks for the loaded groups. For the control group (sham loaded), the mice were placed in the loading device under the same anaesthesia, but no loading was applied.

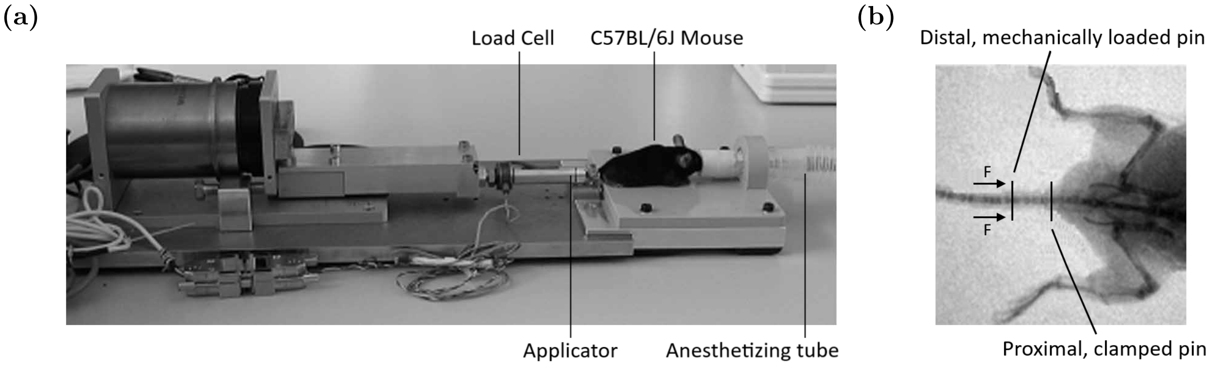

Fig. 2.1: **(a)** Photograph showing the caudal vertebra axial compression device, and **(b)** a fluoroscopic image of a mouse, graphically edited to show the location of the stainless steel pins. To achieve compression of a C6 vertebra, the mechanical signal was applied to the distal pin with the proximal pin being clamped. Reproduced from [48].

2.3 In vivo micro-computed tomography

In vivo micro-CT scans of CV6 were obtained at the start of loading for each group, and subsequently after 1, 2, 3, and 4 weeks. In this thesis, the five measurements are labelled "m1"-"m5". Changes between measurements or within a week are thus labelled "m1m2" (Week 1) ,"m2m3" (Week 2), "m3m4" (Week 3), and "m4m5" (Week 4). The vertebrae were scanned using high-resolution *in vivo* micro-CT (vivaCT 40, Scanco Medical AG, Brüttisellen, Switzerland). The nominal isotropic voxel resolution amounted to 10.5 μm. The scanner settings were chosen analogously to previous experiments [57], resulting in a resolution of the scanned region of $300 \times 300 \times 422$ voxels. Hence, the dimensions of the corresponding micro-CT representation amounted to $3.15 \times 3.15 \times 4.43$ mm.

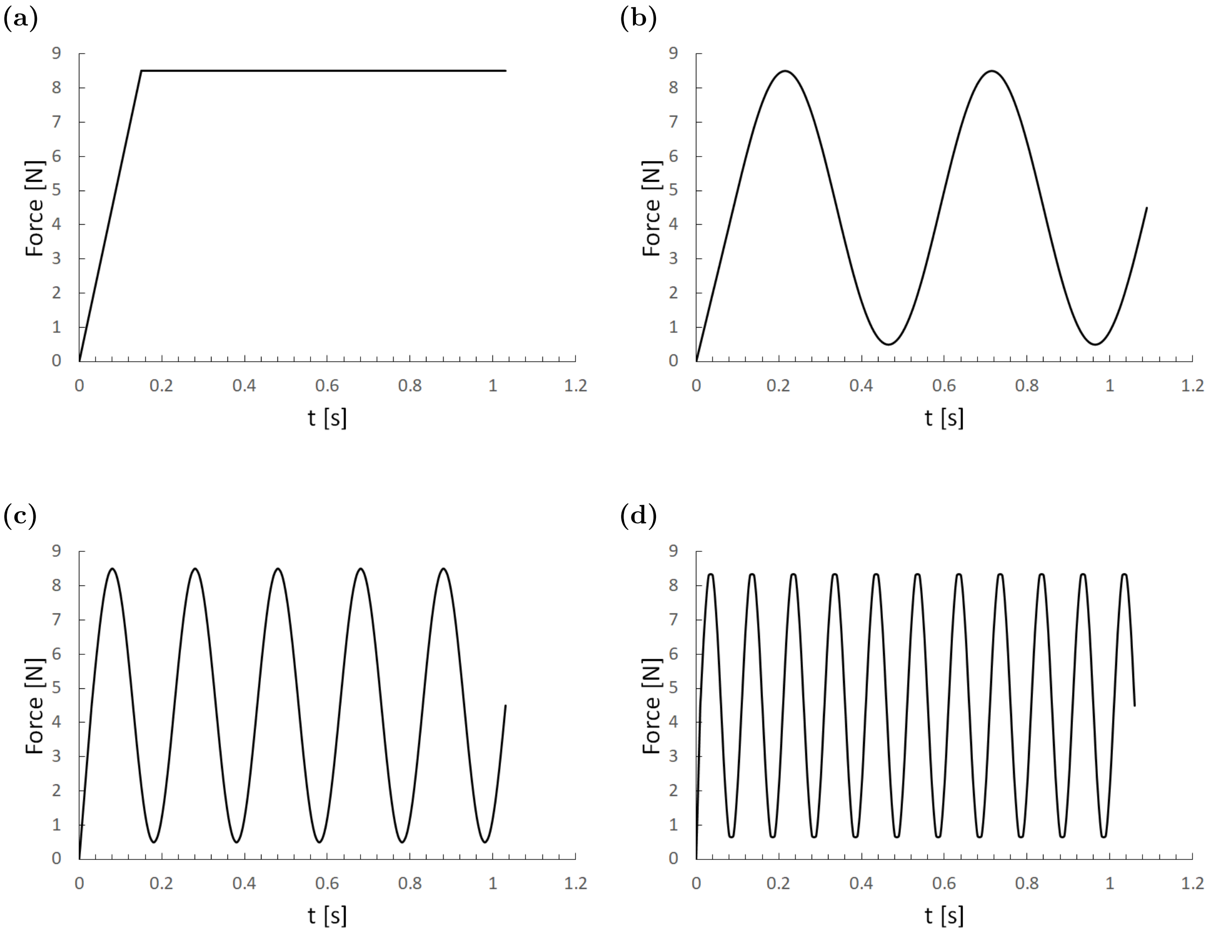

Fig. 2.2: Graphs showing the loading protocols of the analysed experimental campaign. **(a)** Static loading applied to murine vertebrae. **(b)** 2 Hz **(c)** 5 Hz **(d)** 10 Hz sinusoidal loading applied to murine vertebrae.

Chapter 3

Image processing

Micro-computed tomography (micro-CT) provides access to a three-dimensional field of Hounsfield units (directly interpretable as attenuation coefficients) throughout the scanned area. This (raw) data is usually compromised by noise, interference, artefacts, and misalignments [58]. In order to effectively exploit this data, e.g. in terms of a Finite Element (FE) analysis, a number of processing steps must be carried out. At the Laboratory of Bone Biomechanics an in-house script (OpenVMS/IPL) is used for that purpose. One of the aims of this thesis was to establish an image processing pipeline by using the programming language Python.

3.1 Process modalities

In the following, the names of specific openVMS/IPL in-house scripts and functions are explicitly mentioned for the sake of reproducibility, and to simplify future extensions and adaptations of the here-presented work at the Laboratory of Bone Biomechanics, ETH Zürich. The eventually produced Python-code is documented in the following internal repository:

`ifb_framework\projects\vertebrae_data_analysis` (30.01.2019)

Processing steps

In order to facilitate the equivalence between the new Python and the original open-VMS/IPL pipeline, the original image processing steps needed to be evaluated. If not explicitly noted otherwise, all necessary information on those steps can be found in the script `XIPL_EVAL_MEAS1.COM` and the logs of already processed images. These resources were used to evaluate the original pipeline. The steps of the pipeline to be newly established are chosen according to the original pipeline.

Stack misalignment correction

Due to the size of the vertebrae, the scans were subdivided into two stacks by the scanner. That is, the imaged vertebrae were split in half normal to the longitudinal axis of the spine. Between those two partial scans, the mouse holder on which the mice were placed during scanning was repositioned. This repositioning may cause translational or rotational displacements between the two image stacks, e.g. if the clamping of the tail was not sufficient. Therefore, a stack misalignment correction needed to be implemented.

The original stack misalignment correction registers the first slice of the second stack to the last slice of the first stack (script: `XIPL_EVAL_CORST.COM`, command: `/correct_stacks`). All other slices of the second stack are displaced and rotated accordingly. The stack misalignment correction only corrects three degrees of freedom, i.e. the two displacements within the transverse plane and one rotation around the longitudinal axis of the vertebrae. The other three degrees of freedom are neglected by the function. While displacements and rotations within the neglected degrees of freedom can and do indeed occur, scrutinizing this approach goes beyond the scope of this thesis. Notably, the number of overlapping slices varied between scans.

Gaussian filtering

In general, Gaussian filtering or Gaussian blur is obtained by convoluting an image with a kernel of Gaussian values [59]. 3D filtering is achieved by three orthogonal 1D convolutions. The input parameters need to be chosen according to the required filtering effect. A low-pass filter is used in order to reduce high-frequency noise without blurring the image and edges too much [40]. The key parameters are the size of the discrete Gaussian kernel (window) and the standard deviation (σ). In this work, the parameters are chosen analogously to previous studies: $\sigma = 1.2$ and a support of one voxel ($window\ size = 3 \times 1 \times 1$) [50, 57, 60–62]

Segmentation

For translating CT data into a clear, unambiguous model representation of the scanned object, thresholding-based segmentation is standardly carried out. Thresholding involves using a certain grey level threshold in order to separate the object into foreground (object of interest) and background voxels [63]. Thereby, the mode of thresholding depends on the specific goals and intended application of the respective study.

In the present case, two different thresholding modes were implemented. Firstly, a binary model representation is obtained from the CT-derived field of grey values, where a specific global threshold is chosen. All voxels exhibiting a grey value below the threshold are considered to be background voxels, whereas all voxels exhibiting a grey value larger than the threshold are considered to be foreground voxels, representing bone. Notably, when considering a binary model representation, the exact grey value of voxels with grey values above the threshold is disregarded. The second thresholding mode considered in this work actually takes into account the variability of grey values in the foreground voxels. This allows for assigning, in further consequence, a heterogeneous distribution of mechanical properties (due to a varying degree of mineralization between the voxels) to the object.

As explained above, a single global threshold is used for all vertebrae, requiring only one single parameter for segmentation (which renders this method also computationally efficient). However, a few problems may be encountered when using a single global threshold, concerning the accuracy and the difficulty in distinguishing between different types of bone (i.e., cortical and trabecular bone) [40, 64]. Trabeculae with low mineralization can be lost or appear unrealistically thin. Lowering the global threshold would, however, result in an overestimation of bone volume. More complicated alternatives are ruled out for this application because they lack superiority over simpler methods. The focus of this thesis is on the formation and resorption changes within one vertebra over time. Hence, a fixed global threshold allows longitudinal, site-specific comparisons between scans.

In particular argued by Bouxsein et al. [40], *"there is no consensus on a threshold that should be used for all studies, and extreme care must be taken when selecting a threshold..."* [40]. Furthermore, *"the methods for selecting this* [global] *threshold are not consistent between research groups, and are not always clearly communicated..."* [65]. The value for a global threshold is selected either qualitatively (requiring a substantial amount of experience in this respect), by analysing the histogram of CT data, or by forcing the resulting binary data set to have the same volume as the original bone sample (Archimedes' principle) [65, 66]. Clearly, basing the choice of the threshold on the grey-level histograms creates a sensitivity of the subsequent analysis not only on the absolute value of the threshold, but also on the region, or number of samples considered in the histogram [67, 68]. Nevertheless, the first of the two strategies described above, that is the histogram-based application, was utilized in the present investigation, and the threshold is chosen such that slight variations of it did not result in significant variations of the results presented later in this thesis. In particular, the openVMS pipeline uses a threshold of 580 $\mathrm{mg/cm^3}$ for all animals and measurements. In order to ensure best-possible comparability between the openVMS/IPL pipeline and the new pipeline developed in the here-presented work, the same threshold is considered.

Furthermore, an upper threshold for the grey-scale field is used to account for grey value outliers. Histograms are created which included all grey values between the global threshold (i.e. 580 $\mathrm{mg/cm^3}$) and the maximum value of the Gaussian-filtered image. The mean of the 95% percentiles of these histograms is reported as the maximum bone mineral density (BMD) [69].

Registration

Each mouse was scanned multiple times. For the calculation of bone resorption and formation, images of the same mouse need to be superimposable. This is achieved by image registration. To allow the correct application of normal force in the FE analysis, without adjusting the angle of force application, the longitudinal axis of the first scan is aligned to the corresponding z-axis of the image.

In the original openVMS image pipeline, the alignment is done automatically. The middle 20% of the Gaussian filtered, largest-component extracted first scan are used to align *"the long axis (line of* [minimum] *moment of inertia)"* with the z-axis. This algorithm is sequentially applied three times in total. The original, unfiltered image is then registered to the three times aligned image (`XIPL_EVAL_MEAS1.COM`). In the new Python pipeline, the alignment is executed with a principal component analysis (PCA). Voxels with a value smaller than 580 mg/cm^3 are ignored when computing the PCA. The grey-value information is used as weights. The first eigenvector (1st principal component) corresponds to the longitudinal axis of the vertebra. The whole vertebra is rotated so that the first eigenvector and the z-axis of the image are parallel. Frontal and sagittal axes are already aligned from the scanning and pre-processing in openVMS/IPL. The alignment with PCA is non-iterative and automatable, and the aligned image is used as the baseline image for the registration.

Subsequently, the first follow-up scan is registered to the baseline image. Instead of registering the second follow-up image to the baseline image, it is registered to the first follow-up and so forth. This improves accuracy when big morphometric changes are expected (e.g. disease, growth) [62]. The registration mask is the location of the reference and the unregistered vertebra, which lay closely together. The emerging gaps in the mask are closed with multiple dilation operations.

The registration in Python is executed by a modified Levenberg-Marquardt algorithm, with a non-linear least squares problem as an optimization criterion [70]. A pyramid method is used to downscale the image resolution depending on a pyramid level. Registration started on the highest level, which has the lowest resolution. The pyramid level is subsequently lowered, finally leading to a great decrease in optimization time. The results of the registration are the six parameters for a rigid transformation (three for rotation, three for translation).

Furthermore, efforts are made to overcome the limitations of the stack misalignment correction function. The two stacks/halves of the vertebrae are registered separately to their baseline images. After the registration, the two halves are put together and all six degrees of freedom are considered as possible error sources.

Material properties

The information about the Young's modulus is included in the processed images. A more detailed discussion on the selected values and presumed mechanical behaviour of bone can be found in Section 5.1. For the binary images, $E = 14.8\,\text{GPa}$ is chosen for all bone voxels [48]. The Young's modulus of the grey-scale image is calculated from its BMD [71]

$$E\ [\mathrm{GPa}] = 0.025 \cdot \mathrm{BMD}\ [\mathrm{mg/cm^3}] - 5.83 \tag{3.1}$$

Largest connected component

The images did not only contain information about the C6 vertebra, but also artefacts of the C5/C7 vertebrae. Connected-component labelling is used to establish the number and size of connected components. A 6-neighbour topology is used, where connected components had to share a face and each connected component gets labelled. The largest connected component is derived from the highest number of label occurrences. The chosen volume of interest (VOI) almost solely contains the vertebrae. Therefore, the largest connected component is classified as the vertebra. All other connected components are removed.

3.2 Results

Processing steps

Fig. 3.1 compares the original openVMS/IPL and the new Python pipeline. The only difference is that for practical reasons the order of registration and Gaussian filtering is interchanged. This interchange does not affect the results [72].

Equivalence cannot be evaluated solely by comparing the resulting images. The same image processing steps are executed by different functions. The introduction of an error cannot be excluded, therefore a stepwise comparison is necessary. If not stated otherwise, the steps are identical and generate the same image output.

openVMS pre-processing

The new Python pipeline is still dependent on openVMS/IPL, see Fig. 3.1(b). The scanners were operated with openVMS. The selection of the VOI is done with a function within openVMS. While the function for the stack misalignment correction only exists in openVMS, it can be called from Python, which saves an additional pre-processing step.

Stack misalignment correction

The outcome of the stack misalignment correction function can be shown best with an example. In Fig. 3.2(a) a translation between the halves of the vertebrae is visible. The magnitude of the misalignment can vary between scans from large to small or even non-existent (or, at least, negligible). The stack misalignment correction corrects the jump between the two stacks, see Fig. 3.2(b). The critical slice is fixated and is not changed between scans. This requires a precise choice and some pre-existing knowledge on the VOI.

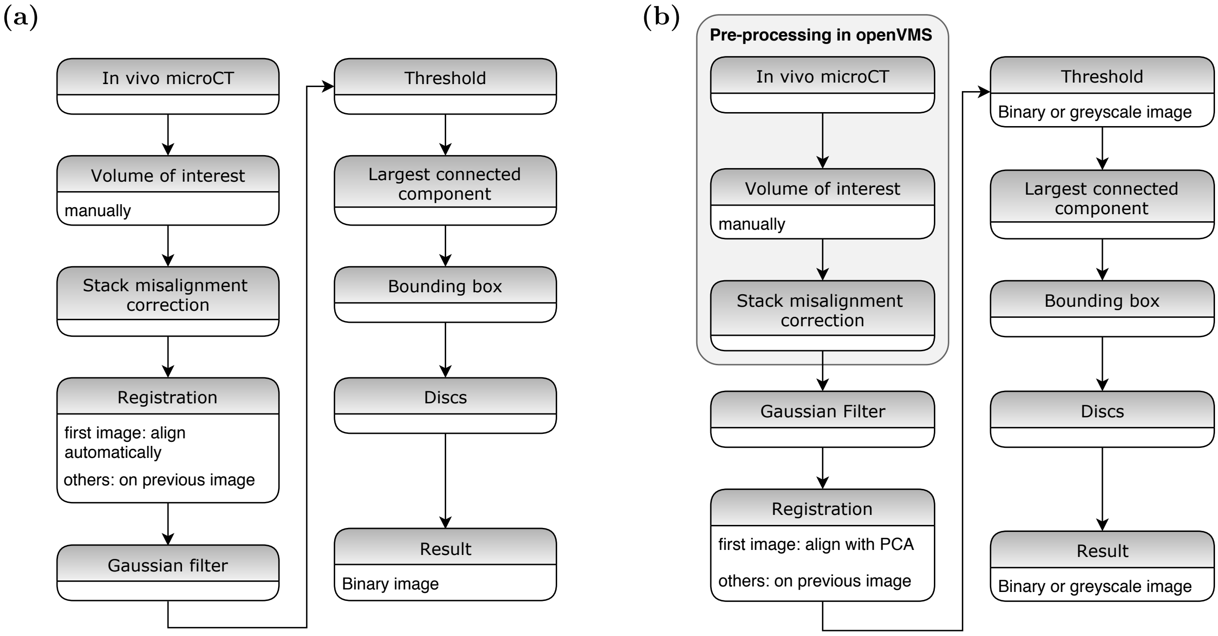

Fig. 3.1: Structure of the image processing pipelines in **(a)** openVMS/IPL and **(b)** Python.

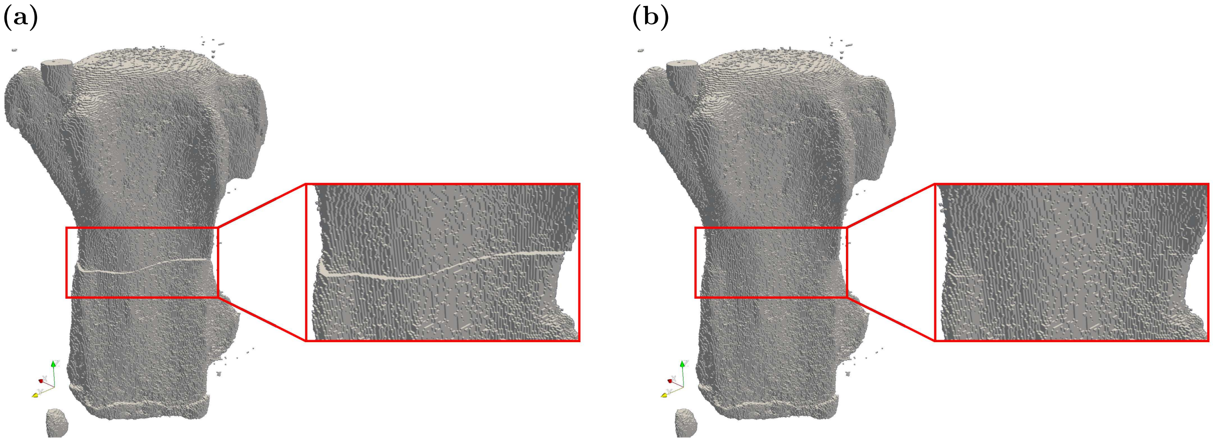

Fig. 3.2: Image of vertebra **(a)** before stack misalignment correction and **(b)** after misalignment correction.

Gaussian filtering

As expected, Gaussian filtering enables the reduction of noise without blurring the edges too much, see Fig. 3.3. The image is smoothed by reducing the peak values. The filtering is harder to see on smaller images, but becomes clearer when increasing the resolution.

The result of the Gaussian filtering in Python is slightly different from the one in openVMS/IPL. Although the images look similar, single voxels within the bone matrix differ. These voxels are thresholded as bone in Python, but not in openVMS. A possible explanation can be that the Gaussian filter in openVMS/IPL may be applied to the original scanner values and not the density values, which are calculated from the scanner values. Another reason can be rounding differences. The 3D filtering is executed by a sequence of one-dimensional convolution filters, from which only intermediate arrays are stored. The results may be imprecise because intermediate results are stored with insufficient precision. Even more differences occur when the Gaussian filter is applied to an array which is of float and not integer format.

The number of voxels for which this problem occurs is limited. From about 4×10^6 bone voxels, less than a thousand (1×10^3) are labelled differently. This difference should not have any influence on the results and is therefore neglected.

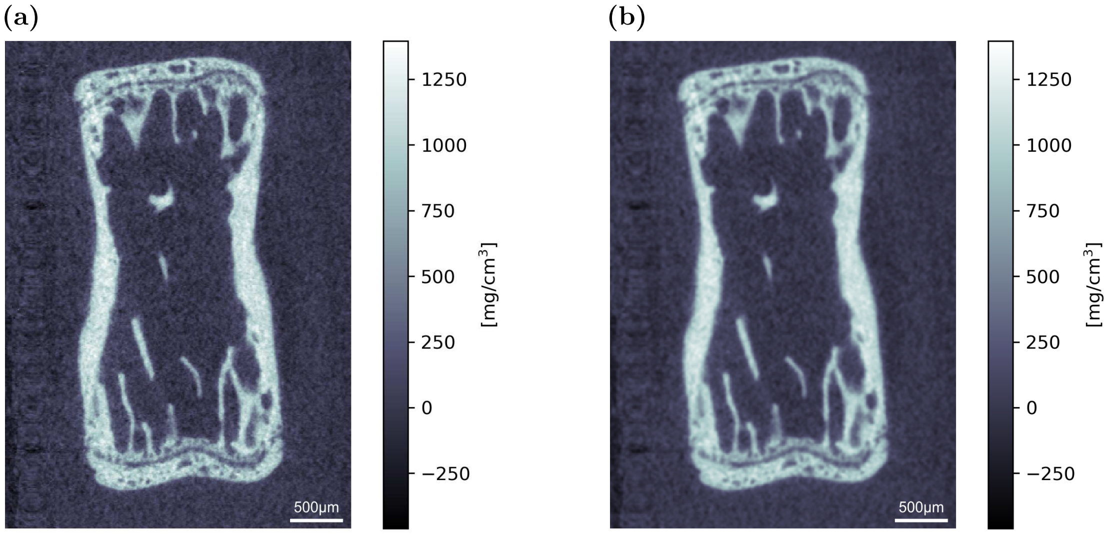

Fig. 3.3: Image of vertebra **(a)** before Gaussian filtering and **(b)** after Gaussian filtering.

Segmentation

The maximum BMD is established as 1182 mg/cm^3. Lower and upper global threshold for the grey-scale image are chosen as 580 and 1180 mg/cm^3. The values between the thresholds are assigned to classes with a bin width of 25 mg/cm^3. The results of the thresholding are shown in Fig. 3.4.

Registration

The automatic openVMS/IPL and Python alignment to the z-axis need to be compared. This is done by realigning the images aligned in openVMS/IPL by the PCA algorithm. The angles of the realignment are shown in Fig. 3.5. After the alignment, x- and y-axes lie in the transverse plane of the vertebrae. The x-axis is the frontal axis and the y-axis is the sagittal axes. The values are bimodally distributed, around zero, quite small and there is no bias for certain angles. The quality of the different alignment algorithms cannot be quantified.

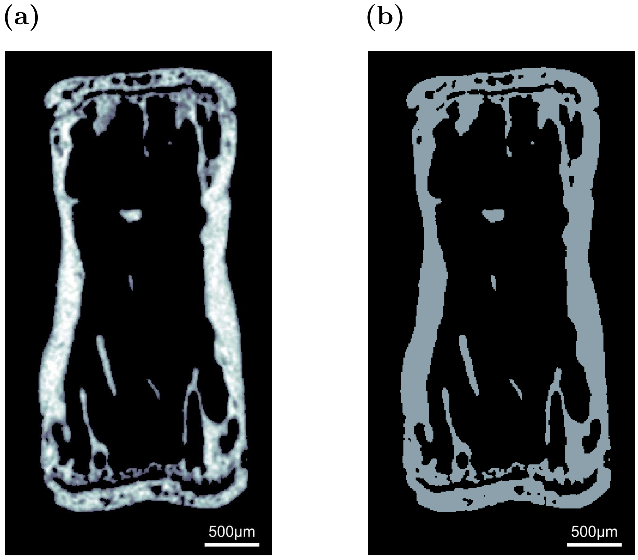

Fig. 3.4: Thresholded vertebra images **(a)** grey-scale image, lower threshold = 580 mg/cm^3, upper threshold = 1180 mg/cm^3, bin width = 25 mg/cm^3 and **(b)** binary image, threshold = 580 mg/cm^3.

When applying the new Python pipeline, some images—although registered correctly—show the tendency that a whole surface is labelled as bone resorption (violet) or formation (orange), see Fig. 3.6(a). This probably occurs due to the translational and rotational displacement between the two vertebra stacks. As this error is image-specific, similar errors are found in images processed with the original openVMS/IPL pipeline.

In some cases, the Python registration converges towards a visually inadequate solution, i.e. the images are not superimposed correctly. For these images, an additional step is added. Firstly, the largest connected component of the grey-scale, thresholded image is registered, which results in the six preliminary parameters for the rigid transformation. The direct application of these preliminary parameters to the actual image can lead to errors [72]. Therefore, the preliminary parameters are used as an initial guess for the registration of the actual, Gaussian-filtered image. After adding this additional step, all images converge towards a visually adequate solution. The method is verified with images which converge in both cases. Adding this registration step decreases the total amount of time needed for every image. It is therefore implemented in the new Python image processing pipeline.

The same procedure is used when registering the two halves separately. The result can be seen in Fig. 3.6. Visually, the registrations look similar. The problem that a whole surface is labelled as resorption (violet) or formation (orange) cannot be fully solved, see Fig. 3.6(b). In some cases, this way of registering causes a small gap between the two

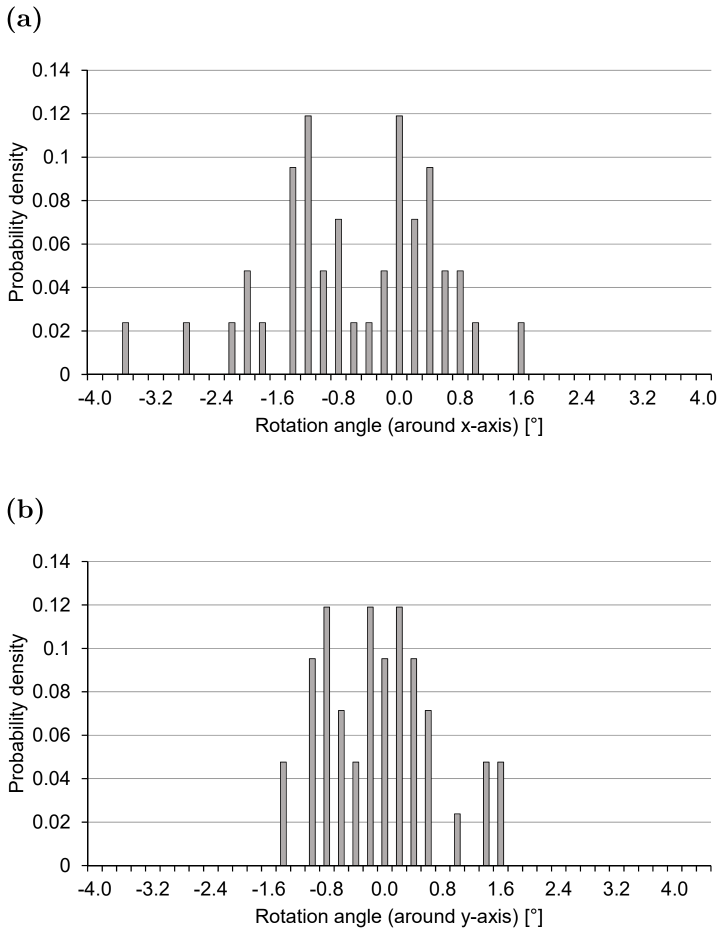

Fig. 3.5: Rotation angles between automatic openVMS/IPL and Python alignment of vertebrae. Histograms contain information about rotation angles around **(a)** the x-axis and **(b)** the y-axis. (After the alignment, x- and y-axes span the transverse plane of the vertebrae.)

halves of the vertebra. The gap is closed with a 1D maximum filter along the longitudinal axis (z-axis), $kernel\ size = 5 \times 1 \times 1$. In other cases the vertebra visibly grew within week m1m2, which is not possible to evaluate registering the two stacks separately. Whether this registration method makes a difference to further analysis or not cannot be established visually. Further analysis of this issue is conducted and described in Section 5.2.

Largest connected component

Artefacts from neighbouring vertebrae or other objects which are not part of the vertebra are successfully removed.

Bounding box and discs

In the last image processing step, the bounding box is cut and discs are added to the vertebra. The borders lie on the outermost voxel(s) in the z-direction. On both ends of

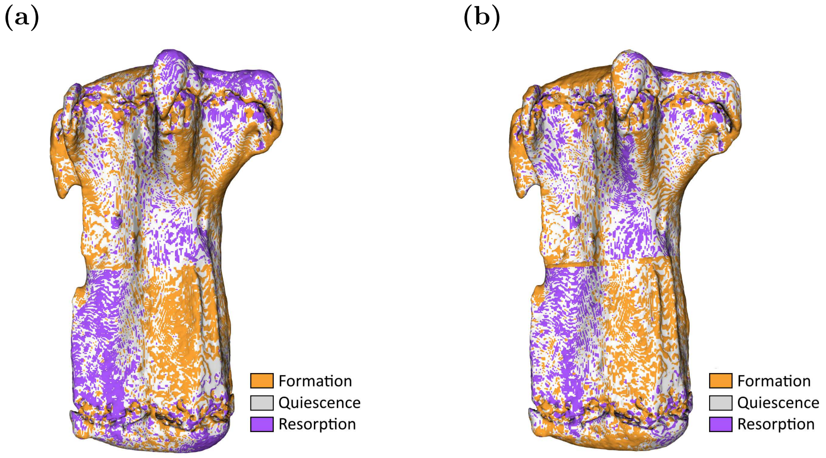

Fig. 3.6: Example of registration solution **(a)** registering the whole vertebra, and **(b)** registering the two halves separately.

the vertebra, 30 disc voxels are added in the z-direction. The number of bounding box voxels in the x- and y-direction are variable. The FE analyses for some images do not converge for a certain number of bounding box voxels. Therefore, the images need to be recreated with a different number of bounding box voxels. After several recreations every FE analysis converges. The Young's modulus of the discs is selected at $E = 14.8\,\text{GPa}$. Further discussion on this choice can be found in Section 5.1. Fig. 3.7 displays an example of the resultant binary and grey-scale image. The images are now ready for the FE analysis.

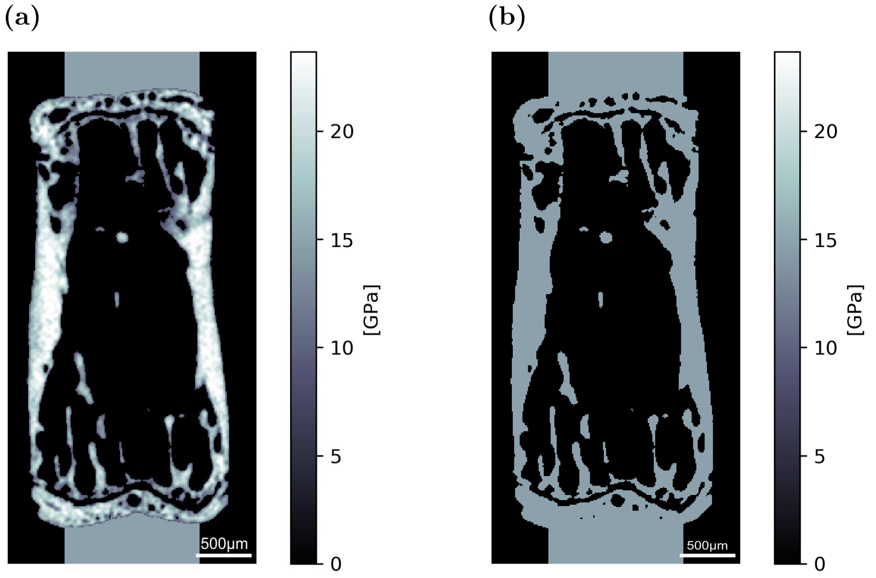

Fig. 3.7: Vertebra image processing results for Finite Element analysis **(a)** grey-scale image and **(b)** binary image.

Chapter 4

Frequency dependency of bone adaptation

4.1 Image data analysis methods

In the following, the names of specific openVMS/IPL in-house scripts and functions are explicitly mentioned for the sake of reproducibility, and to simplify future extensions and adaptations of the here-presented work at the Laboratory of Bone Biomechanics, ETH Zürich. The eventually produced Python-code is documented in the following internal repository:

`ifb_framework\projects\vertebrae_data_analysis` (30.01.2019)

Bone formation and resorption

Image registration allows for direct comparison of voxels in order to detect areas of bone formation and resorption. Resorption voxels are voxels which are labelled as bone in measurement m_n and background in measurement m_{n+1}. Formation voxels are voxels which are labelled as background in measurement m_n and bone in measurement m_{n+1}. Quiescent voxels are voxels which are labelled as bone in measurement m_n and m_{n+1}.

Bone regions

Owing to the diverse structures of trabecular and cortical bone, the mechanisms of bone adaptation might differ, and as a result they should not be analysed together. Additionally, different bone morphometric parameters are analysed when assessing the bone microstructure [40]. Mask images are created to cover the VOIs. In a mask image, voxels which belong to the VOI are set to 1 or “True” and voxels outside the VOI are set to 0 or “False”. The VOIs are chosen according to [60]. The bone adaptation mechanisms close to the growth plates are not well understood, most likely differ from other bone regions, and are therefore eliminated from the mask images. The mask images generated allow for independent analyses of trabecular and cortical bone at the same time.

The mask images for cortical and trabecular bone regions are originally created using openVMS/IPL (`XIPL_EVAL_MVER.COM`). The code from the original script (`XIPL_EVAL_OVMSK.COM`, `XIPL_EVAL_IVMSK.COM`, `XIPL_EVAL_CVMSK.COM`) is ported to Python. Original and new mask images are compared visually.

Bone morphometric parameters

Several parameters are considered for describing trabecular bone architecture and cortical bone morphology [40]. They provide quantitative snapshots of the current state and are calculated for each measurement "m1"-"m5". The parameters for trabecular bone are calculated using an evaluation function from openVMS/IPL (`/tri`). The images used for the parameter calculation are Gaussian filtered and segmented (see Section 3 for details). Additionally, the largest connected component is extracted. The parameters used to describe trabecular bone are:

- Bone volume (BV) present in VOI
- Total volume (TV) of the VOI
- Ratio of bone volume to total volume (BV/TV)

For cortical bone the parameters are:

- Cortical bone area (Ct.Ar)—average of cortical bone area per transversal slice (within the VOI)
- Total cross-sectional area inside the periosteal envelope (Tt.Ar)—average along the longitudinal axis (within the VOI)
- Cortical area fraction (Ct.Ar/Tt.Ar)
- Average cortical thickness (Ct.Th)

There is no standardised way to calculate the mean Ct.Th. In this work, it is done by packing the largest possible spheres in the cortical bone. Every bone voxel is assigned the diameter of the largest sphere covering it. The average of all voxels in the cortical bone region is considered the mean Ct.Th, which might be an overestimation, however, as larger spheres contain more bone voxels and are therefore weighted higher.

Bone dynamic morphometric parameters

The *dynamic* morphometric parameters quantify the bone adaptations which occur within a week/ between two measurements and are thus labelled "m1m2"-"m4m5". The idea of dynamic histomorphometric parameters is adapted to micro-CT scans [73]. The same dynamic parameters are calculated only for the trabecular bone region. The calculations only include changes within the specific VOI. The *dynamic* morphometric parameters are:

- Bone formation rate (BFR)—ratio of formed bone volume to baseline (m_n) bone volume per time interval.
- Bone resorption rate (BRR)—ratio of resorbed bone volume to baseline (m_n) bone volume per time interval.
- Mineralising surface (MS)—ratio of mineralising surface to bone surface. (When evaluating the surface of the formation volume, the type of neighbouring voxel is neglected. The absolute value of the mineralising surface is calculated by dividing the surface of the formation volume in half.)
- Eroded surface (ES)—ratio of eroded surface to bone surface. (When evaluating the surface of the resorption volume, the type of neighbouring voxel is neglected. The absolute value of the eroded surface is calculated by dividing the surface of the resorption volume in half.)
- Mineral apposition rate (MAR)—average distance between baseline (m_n) and follow-up (m_{n+1}) bone surface per time interval in regions of bone formation.
- Mineral resorption rate (MRR)—average distance between baseline (m_n) and follow-up (m_{n+1}) bone surface per time interval in regions of bone resorption.

Statistical analysis

The effects of time and loading regime on the bone structural parameters and dynamic bone parameters are determined through a linear mixed model. The between-subjects effect is the loading regime (no loading, static loading, dynamic loading with 2 Hz, 5 Hz, 10 Hz), while the within-subjects effects are time and time-group interactions. The subject ID is included as a random effect. If a significant time or group effect is observed, a post hoc analysis is conducted. This is done by pairwise comparisons among means using Tukey's HSD (honestly significant difference) test. Probability values (p-values) below 0.05 are considered statistically significant. Statistical analysis is performed with the software package R (R, Vienna, Austria).

4.2 Results

Bone regions

Although the code from the original script is translated line by line to Python, the achieved mask images are very similar but not identical. One reason for this disparity might be the lack of detailed information provided by openVMS/IPL. As it is a closed-source software, it is not possible to investigate the functions in detail, so small discrepancies between the used functions may exist.

The Python-created mask images visually cover the VOIs and are consistent over longitudinal measurements, see Fig. 4.1. The consistency is important for later ratio calculations. The Python-created mask images are therefore eligible to use for further calculations.

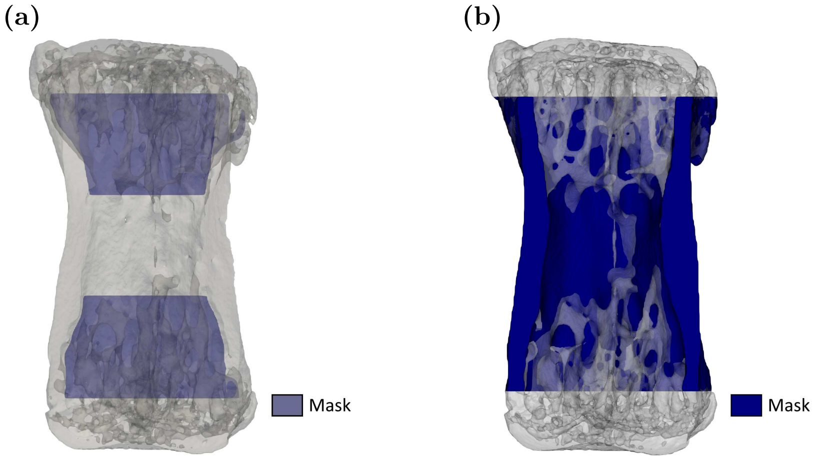

Fig. 4.1: Example of mask images (blue) of the **(a)** trabecular bone region and **(b)** cortical bone region.

Bone morphometric parameters—trabecular bone

The data containing the bone morphometric parameters in trabecular bone are provided in Supplementary Data S1.

Fig. 4.2(a) shows the change of the ratio of bone volume to total volume (BV/TV) over time, relative to BV/TV of the first measurement (m1). The dynamic-loading groups (2 Hz, 5 Hz, 10 Hz) experience a significant increase of BV/TV over time ($p < 0.001$ for m4 and m5 compared to m1). Notably, 5 Hz and 10 Hz already have a significant difference to its baseline (m1) at an earlier point in time (m3) ($p < 0.05$). The BV/TV of the sham-loading/control (CONT) and the static-loading (STAT) groups, on the other hand, does not change significantly over time. At the last measurement (m5), the 2 Hz, 5 Hz, and 10 Hz groups have a significantly higher adaptation than the CONT and STAT groups ($p < 0.001$), see Fig. 4.2(b). Although there is no significant difference between the CONT and STAT groups at m5, there is a slight tendency for a greater decrease in BV/TV for STAT. This hints towards the notion that static loading causes bone loss. Furthermore, no significant difference among the dynamic-loading groups can be seen. In Fig. 4.2(c), the relative change of the static- and dynamic-loading groups for m5 is plotted over the loading frequency, with STAT being plotted at 0.12 Hz to simplify the calculation of the non-linear regression line. Performing a regression analysis suggests a logarithmic bone adaptation response to loading frequency.

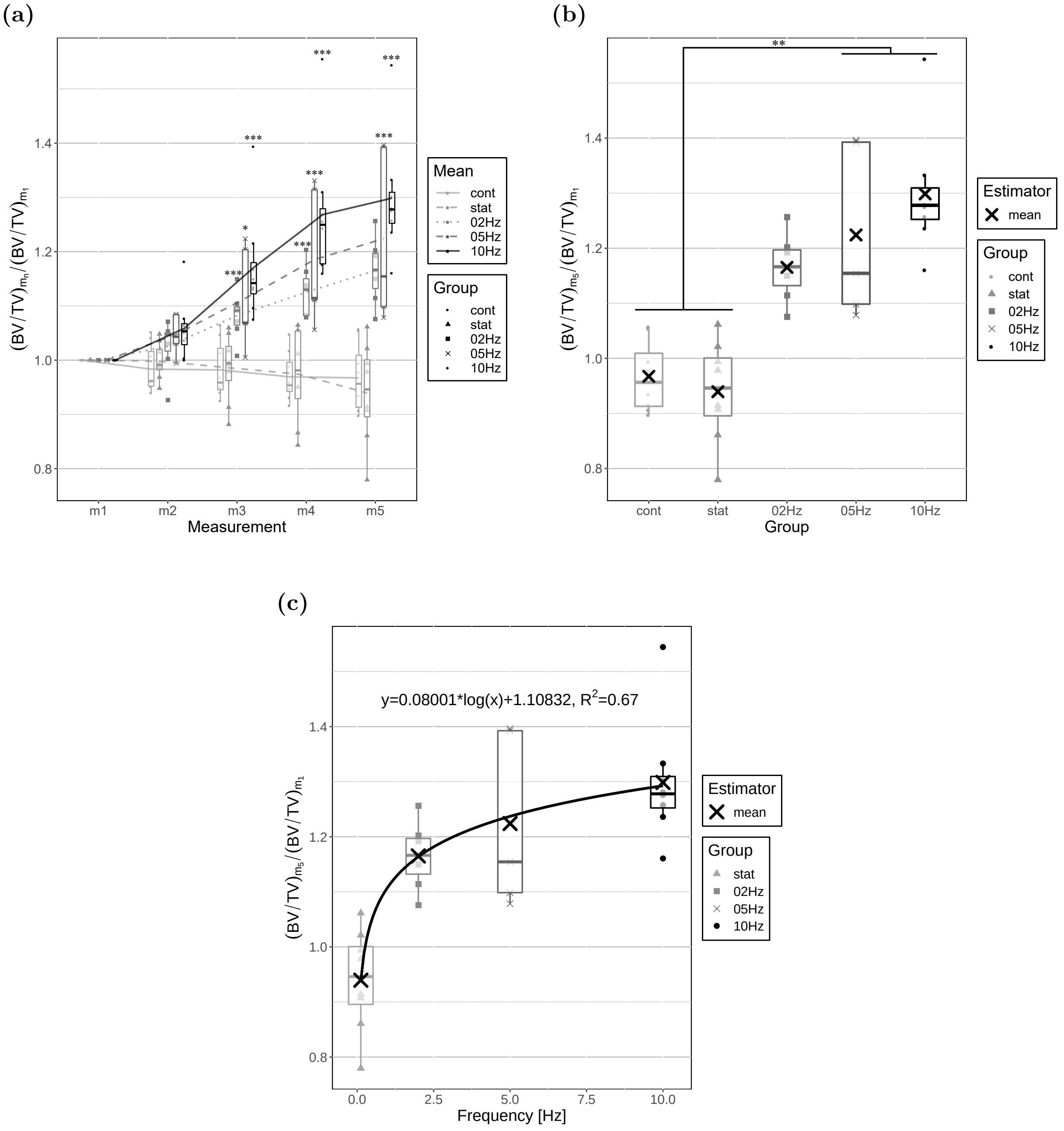

Fig. 4.2: Bone morphometric parameters in trabecular bone. **(a)** Relative change of ratio of bone volume to total volume (BV/TV) in trabecular bone for all measurements (Level of significance displayed for difference between m_1 and m_n within the group.) **(b)** Relative change of BV/TV at measurement m5 **(c)** Logarithmic regression line fitted to the relative change of BV/TV at measurement m5—(Levels of significance: * relates to $p < 0.05$, ** relates to $p < 0.01$, and *** relates to $p < 0.001$).

Bone dynamic morphometric parameters—trabecular bone

The data containing the bone dynamic morphometric parameters in trabecular bone are provided in Supplementary Data S2.

The values for the dynamic parameters correspond to the adaptations seen in the morphometric parameters. The only value which is excluded from the following analysis is 10 Hz, Mouse 6, week m1m2. In this case, the dynamic parameters do not match the observed bone volume adaptations.

For the CONT, STAT, 2 Hz, and 5 Hz groups, the bone formation rate (BFR) does not change significantly over time, see Fig. 4.3(a). Only 10 Hz causes a significant decrease of BFR in week m4m5 ($p < 0.01$, compared to the other groups). While the 10 Hz group seems to have a greater BFR in week m1m2, m2m3 and m3m4 than all other groups, this difference is not significant. The decrease of BFR in the last week suggests that most mice subjected to excitation at 10 Hz were already partially adapted to the present stimuli at m4, see Fig. 4.2(a). The bone resorption rate (BRR) does not change significantly over time, see Fig. 4.3(b). The BRR of the dynamic-loading groups is significantly lower than the BRR in the CONT and STAT groups ($p < 0.01$), indicating that dynamic loading has a strong influence on the BRR. There was no significant difference between the dynamic-loading groups.

Fig. 4.3(c) displays the difference between BFR and BRR (BFR-BRR), which can be described as net bone adaptation rate. BFR-BRR indicates whether there was overall bone gain or loss within the VOI. BFR-BRR does not change significantly over time in week m1m2, m2m3, and m3m4, see Fig. 4.3(c). Only in the 10 Hz group the decrease from m3m4 to m4m5 is significant ($p < 0.05$), which may be caused by the partial adaptations of the mice. Therefore, weeks m1m2, m2m3, and m3m4 are combined and fitted with a logarithmic regression line, see Fig. 4.3(d). There is a significant difference in BFR-BRR between the dynamic-loading groups and the other groups (CONT and STAT) ($p < 0.01$), as well as between the 2 Hz and the 10 Hz groups ($p < 0.05$). No significant difference between the 5 Hz and the other two dynamic-loading groups can be seen. The fitted regression line indicates that the net bone adaptation rate has a logarithmic dependency of loading frequency.

For mineral apposition rate (MAR) and mineral resorption rate (MRR), no time dependency can be seen, therefore all weeks are combined, see Fig. 4.4. There is no significant difference between the groups in MAR and MRR, see Fig. 4.4(a) and (b). This suggests that there is no influence of loading on MAR and MRR.

The mineralising surface (MS) can be interpreted as the amount of osteoblasts which were recruited, while the MAR describes how active single osteoblast units were. Similarly, the eroded surface (ES) quantifies the amount of suppressed osteoclasts, while MRR indicates the activity of single osteoclast units. For MS and ES, no time dependency can be seen,

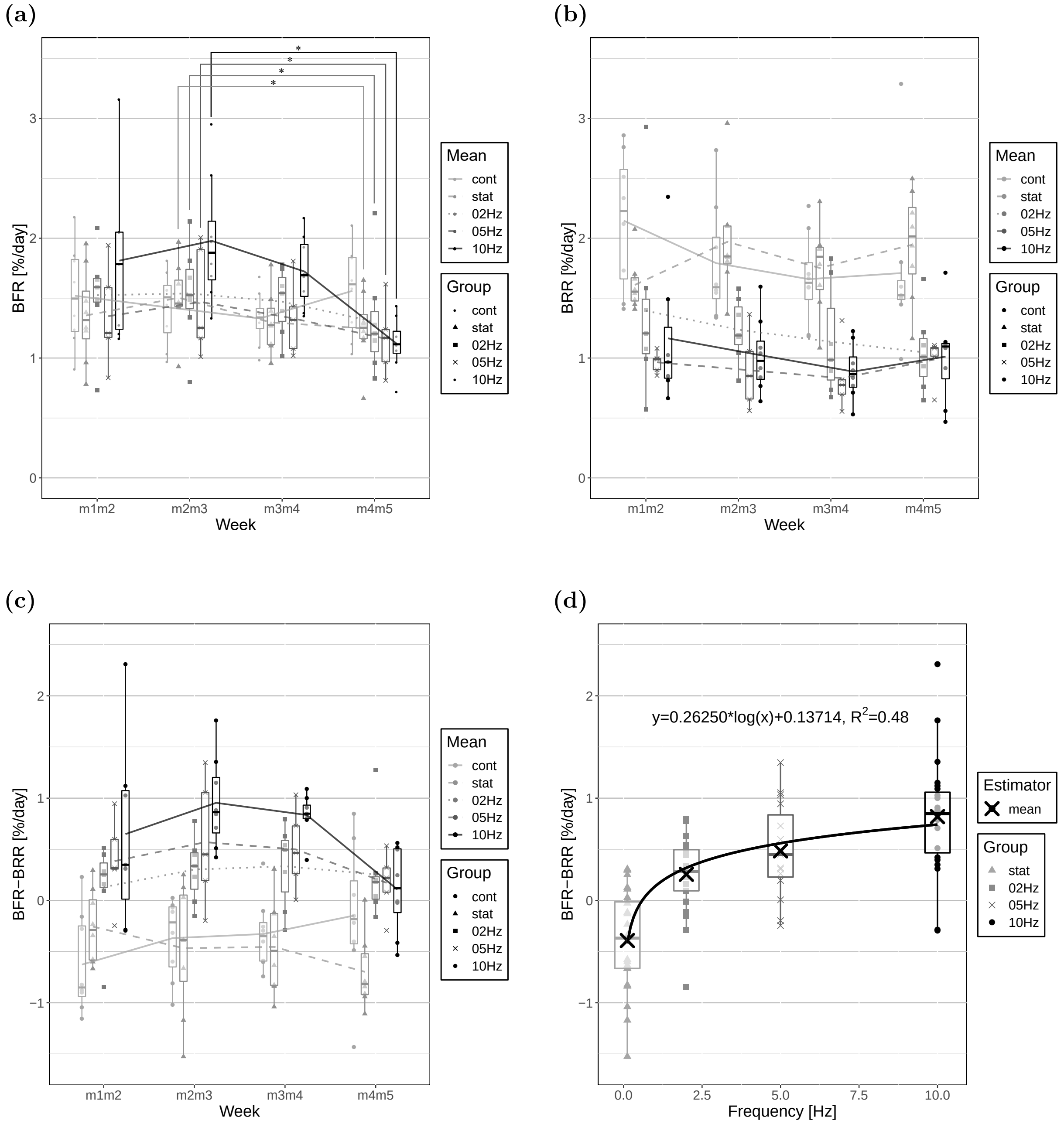

Fig. 4.3: Bone dynamic morphometric parameters in trabecular bone. **(a)** Bone formation rate (BFR) for all weeks **(b)** Bone resorption rate (BRR) for all weeks **(c)** Bone net adaptation rate (BFR-BRR) for all weeks **(d)** Combined BFR-BRR from measurements m1m2, m2m3 and m3m4, fitted with a logarithmic regression line—(Levels of significance: * relates to $p < 0.05$, ** relates to $p < 0.01$, and *** relates to $p < 0.001$)).

therefore all weeks are combined, see Fig. 4.5. There is a significant difference between the MS of the dynamic-loading and the other groups (CONT and STAT) ($p < 0.01$), see Fig. 4.5(a). While no significant difference within the dynamic-loading groups or

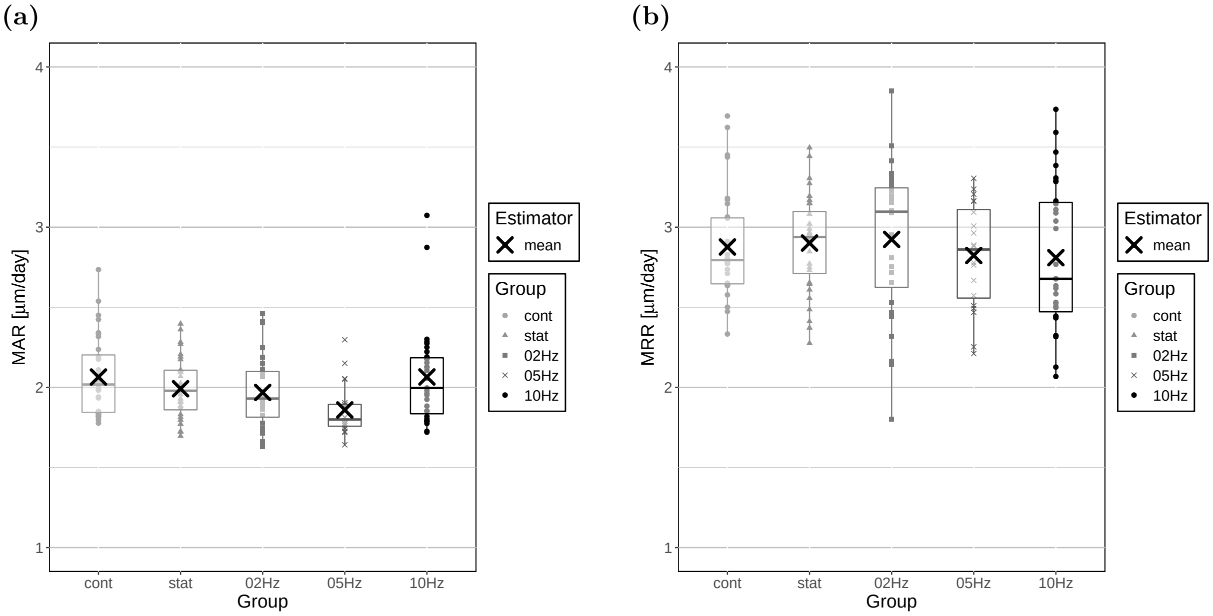

Fig. 4.4: Bone dynamic morphometric parameters in trabecular bone. **(a)** Mineral apposition rate (MAR) combined from all measurements **(b)** Mineral resorption rate (MRR) combined from all measurements (Levels of significance: * relates to $p < 0.05$, ** relates to $p < 0.01$, and *** relates to $p < 0.001$).

between the CONT and STAT groups can be found. For the ES, this observation is very similar, see Fig. 4.5(b), with a significant difference between the dynamic-loading and the other groups (CONT and STAT) ($p < 0.001$). Again, no significant difference within the dynamic-loading groups or between the CONT and STAT groups can be seen. This information suggests an influence of dynamic loading on mineralising and eroded surface. For further investigation the net active surface (MS-ES) is calculated and fitted with a logarithmic regression line. The logarithmic dependency on frequency is not as clear as with other parameters.

Possible correlations between the bone dynamic morphometric parameters are investigated with scatter plots and regression lines, see Fig. 4.6. There is no correlation between BFR-BRR and MAR or MRR present, see Fig. 4.6(a) and (b). However, a clear correlation between BFR-BRR and MS-ES is found, see Fig. 4.6(c). This correlation indicates that an increase in bone volume was driven by an increase in mineralising and decrease of eroded surface, rather than an increase of mineral apposition rate or decrease of mineral resorption rate.

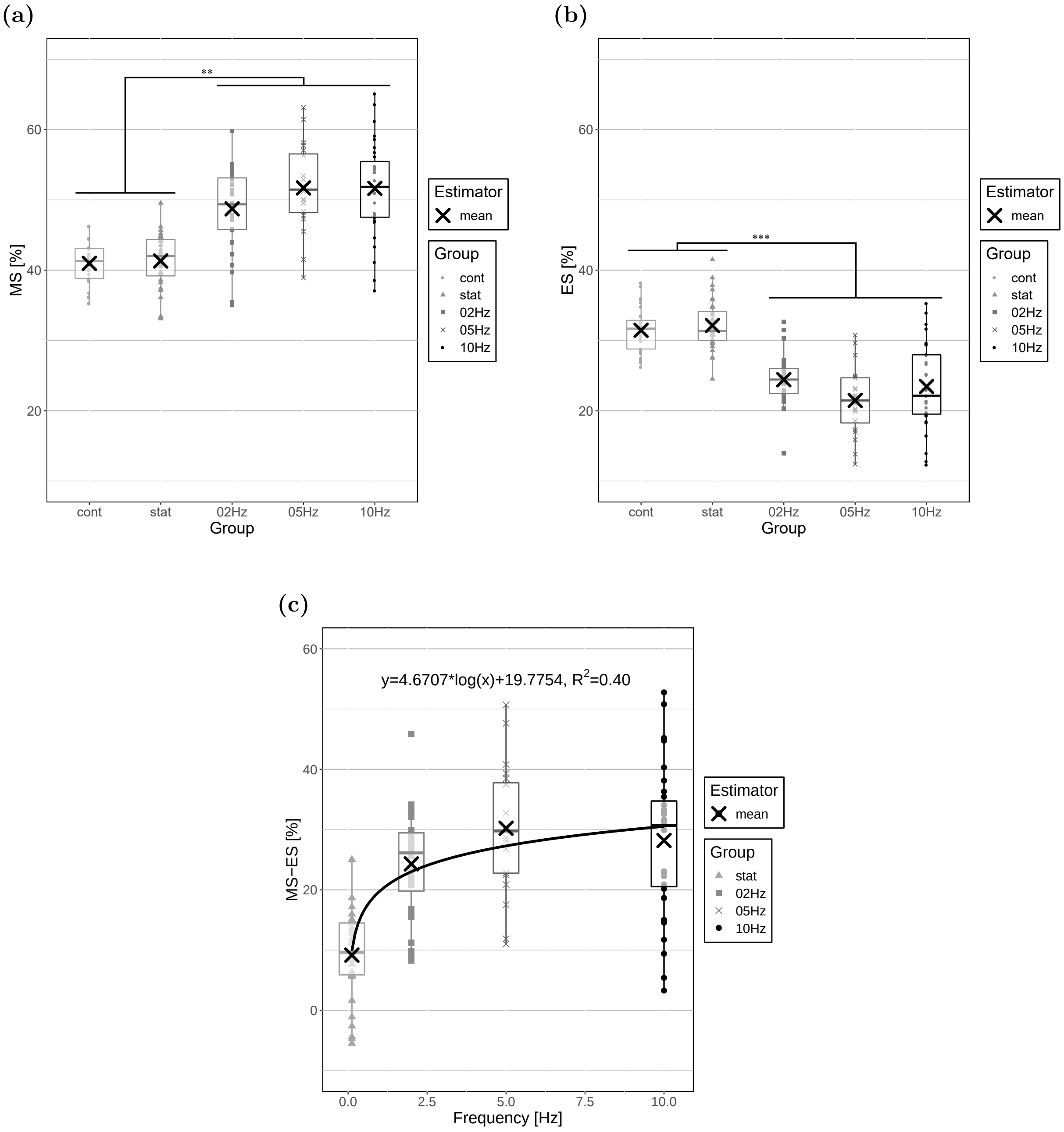

Fig. 4.5: Bone dynamic morphometric parameters in trabecular bone. **(a)** Mineralising surface (MS) combined from all measurements **(b)** Eroded surface (MS) combined from all measurements **(c)** Net active surface (MS-ES) combined from all measurements fitted with a logarithmic regression line (Levels of significance: * relates to $p < 0.05$, ** relates to $p < 0.01$, and *** relates to $p < 0.001$).

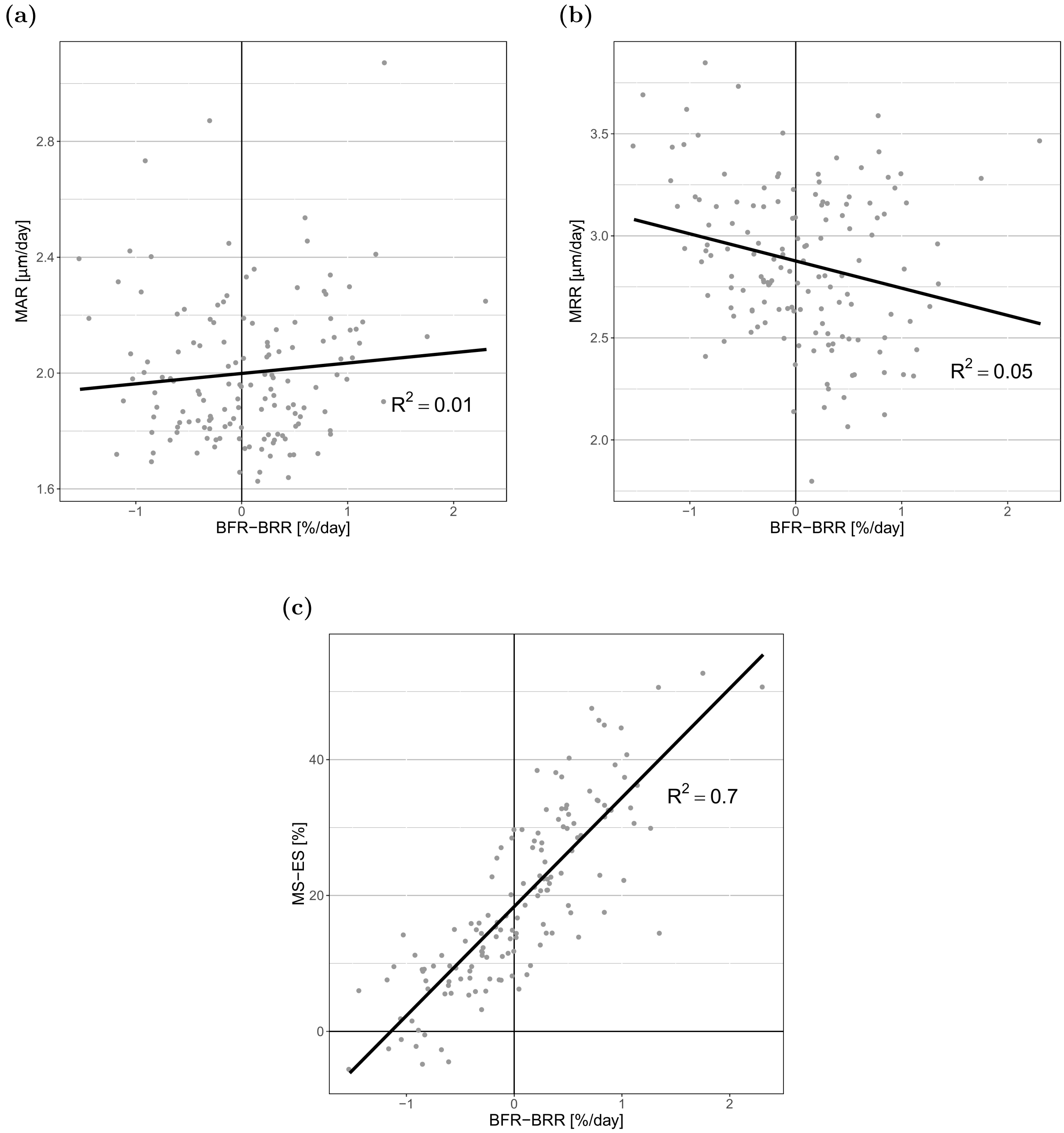

Fig. 4.6: Linear regression of bone dynamic morphometric parameters in trabecular bone. **(a)** Linear regression between net bone adaptation rate (BFR-BRR) and mineral apposition rate (MAR) **(b)** Linear regression between net bone adaptation rate (BFR-BRR) and mineral resorption rate (MRR) **(c)** Linear regression between net bone adaptation rate (BFR-BRR) and net active surface (MS-ES).

Bone morphometric parameters—cortical bone

The data containing the bone morphometric parameters in cortical bone is displayed in Supplementary Data S3. The calculated dynamic morphometric parameters do not appear to be correct, as the data contained severe inconsistencies. Some of the dynamic morphometric parameters require surface analyses. A possible explanation may be the registration problems described in Section 3.2, where a whole surface of a vertebra is labelled as formation or resorption. This problem cannot be solved with computational methods. Other possible sources of error could not be ruled out. Therefore, this data was not analysed.

The change in cortical area fraction (Ct.Ar/Tt.Ar) over time is displayed in Fig. 4.7(a). Again, no significant change within the sham-loading (CONT) and static-loading (STAT) groups over time can be seen. The increase of Ct.Ar/Tt.Ar in the dynamic-loading groups is significant from measurement m3 onwards ($p < 0.001$, exception 2 Hz-m3 $p < 0.05$). In every measurement, the 5 Hz group shows a tendency for greater adaptation compared to the 10 Hz group. The greater adaptation of the 5 Hz group is also present at m5, see Fig. 4.7(b). Whether this is a result of the small number of samples ($N = 5$), one high responder in the 5 Hz group, lower baseline parameter values at m1, or a different response to frequency in cortical bone, cannot be established at this point. In general, the dynamic-loading groups have a significantly higher increase of Ct.Ar/Tt.Ar at m5 compared to the CONT and STAT groups ($p < 0.05$). The fitted logarithmic regression line, see Fig. 4.7(c), does not reveal the same dependency as in BV/TV. However, the absence of the high responder in the 5 Hz group would lead to a better fit and the mean being much closer to the actual regression line.

A similar pattern can also be seen for the change of average cortical thickness (Ct.Th) over time, see Fig. 4.8(a). The increase of Ct.Th in the dynamic-loading groups is significant from measurement m2 onwards ($p < 0.001$). Although a slight increase within the CONT and STAT groups can be seen, this is not significant. The adaptation is again greater in the 5 Hz group compared to the 10 Hz group, see Fig. 4.8(b). The high response of one mouse is still present, but closer to the other data points. A logarithmic relation is not investigated for the cortical thickness parameter because of the way it is calculated. Fig. 4.8(b) and 4.7(b) suggest that the frequency dependency of bone adaptation in cortical bone is different to trabecular bone.

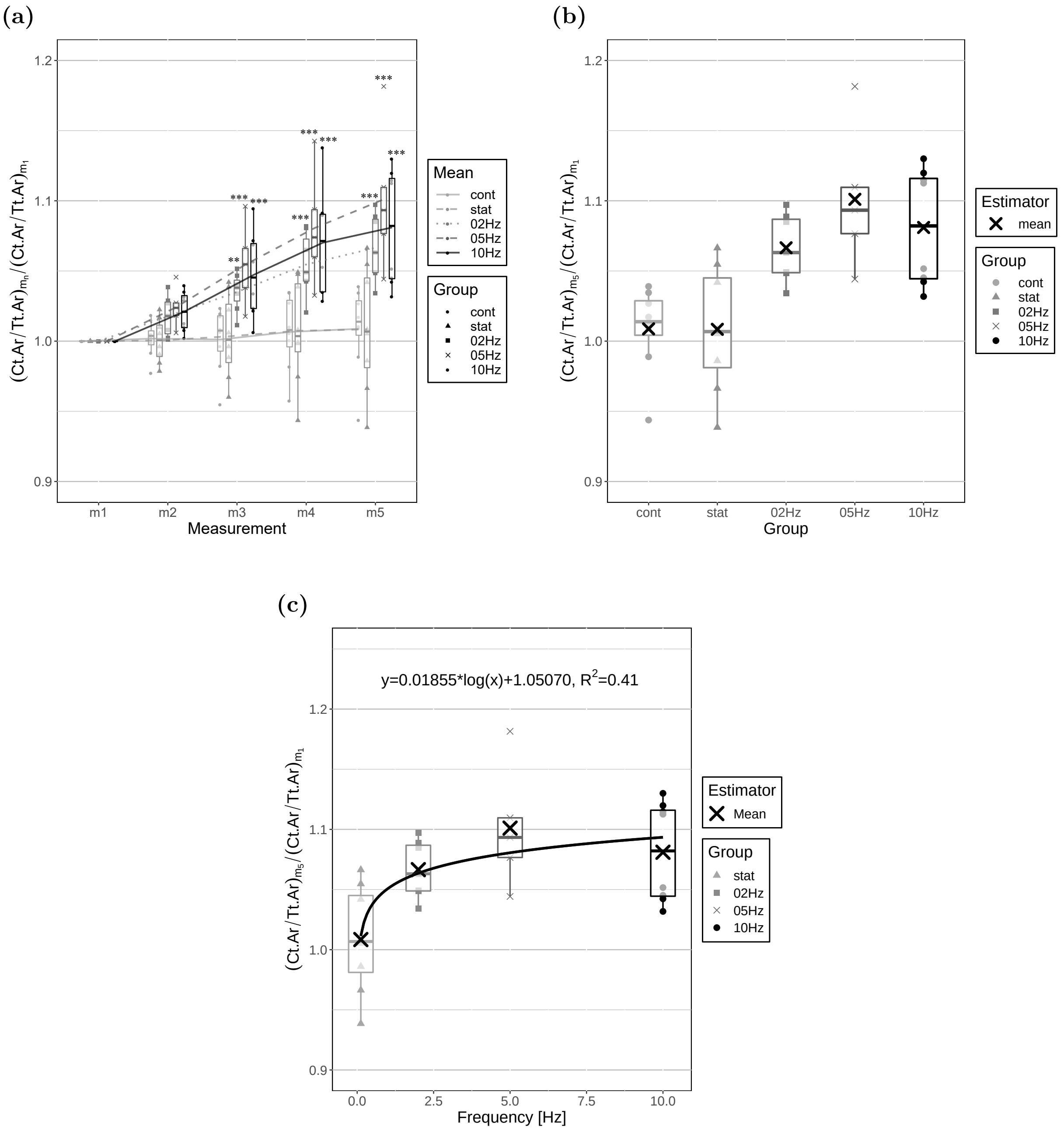

Fig. 4.7: Bone morphometric parameters in cortical bone. **(a)** Relative change of cortical area fraction (Ct.Ar/Tt.Ar) in cortical bone for all measurements (Level of significance displayed for differences between m_1 and m_n within the group.) **(b)** Relative change of Ct.Ar/Tt.Ar at measurement m5 **(c)** Logarithmic regression line fitted to the relative change of Ct.Ar/Tt.Ar at measurement m5—(Levels of significance: * relates to $p < 0.05$, ** relates to $p < 0.01$, and *** relates to $p < 0.001$).

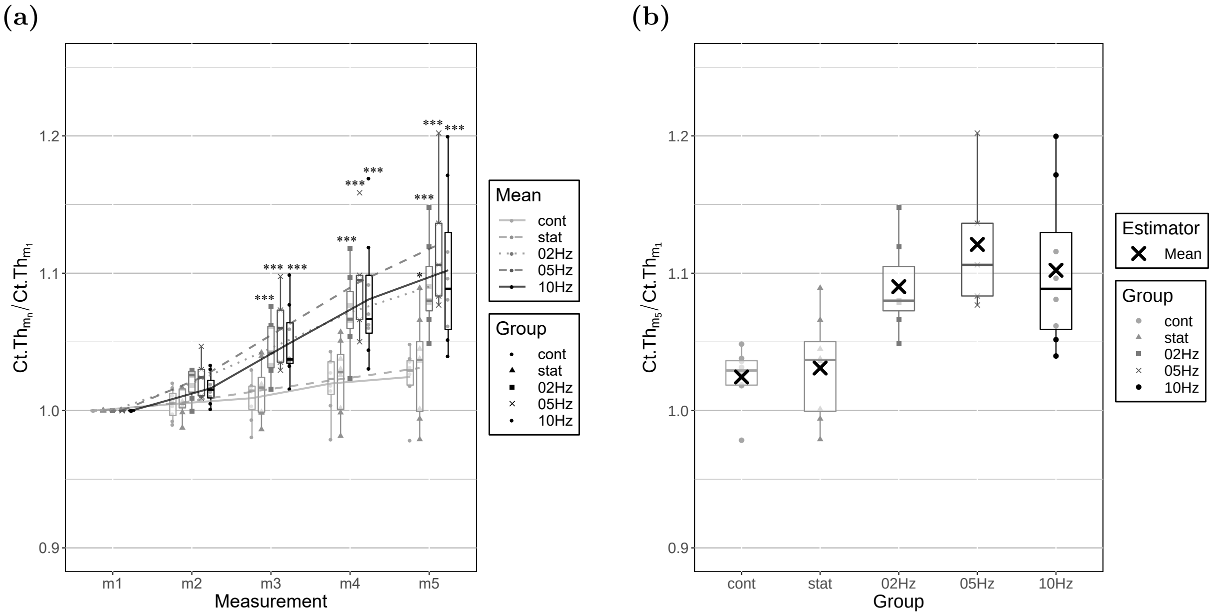

Fig. 4.8: Bone morphometric parameters in cortical bone. **(a)** Relative change of cortical thickness (Ct.Th) in cortical bone for all measurements (Level of significance displayed for difference between m_1 and m_n within the group.) **(b)** Relative change of Ct.Th at measurement m5—(Levels of significance: * relates to $p < 0.05$, ** relates to $p < 0.01$, and *** relates to $p < 0.001$).

Chapter 5

Correlation of strain energy density and its gradient with local bone (re)modelling behaviour

5.1 Theoretical concepts

In the following, the names of specific openVMS/IPL in-house scripts and functions are explicitly mentioned for the sake of reproducibility, and to simplify future extensions and adaptations of the here-presented work at the Laboratory of Bone Biomechanics, ETH Zürich. The eventually produced Python-code is documented in the following internal repository:

`ifb_framework\projects\vertebrae_data_analysis` (30.01.2019)

Finite Element analyses

3D micro-Finite Element (FE) models are created by converting all voxels of the image into eight-node hexahedral finite elements, with the resulting computational mouse models consisting of approximately 1.8 to 2.3 million elements. As for the mechanical properties assigned to the finite elements, two approaches are pursued. On the one hand, all finite elements are considered to exhibit the same mechanical properties: a Young's modulus of $E = 14.8\,\mathrm{GPa}$ and a Poisson's ratio of $\nu = 0.3$ are assigned to the bone tissue [48]. To model the intervertebral discs, additional voxels are added to the proximal and distal ends of the vertebra. This also prevents unrealistically high strains in a few nodes of the FE mesh. The discs have a circular cross-sectional area of $1.7\,\mathrm{mm}^2$ and a height of up to 10% of the full vertebral length, i.e. 30 voxels. In order to avoid convergence problems of the FE solver, the voxels representing the intervertebral discs are considered to exhibit the same material properties as bone, i.e. a Young's modulus of $E = 14.8\,\mathrm{GPa}$ and a Poisson's ratio of $\nu = 0.3$. The voxels representing the background (representing the space around the studied bone organ) are set to a Young's modulus of $E = 3\,\mathrm{MPa}$. This way, the background is considered to be substantially less stiff than the bone organ without compromising the results—assigning zero-stiffness to these voxels was not accepted by the FE solver used in this work.

Optionally the FE analyses are performed using variable Young's moduli estimated according to Eq. (3.1). The goal of this approach is to take into account the voxel-specific density-dependence of the Young's modulus [71, 74].

The bone is assumed to exhibit linear elastic material behaviour, which allows for static loading in the FE analysis [75]. A deformation of 1% of the length in the z-direction (longitudinal axis) is applied. The results are then rescaled to an applied force of 8 N for the dynamic- and static-loading groups and 4 N (physiological loading) for the sham-loading (control) group [76]. Displacement-controlled FE analyses are preferred, because the input dataset for the FE solver specifies the displacement or load for every node separately [77]. As the nodal forces and displacements cannot be estimated beforehand, the applied uniform displacement leads to a more realistic pressure distribution at proximal and distal surface voxels.

The FE model is solved using ParOSol, a micro-FE solver [77]. The calculations took 10 to 15 minutes on a standard desktop computer (Intel(R) Core(TM) i7-7700 @ 3.60GHz, 4 cores, 8 logical cores; 16GB RAM).

Mechanical environment

Although heavily debated for decades, direct deformation and interstitial fluid flow are the mechanical stimuli which are often hypothesised to drive mechanical load-induced adaptation of bone tissue [12]. In order to work with a scalar measure adequately representing the deformation, strain energy densities (SED) is computed. Fluid flow is approximated based on the spatial gradient of the SED, following the assumption that spatial differences in tissue deformation will induce fluid flow [78]. The spatial gradient in the x-direction is calculated as:

$$\frac{\partial f_{i,j,k}}{\partial x} = \frac{f_{i+1,j,k} - f_{i-1,j,k}}{2a} \qquad \text{for voxel } 1 < i < N_x \tag{5.1}$$

where f_i is the SED of a voxel at x-position i, N_x the number of voxels in the x-direction, and a the nominal resolution. The gradients in the y- and z-direction are calculated correspondingly (with $1 < j < N_y$ and $1 < k < N_z$). The norm of the gradient vector (∇SED) is used as quantity for the fluid flow:

$$\nabla\mathrm{SED}_{i,j,k} = \sqrt{\left(\frac{\partial f_{i,j,k}}{\partial x}\right)^2 + \left(\frac{\partial f_{i,j,k}}{\partial y}\right)^2 + \left(\frac{\partial f_{i,j,k}}{\partial z}\right)^2} \tag{5.2}$$

This formulation was used in previous studies to estimate fluid flow [79].

Bone formation and resorption

As mentioned above, image registration allows for a direct comparison of voxels in order to detect areas of bone formation and resorption. Resorption voxels are voxels which are labelled as bone in measurement m_n and background in measurement m_{n+1}. Formation voxels are voxels which are labelled as background in measurement m_n and bone in measurement m_{n+1}. Quiescent voxels are voxels which are labelled as bone in measurement m_n and m_{n+1}.

Analysis of local mechanical environment

To investigate and quantify the relationship between local SED distribution and cellular activity on the bone surface, the bone formation, quiescence, and resorption sites need to be identified [50]. The surface classification method is ported from openVMS/IPL to Python.

The classification in openVMS/IPL is done by adding the images of measurements m_n and m_{n+1}. The voxels in those images contain classification values (m_n: bone = 1, background = 0 and m_{n+1}: bone = 2, background = 0). This results in an image with four possible classification values and adaptation behaviours (0 = background, 1 = resorption, 2 = formation, 3 = quiescence). A 2D example of this superimposed image can be seen in Fig. 5.1(a), where the black-rimmed boxes represent the bone surface at measurement m_n. The result of the subsequent 2D-modified surface classification method is displayed in Fig. 5.1(b). In the original image, the 6-neighbour-topology interfaces between different classification values are classified as formation (2-3 interface, voxel at 3 position is classified), quiescence (0-3 interface, voxel at 3 position is classified) and resorption (0-1 interface, voxel at 1 position is classified) regions (`XIPL_EVAL_BBETW.COM`, `/boundary_between`). The classified bone surface is, therefore, on the bone side of the 6-neighbour-topology, bone-marrow interface at measurement m_n, represented by the black-rimmed boxes in Fig. 5.1. The classified bone surface is only used for the analyses of the SED distribution.

The SED gradient is evaluated on the marrow surface, which is the marrow side of the bone-marrow interface [79]. The marrow surface is classified analogously to the bone surface. The interfaces between different classification values are classified as formation (2-3 interface, voxel at 2 position is classified), quiescence (0-3 interface, voxel at 0 position is classified) and resorption (0-1 interface, voxel at ß position is classified) regions. Only SED and SED gradient values which lay on the bone or marrow surface were used for further calculation.

Conditional probability

The visualisation of the relation between bone (re)modelling behaviour and direct mechanical strain is done with conditional probability plots, also referred to as (re)modelling

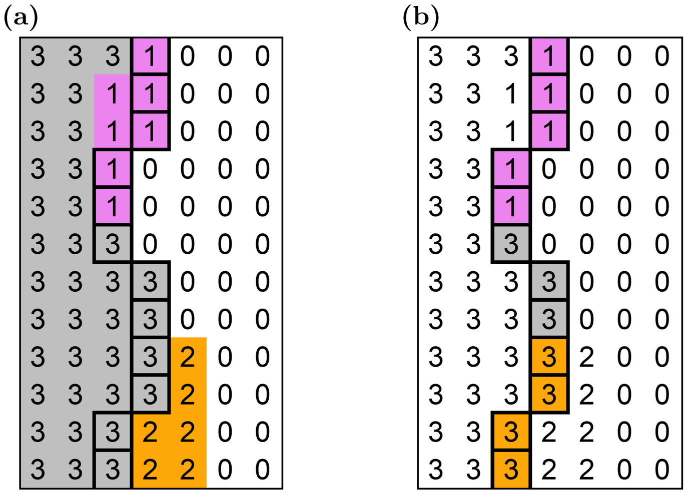

(a)

3	3	3	1	0	0	0
3	3	1	1	0	0	0
3	3	1	1	0	0	0
3	3	1	0	0	0	0
3	3	1	0	0	0	0
3	3	3	0	0	0	0
3	3	3	3	0	0	0
3	3	3	3	0	0	0
3	3	3	3	2	0	0
3	3	3	3	2	0	0
3	3	3	2	2	0	0
3	3	3	2	2	0	0

(b)

3	3	3	1	0	0	0
3	3	1	1	0	0	0
3	3	1	1	0	0	0
3	3	1	0	0	0	0
3	3	1	0	0	0	0
3	3	3	0	0	0	0
3	3	3	3	0	0	0
3	3	3	3	0	0	0
3	3	3	3	2	0	0
3	3	3	3	2	0	0
3	3	3	2	2	0	0
3	3	3	2	2	0	0

Fig. 5.1: 2D example of the surface region classification, with the classification values: 0 = background (white), 1 = resorption (violet), 2 = formation (orange), 3 = quiescence (grey). The black-rimmed boxes represent the bone surface of measurement m_n. **(a)** Superimposed images of measurements m_n and m_{n+1} **(b)** Classified bone surface.

rules [50]. They show the probability for a certain (re)modelling event (formation, resorption or quiescence) to occur, depending on the magnitude of a mechanical quantity (SED and SED gradient).

First, the SED and SED gradient values are normalised within each animal and measurement to remove the variance due to temporal bone adaptation, applied force in FE analysis and individual animals. The normalisation is done with the 99^{th} percentile of all values which are present on the surface and in the volume of interest (VOI) (cortical or trabecular bone, see Section 4.1) and is referred to as SED_{MAX} or ∇SED_{MAX}. This heavily reduces the sensitivity to outliers and, therefore, made the normalisation more stable. At this point, a bone or marrow surface with normalised mechanical quantity values and a bone or marrow surface containing information on (re)modelling behaviour are available. Therewith, a frequency density histogram for each region (formation, quiescence and resorption) can be created. Every histogram consists of 50 bins with equal bin widths, which display the normalised mechanical quantity in the range from 0 to 1. The further underlying assumption is that each (re)modelling event has the same occurrence probability, which rules out possible dependencies on the imbalance due to the size of bone formation and resorption regions. The conditional probability is calculated as relative proportions of the (re)modelling event occurrence probabilities within each bin, which is then plotted over the normalised mechanical quantity. The conditional probabilities are fitted by logarithmic functions using non-linear regression analysis.

Area under the ROC curve (AUC)

The area under the curve (AUC) of a receiver operating characteristic (ROC) curve is used as a performance measurement of a mechanical quantity (SED and SED gradient) classifying and predicting local bone (re)modelling behaviour [80, 81].

For the calculation of the AUC of the formation region, all formation surface voxels are set to “True” and all other surface voxels are set to “False”. If the AUC is lower than 0.5, the classified surface region is changed, i.e. instead of the AUC of the formation region, alternatively the non-formation region can be classified. Voxels which belong to quiescence or resorption regions are set to “True”, while voxels in the formation regions are set to “False” in this case. The ROC curve is a binary classifier—elements of a set are assigned to one of two groups—therefore, the three different surface regions need to be analysed separately. Analogously, analyses are performed for quiescence and resorption regions. The analyses are only performed on voxels on the bone or marrow surface within the VOI (cortical or trabecular bone).

Statistical analysis

Information on the statistical analysis can be found in Section 4.1. The same fixed and random effects are used to compare the AUC between groups and mechanical quantities. Additionally, the mechanical quantity is introduced as an within-subject effect.

5.2 Results

Conditional probability

The functions of the regression lines can be found in Tab. 5.1, with the corresponding coefficients for all groups displayed in Supplementary Tab. S1–S4. In the function of the regression line of the resorption probability in trabecular bone, the offset-parameter y_0 indicates a certain probability for bone resorption to occur in the full range of mechanical stimuli. This suggests a baseline of bone (re)modelling, which is independent of the mechanical stimuli. In this thesis this baseline of formation and resorption probability is referred to as non-targeted bone (re)modelling. Due to the differing function, the parameter y_0 in cortical bone cannot be interpreted in the same way. For both trabecular and cortical bone, the parameter a in the conditional formation and resorption probability fitting functions quantifies the mechanical sensitivity of the system. Additionally, the coefficient b inside the exponent can be interpreted as the amount of mechanical control in the (re)modelling process [50].

In Fig. 5.2 the four possible configurations of bone regions (trabecular and cortical, see Section 4.1) and mechanical quantities (strain energy density, SED or its gradient, ∇SED) are displayed to observe differences within a group (10 Hz dynamic loading) and

Tab. 5.1: Functions to fit non-linear regression lines to conditional probabilities, with $x = SED/SED_{MAX}$ and $x = \nabla SED/\nabla SED_{MAX}$.

	Trabecular bone	Cortical bone
Formation region	$F = a \cdot \left(1 - e^{-b \cdot x}\right) + y_0$	$F = a \cdot \left(1 - e^{-b \cdot x}\right) + y_0$
Quiescence region	$Q = a^{-c} \cdot e^{\frac{x}{-b}} \cdot x^{c-1} + y_0$	$Q = a^{-c} \cdot e^{\frac{x}{-b}} \cdot x^{c-1} + y_0$
Resorption region	$R = a \cdot \left(e^{-b \cdot x}\right) + y_0$	$R = a \cdot \left(e^{-b \cdot x}\right) + c \cdot (x + d) + y_0$

week (m1m2). The comparison of Fig. 5.2(a) and (c) suggests that the (re)modelling rules of trabecular and cortical bone are similar, but not identical. The slope of the conditional formation and resorption probability in Fig. 5.2(c) is steeper, suggesting that cortical bone is slightly more sensitive to mechanical stimuli. The conditional formation probability in trabecular and cortical bone appear to be more sensitive to SED gradient ($a_{trab} = 0.348$, $a_{cort} = 0.426$) rather than SED ($a_{trab} = 0.262$, $a_{cort} = 0.341$), see Fig. 5.2(b) and (d). In contrast, resorption seems to be more sensitive to SED ($a_{SED,\ trab} = 0.259$, $a_{\nabla SED,\ cort} = 0.215$). This contrary behaviour could be generated by the differences in bone and marrow surface, on which the analyses are performed.

All conditional probability plots of cortical bone in the 2 Hz, 5 Hz, static-loading (STAT), and sham-loading (CONT) groups show unexpected behaviour below 2.5-5% SED/SED$_{MAX}$, see Fig. 5.3(a) (not all plots shown). Slight tendencies towards this behaviour are also present in the 10 Hz group, see Fig 5.3(b). For investigation, the results are visualised. In Fig. 5.4(a) only values below 2.5% SED/SED$_{MAX}$ are displayed. This indicates, that due to the loading application in the FE analysis, the processes of the vertebrae do not experience loading. This causes noise in the very low SED/SED$_{MAX}$ regions, which explains the observed behaviour. When fitting the non-linear regressions lines, the values of the three lowest bins are excluded.

Subsequently, the data of all weeks is combined to simplify comparison between groups, see Fig. 5.5 and 5.6. Plots comparing groups for each week are shown in Supplementary Fig. S11–S18. The suggestion that formation in trabecular and cortical bone is more sensitive to the SED gradient is reassured, see Fig. 5.5(a)–(b) and Fig. 5.6(a)–(b). A difference between trabecular and cortical bone can be seen in the quiescence probabilities, see Fig. 5.5(c) and Fig. 5.6(c). The peak of conditional quiescence probability in cortical bone is narrower and at a different SED/SED$_{MAX}$ value compared to trabecular bone. The

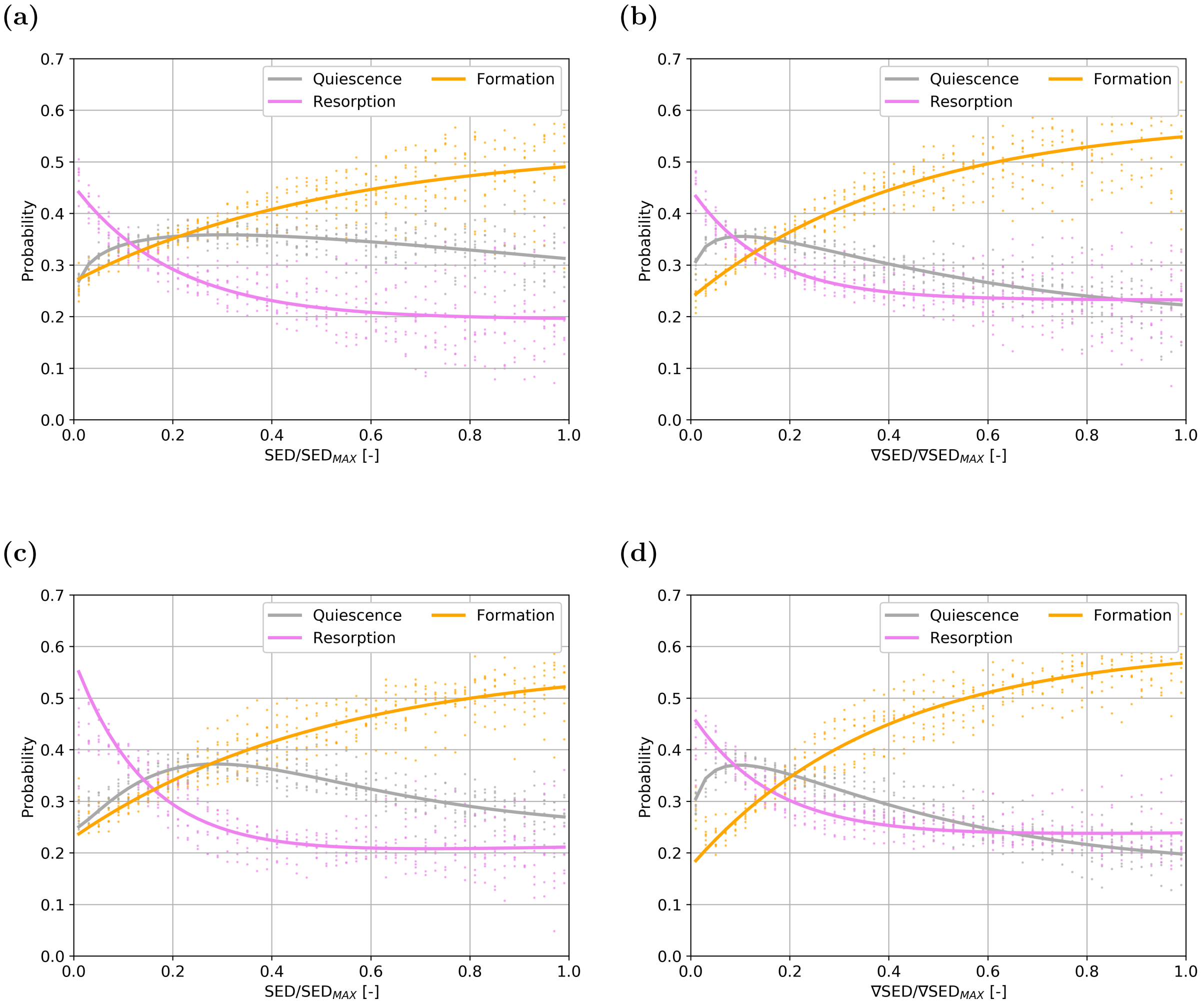

Fig. 5.2: Conditional probability with regression line for trabecular bone in the 10 Hz dynamic-loading group (m1m2, **(a)** SED **(b)** SED gradient). Conditional probability with regression line for cortical bone in the 10 Hz dynamic-loading group (m1m2, **(c)** SED **(d)** SED gradient).

conditional probability of the quiescence in both regions does not seem to be influenced by the type of mechanical loading, see Fig. 5.5(c)–(d) and Fig. 5.6(c)–(d).

There are slight differences between loading groups in the conditional resorption probability of trabecular bone. Dynamic mechanical loading seems to lower the rate of non-targeted bone remodelling, see Fig. 5.5(e) and (f). This is implied by the lower limit of the resorption curve, which is lowered by 5 Hz and 10 Hz dynamic-loading, also see Tab. S1. Thereby, 5 Hz and 10 Hz dynamic-loading results in a higher conditional probability for bone formation, see Fig. 5.5(a) and (b). When increasing the plot range of the normalised mechanical quantity, the conditional quiescence probability decreases with increasing

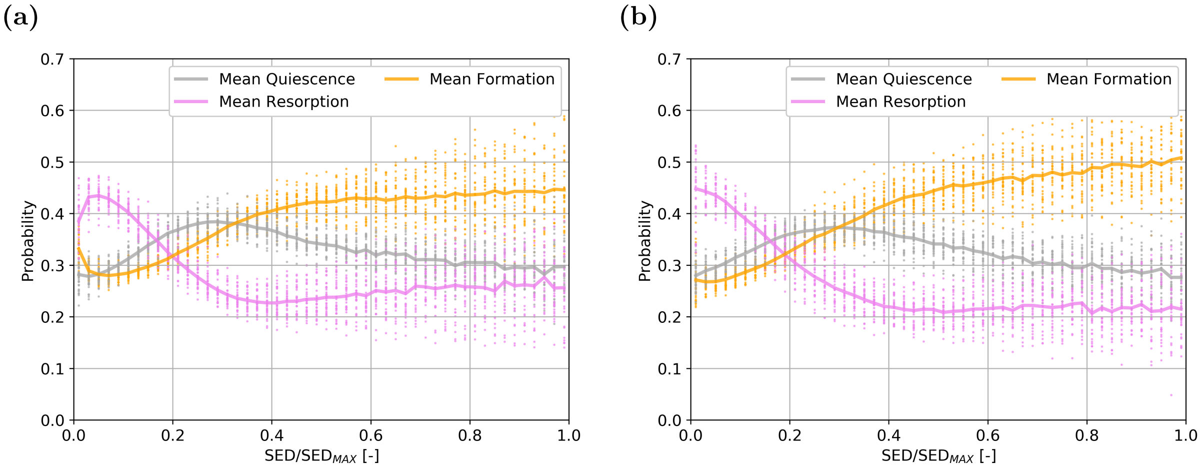

Fig. 5.3: Conditional probability for cortical bone in the **(a)** sham-loading (control) group (all weeks combined) **(b)** 10 Hz dynamic-loading group (all weeks combined)

mechanical quantity and converges towards the conditional resorption probability, see Fig. 5.5(c) and (d) (increased data range not shown).

Cortical bone in general shows similar behaviour, with quiescence not showing differences between groups, see Fig. 5.6(c) and (d). The increase in conditional formation probability correlates with the increase in loading frequency, see Fig. 5.6(a) and 5.6(b), while the rate of non-targeted bone (re)modelling is slightly lowered when applying dynamic loading, see Fig. 5.6(e) and (f). The increase in conditional resorption probability at higher mechanical quantity values is probably due to load application in the FE analysis. Even so this hypothesis of the computational error can be questioned because of the conditional resorption probability of the 10 Hz group, see Supplementary Fig. S6(e) and (f). There is almost no increase in conditional resorption probability in the high SED/SED$_{MAX}$ range.

It is now interesting to establish whether the (re)modelling rules change over time. In trabecular bone, the dynamic-loading groups (2 Hz, 5 Hz, 10 Hz) show an adaptation over time, see Supplementary Fig. S1, S2, and S3. The formation regression lines flatten out, with a decrease in the maximum obtained probability and a corresponding increase in non-targeted bone (re)modelling. This probably happens because the bone adaptation leads to decreased mechanical stimuli, i.e. lower, absolute SED and SED gradient values. In the STAT and CONT groups a similar adaptation over time is not seen, see Supplementary Fig. S4 and S5. Furthermore, there are no adaptations of the conditional probabilities over time in cortical bone, see Supplementary Fig. S6–S10. The suggestion that cortical bone is more sensitive to mechanical stimuli can only be affirmed for the 10 Hz and 5 Hz groups, compare Supplementary Fig. S1(a) with S6(a), and S2(a) with S7(a). The higher sensitivity of cortical bone cannot be observed in the 2 Hz, STAT, or CONT groups.

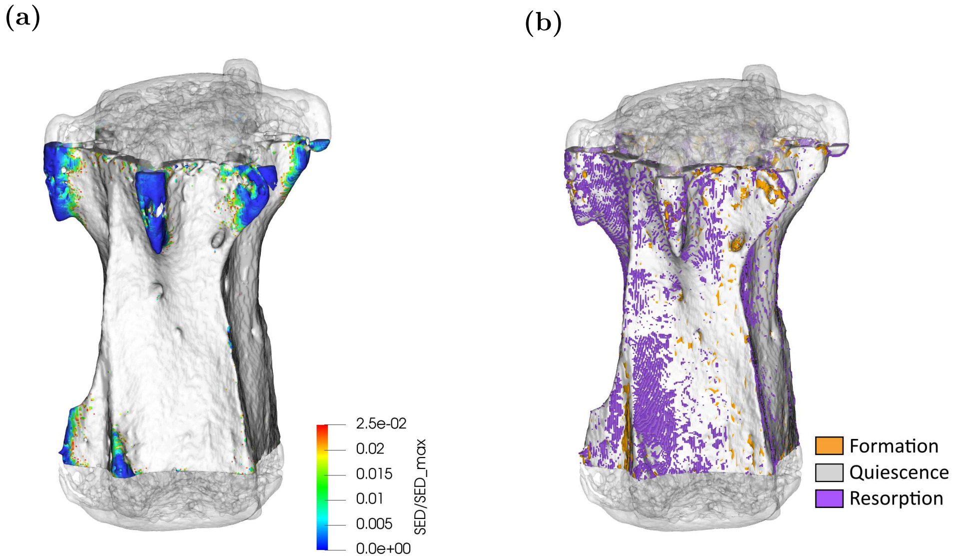

Fig. 5.4: **(a)** Visualisation of the lowest 2.5% SED/SED$_{MAX}$ **(b)** Visualisation of the corresponding vertebra, including formation (orange), quiescence (grey) and resorption (violet) regions.

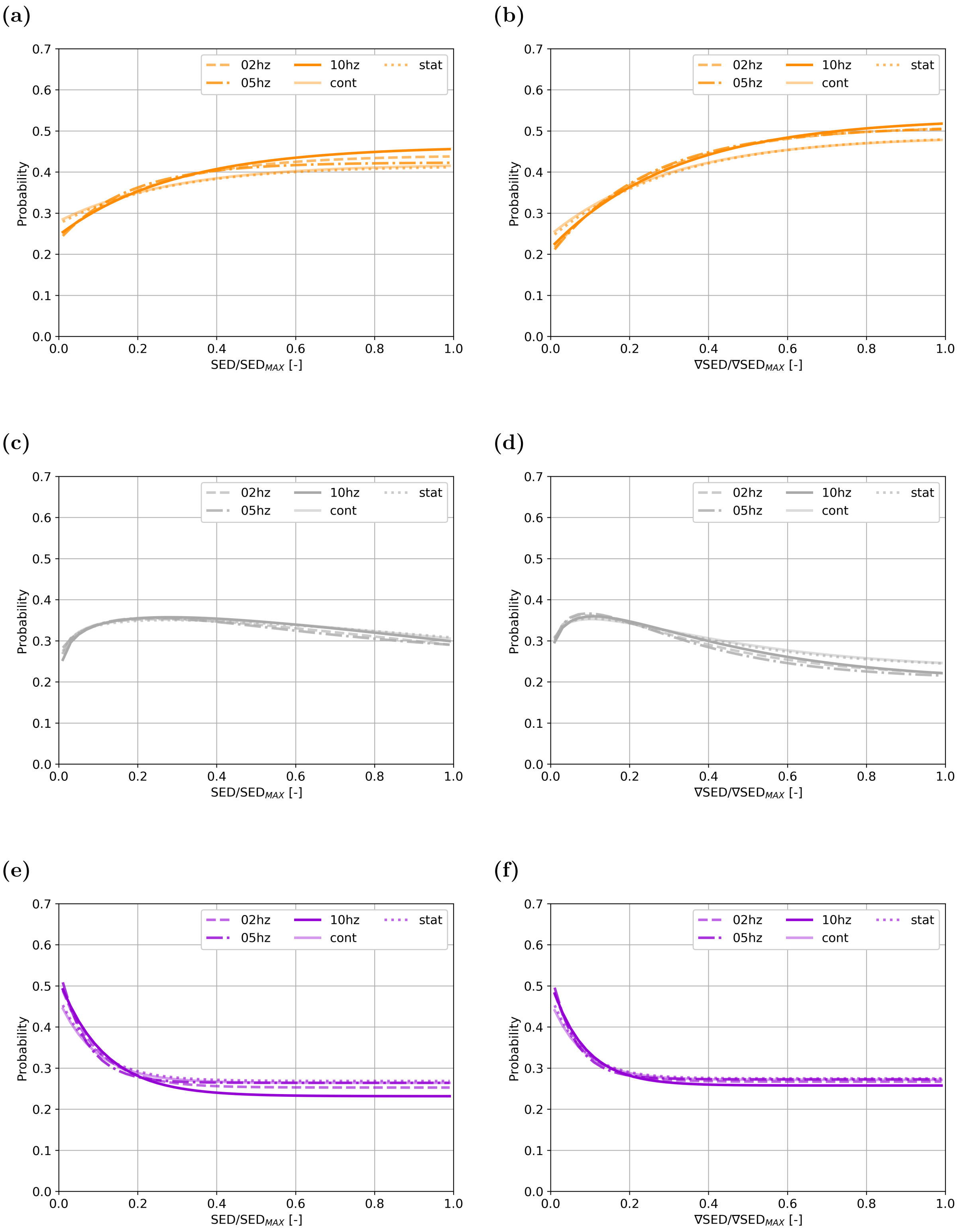

Fig. 5.5: Regression lines for conditional probability for all groups (all time points combined, trabecular bone): **(a)** formation, SED **(b)** formation, SED gradient **(c)** quiescence, SED **(d)** quiescence, SED gradient **(e)** resorption, SED **(f)** resorption, SED gradient.

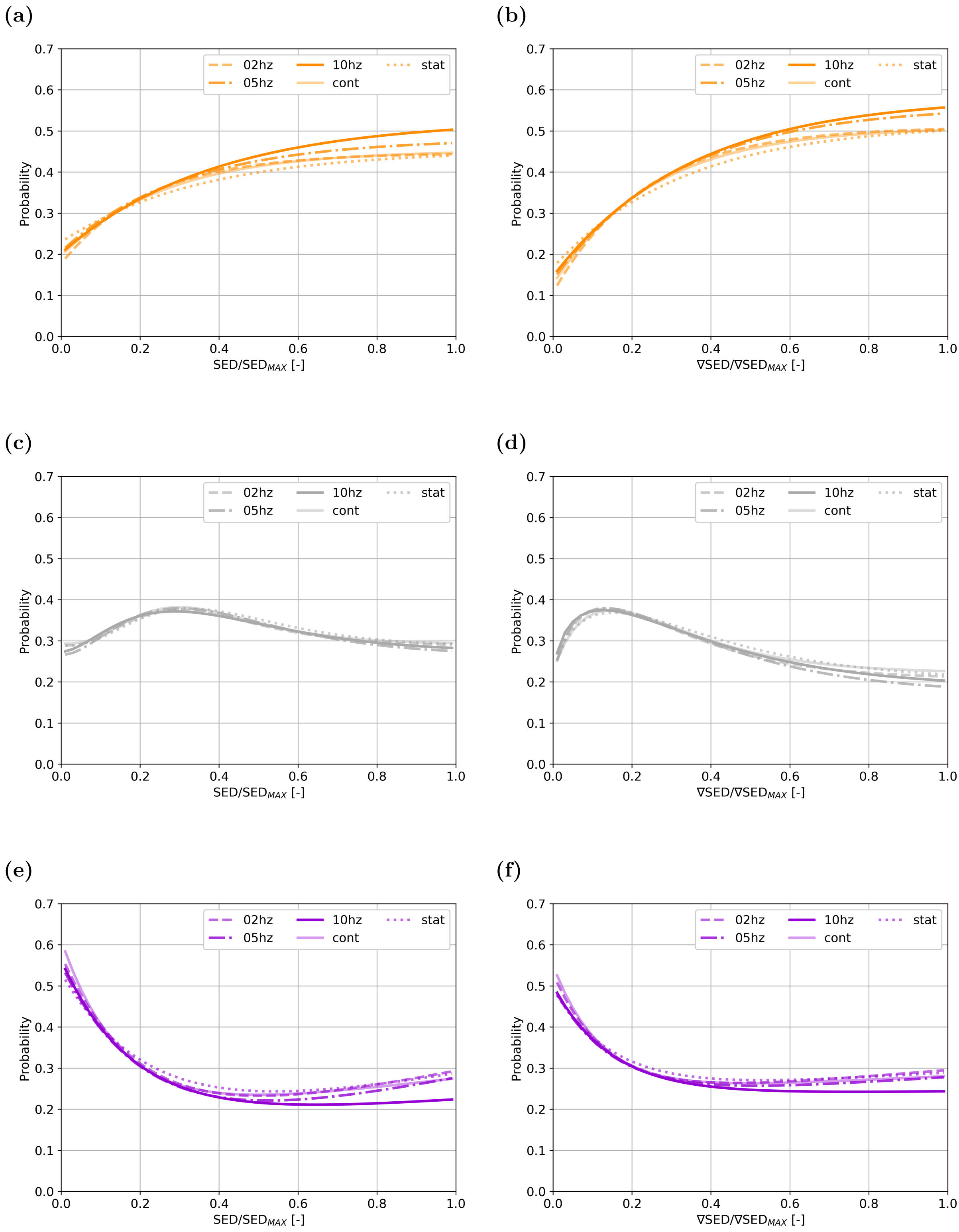

Fig. 5.6: Regression lines for conditional probability for all groups (all time points combined, cortical bone): **(a)** formation, SED **(b)** formation, SED gradient **(c)** quiescence, SED **(d)** quiescence, SED gradient **(e)** resorption, SED **(f)** resorption, SED gradient

Area under the ROC curve (AUC)

A summary of the AUC can be found in Tab. 5.2. Due to the absence of time dependency, values of all measurements are combined. In trabecular bone, no significant difference in AUC (strain energy density, SED) in the formation region between the groups can be seen, see Fig. 5.7(a). The AUC (SED) of the quiescence region is significantly lower in the dynamic-loading groups (2 Hz, 5 Hz, and 10 Hz) ($p < 0.05$, exception: STAT–10 Hz $p = 0.066$). In contrast, no significant difference between dynamic-loading groups or between the static-loading (STAT) and sham-loading (CONT) groups is seen. AUC (SED) of the resorption region in the 10 Hz group is significantly higher than in the STAT and CONT groups ($p < 0.001$), while the 2 Hz and 5 Hz groups are not significantly different to the STAT and CONT groups ($p < 0.1$).

In trabecular bone, the AUC (SED gradient, ∇SED) of the formation and resorption regions in the dynamic-loading groups are significantly higher than in the CONT group ($p < 0.05$), see Fig. 5.7(b). The difference between the dynamic-loading groups and the STAT group is not significant ($p < 0.1$). AUC (∇SED) of the quiescence region is significantly lower in dynamic-loading groups, when compared to the STAT and CONT groups ($p < 0.05$). The AUC (SED) of the formation region is significantly lower than the AUC (∇SED) in all groups ($p < 0.001$), see Fig. 5.7(a) and (b), whereas no significant differences between AUC (SED) and AUC (∇SED) of the quiescence region are observed. The AUC (SED) of the resorption region is significantly lower than the AUC (∇SED) within the CONT, STAT, 2 Hz, and 10 Hz groups ($p < 0.05$). For the 5 Hz group, this difference is not significant ($p = 0.076$).

In cortical bone, the AUC (SED) of the formation region in the 10 Hz group is significantly greater than in all other groups ($p < 0.05$). In the STAT group, it is significantly lower than in the 2 Hz and 5 Hz group ($p < 0.001$). All other differences in the AUC (SED) of the formation region are not significant, see Fig. 5.7(c). The AUC (SED) of the quiescence region is significantly lower in dynamic-loading groups when compared to the STAT and CONT groups ($p < 0.05$), while no significant difference between the dynamic-loading groups and between the STAT and CONT groups is seen. The AUC (SED) of the resorption region in the 10 Hz group is significantly greater than in the STAT and CONT groups ($p < 0.05$). The 5 Hz group only has a significant difference to the STAT group ($p < 0.001$).

Again looking at the cortical bone region, the AUC (∇SED) of the formation region is significantly higher in dynamic-loading groups, compared to the STAT and CONT groups ($p < 0.01$), see Fig. 5.7(d). A similar tendency can be observed in the AUC (∇SED) of the quiescence and resorption regions, with the dynamic-loading groups being significantly lower than the STAT and CONT groups ($p < 0.05$). The AUC (SED) of the formation region is significantly lower than the AUC (∇SED) in all groups ($p < 0.001$), see Fig. 5.7(c)

Region	**Quantitity**	**Loading group**	**AUC Formation**	**AUC Quiescence**	**AUC Resorption**
			Mean ± SD	Mean ± SD	Mean ± SD
Cortical bone	SED	control	0.529 ± 0.013	0.511 ± 0.016	0.599 ± 0.016
		static	0.519 ± 0.016	0.509 ± 0.026	0.585 ± 0.026
		02Hz	0.540 ± 0.014	0.484 ± 0.024	0.607 ± 0.021
		05Hz	0.541 ± 0.011	0.483 ± 0.020	0.618 ± 0.021
		10Hz	0.555 ± 0.020	0.485 ± 0.024	0.624 ± 0.024
	SED gradient	control	0.587 ± 0.016	0.503 ± 0.017	0.612 ± 0.017
		static	0.578 ± 0.020	0.502 ± 0.026	0.599 ± 0.027
		02Hz	0.607 ± 0.019	0.471 ± 0.027	0.621 ± 0.023
		05Hz	0.611 ± 0.016	0.470 ± 0.022	0.633 ± 0.023
		10Hz	0.615 ± 0.022	0.475 ± 0.025	0.638 ± 0.025
Trabecular bone	SED	control	0.542 ± 0.018	0.513 ± 0.017	0.584 ± 0.021
		static	0.544 ± 0.013	0.509 ± 0.015	0.584 ± 0.018
		02Hz	0.552 ± 0.018	0.491 ± 0.018	0.603 ± 0.022
		05Hz	0.548 ± 0.014	0.485 ± 0.020	0.604 ± 0.019
		10Hz	0.555 ± 0.021	0.493 ± 0.024	0.614 ± 0.019
	SED gradient	control	0.593 ± 0.016	0.507 ± 0.018	0.598 ± 0.019
		static	0.597 ± 0.013	0.501 ± 0.016	0.598 ± 0.017
		02Hz	0.613 ± 0.018	0.478 ± 0.021	0.618 ± 0.021
		05Hz	0.614 ± 0.015	0.469 ± 0.024	0.620 ± 0.020
		10Hz	0.611 ± 0.020	0.480 ± 0.027	0.628 ± 0.018

Tab. 5.2: Summary of area under the ROC curve (AUC) values, combined for all measurements.

and (d). However, no significant differences between AUC (SED) and AUC (∇SED) of the quiescence and resorption regions are observed.

In general, the results indicate that the SED gradient has a better performance when predicting local bone formation and resorption. The performance difference between SED and SED gradient to predict quiescence is not significant.

The AUC (SED) is also used to compare the two different registration methods (register whole vertebra and the two halves separately, see Section 3.1). However, there are no differences in AUC (SED) between these methods (data not shown).

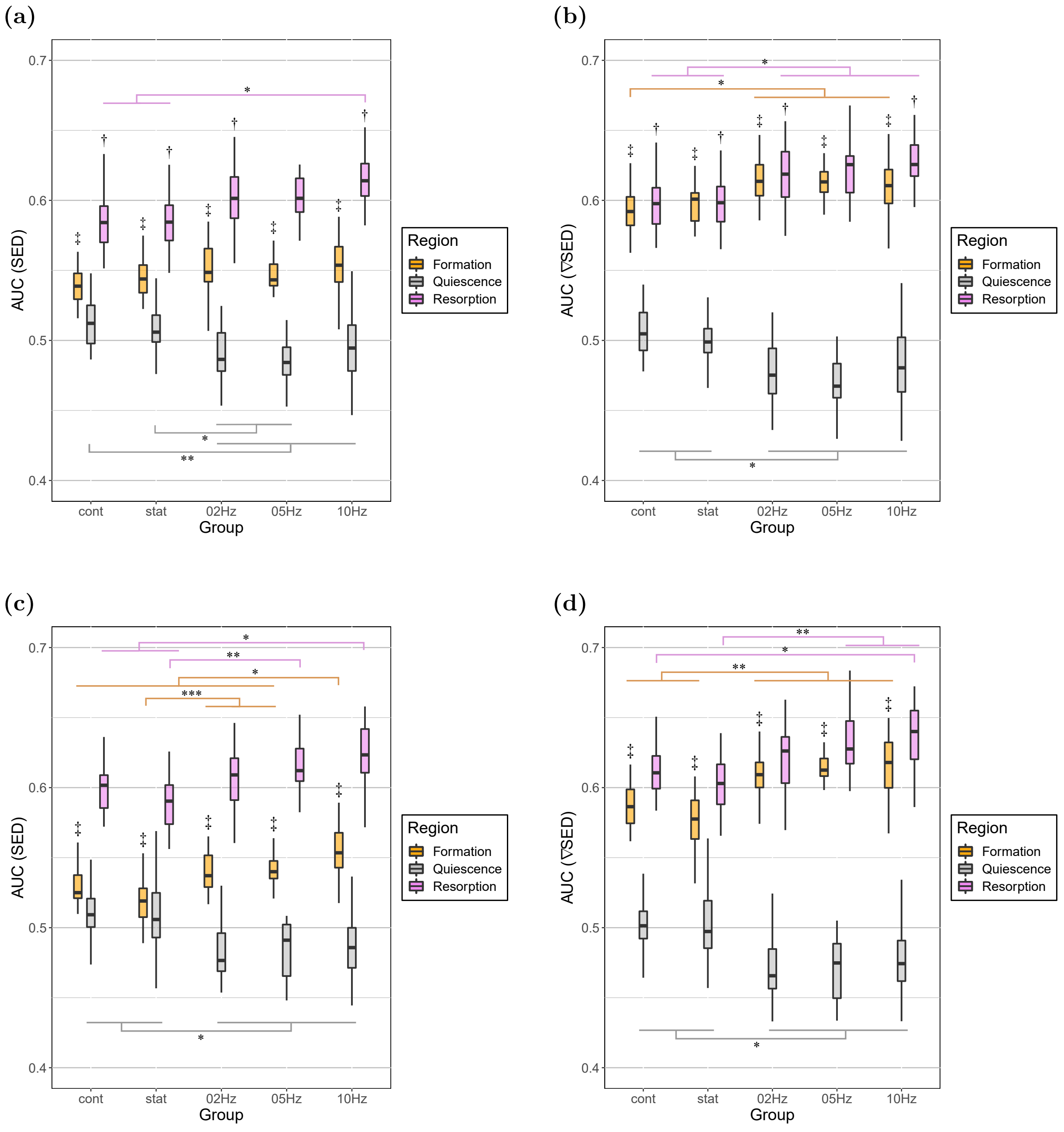

Fig. 5.7: Area under the curve (AUC) for formation (orange), quiescence (grey) and resorption (violet) regions and groups: **(a)** trabecular bone, SED **(b)** trabecular bone, SED gradient **(c)** cortical bone, SED **(d)** cortical bone, SED gradient. (Levels of significance: * relates to $p < 0.05$, ** relates to $p < 0.01$, and *** relates to $p < 0.001$; † indicates significant difference to same measurement of opposite quantity: $^{\dagger} = p < 0.05$, $^{\ddagger} = p < 0.01$)

Chapter 6

Poromicromechanics-based computation of lacunar pore pressure fields

6.1 Hierarchical organization of murine bone

The anatomy of murine and human bone is similar, but not identical. Most importantly, murine bone organs are much smaller than human ones, implying that some features typical for human bone are missing in murine bone, or occur in different size and shape. It is, for example, noteworthy that the blood vessels in murine bone are not embedded in osteonal canals [82].

On the organ scale, murine bone can be divided into cortical and trabecular bone regions, see Fig. 6.1(a), with orange-coloured regions indicating cortical bone and blue-coloured regions indicating trabecular bone. The latter consists of rod- and plate-shaped trabeculae, see Fig. 6.1(b), is surrounded by bone marrow and contains lacunar pores filled with osteocytes, see Fig. 6.1(c), with the violet-stained bone tissue, and dark-blue-stained bone and bone marrow cells. Cortical bone, on the other hand, is more compact and encloses blood vessels and lacunar pores, shown in Fig. 6.1(d), with red-coloured pores indicating blood vessels and yellow-coloured pores indicating lacunar pores and 6.1(e), with the violet-stained bone tissue, and dark-blue-stained bone and bone marrow cells. An example of a lacunar pore is shown in Fig. 6.1(f). The lacunar pores are connected via a canalicular network enabling signalling between osteocytes and to other bone cells [8].

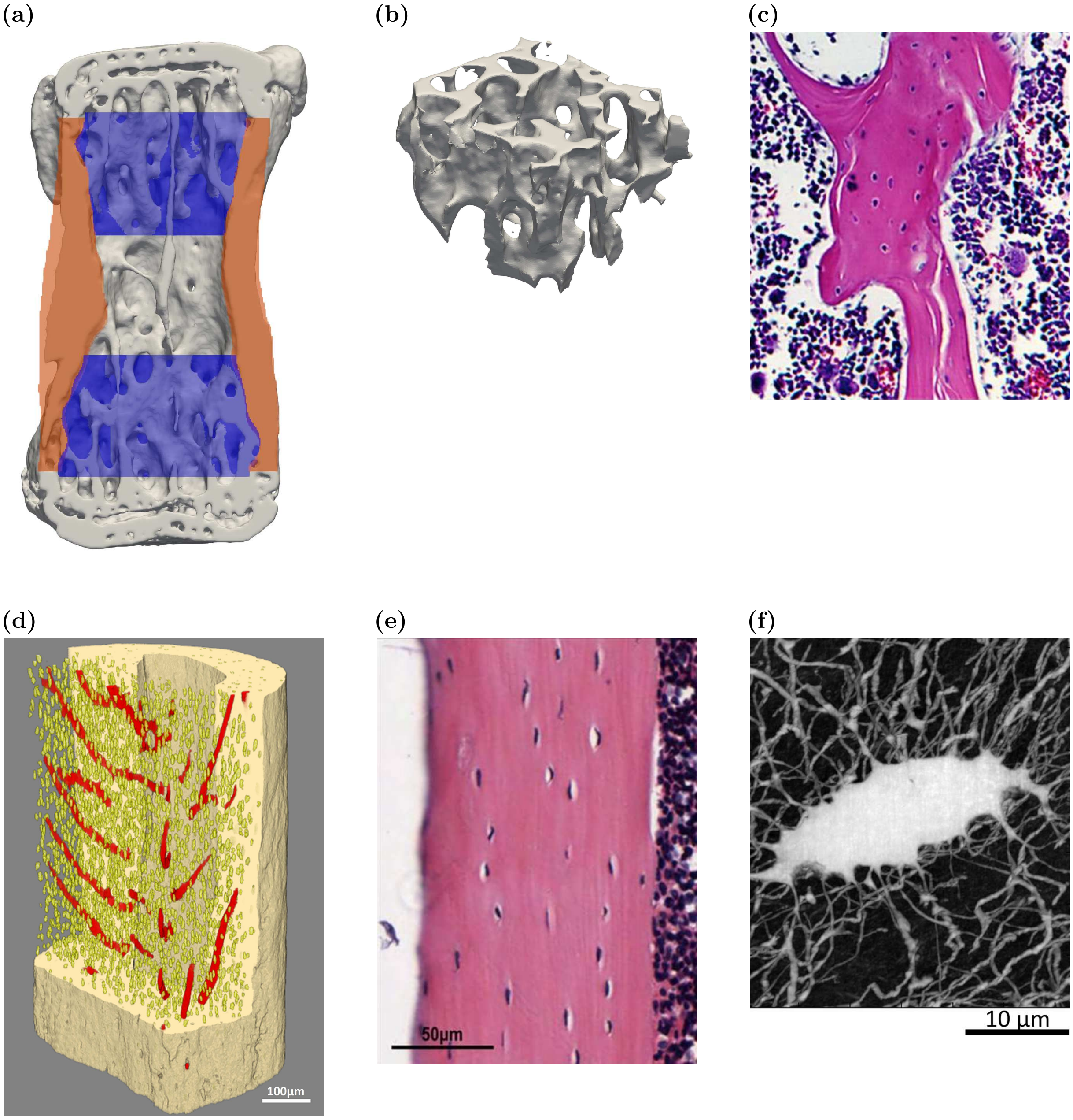

Fig. 6.1: **(a)** 3D rendering of μCT-derived vertebra show cortical (orange) and trabecular (blue) bone regions, see Section 4.1 for details. **(b)** 3D rendering of μCT-derived, trabecular bone from murine vertebra. **(d)** 3D rendering of μCT-derived, cortical bone microporosity including osteocyte lacunae (yellow) and vascular canal network (red) of mouse fibula. Reproduced from [83]. **(c)** Histologic sections, stained with hematoxylin and eosin, of decalcified proximal tibia from 12-week-old mice. Reproduced from [84] **(e)** Representative image of haematoxylin and eosin stained murine cortical bone (femur). Reproduced from [85]. **(f)** Synchrotron phase nano-computed tomography (SR-PNCT) image of the mass density of the mineralised bone matrix showing osteocyte lacuna and canalicular network. Sample: Human jawbone. Reproduced from [86].

6.2 Fundamental concept of continuum (poro-)micromechanics

In continuum micromechanics, microstructural features of a hierarchically organized material are considered for up- and downscaling mechanical properties. In addition, the subfield "poromicromechanics" or "micromechanics of porous media" allows for introducing pore phases at various hierarchical levels, leading to the establishment of relations between the mechanical loading applied macroscopically, and the correspondingly arising pore pressures on the microscale [28, 32].

The investigated material is considered a macro-homogeneous, but micro-heterogeneous body filling a representative volume element (RVE) [87, 88]. Such RVEs with characteristic length l_{RVE} need to fulfil the following separation-of-scales conditions:

- $l_{RVE} \gg d_{RVE}$, d_{RVE} representing the characteristic length of inhomogeneities within the RVE. In particular, l_{RVE} must be (at least) 2-3 times larger than d_{RVE} in order to comply with this requirement [89].
- $l_{RVE} \ll \{L, P\}$, L representing the characteristic length of the geometry and P representing the characteristic length of the loading of a structure built up by the material defined on the RVE. The requirement is fulfilled as long as L and P, respectively, are (at least) 5 to 10 times larger then l_{RVE} [90].

In general, the microstructure of a material is so complicated that it cannot be described in complete detail. Therefore, quasi-homogeneous subdomains with known physical properties are introduced. The so-called material phases typically consist of solid and pore phases. If a single phase has a microstructure itself, its mechanical behaviour can be estimated in sequential fashion by introducing an RVE within this phase, with dimensions $l_{RVE,2} \leq d_{RVE}$ comprising again smaller phases with characteristic length $d_{RVE,2} \ll l_{RVE,2}$ and so on. This leads to the possibility of multistep homogenizations schemes.

6.3 Micromechanical representation of murine bone (for the sake of pore pressure computations)

In the cortical bone matrix, the vascular pores, which contain the blood vessels in murine bone, shown in Fig. 6.1(d), indicated by red colour, have a diameter of 8–10 μm [83, 91–93]. Lacunar pores containing the osteocytes (d_{lac} = 9–10 μm) [83, 92, 94], see Fig. 6.1(d), indicated in yellow, are embedded in the the extravascular bone matrix. In contrast, the trabecular bone matrix only consists of lacunar pores containing the osteocytes and extralacunar bone matrix. Zooming in on the extralacunar bone matrix reveals that the lacunar pores are connected via a canalicular network, see Fig. 6.1(f). The characteristic length of the lacuno-canalicular network in murine bone is $d_{can} = 0.1$–$0.4\,\mathrm{nm}$ [95–97]. The extracanalicular bone matrix consists of collagen fibrils and extrafibrillar space. On even smaller scales intermolecular and intercrystalline spaces are present [28, 98]. The composition and structure of the extracanalicular bone matrix was not relevant for this thesis and is therefore assumed homogeneous and isotropic.

In the cortical regions of murine bone, the vascular pores and lacunar pores have a similar characteristic length. Therefore, murine bone does not fulfil all the required separation-of-scales conditions. In contrast, the trabecular bone matrix does not contain vascular pores and fulfils the required conditions. The characteristic length of the trabeculae L is in the range of 40–75 μm [60, 65]. Subsequently, the image resolution allows differentiation between bone marrow ("vascular pores") and bone matrix. Hence, a model which can be directly applied to voxels containing trabecular bone matrix is adapted from [23]. The established model consists of a single-step homogenization scheme, displayed in Fig. 6.2, and is only applied to bone voxels in the trabecular bone regions, see Section 4.1 and Fig. 4.1(a). The lacunar pores are modelled as spherical inclusions in an isotropic, homogeneous extralacunar bone matrix. All other pore spaces smaller than the lacunar pore space, i.e. the canalicular pore space, but also the intercrystalline and intermolecular pore space, are not considered in the model [23].

6.4 Poromicromechanical up- and downscaling relations

For the theoretical foundation of the subsequently presented mathematical relations, see [23, 28, 32, 99]. The following equations are used to estimate the lacunar pore pressure:

$$p_{lac} = -M^{lac}_{macro}\mathbf{b}^{lac}_{macro} : \mathbf{E} \tag{6.1}$$

with the lacunar pore pressure p_{lac}, the modulus-type quantity M^{lac}_{macro}, the pore-space-specific Biot tensor $\mathbf{b}^{lac}_{macro}$, which quantifies the macroscopic stresses $\mathbf{\Sigma}$ arising in an undeformed trabecular bone RVE, from pressure acting in the lacunar pore space and the macroscopic strains $\mathbf{E}$ imposed as displacements at the boundary of the trabecular RVE. M^{lac}_{macro} is defined as [28]

$$\frac{1}{M^{lac}_{macro}} = \frac{f_{lac,0}}{k_{lac}} + \frac{1}{N^{lac,lac}_{macro}} \tag{6.2}$$

where $f_{lac,0}$ is the initial volume fraction of lacunar pore space (quantified on the macroscopic observation scale), before the RVE of macroscopic trabecular bone is subjected to mechanical loading ($f_{lac,0} + f_{exlac,0} = 1$). Furthermore, k_{lac} denotes the bulk modulus of the fluid contained in the lacunar pores. $N^{lac,lac}_{macro}$ is the so-called Biot modulus, whose

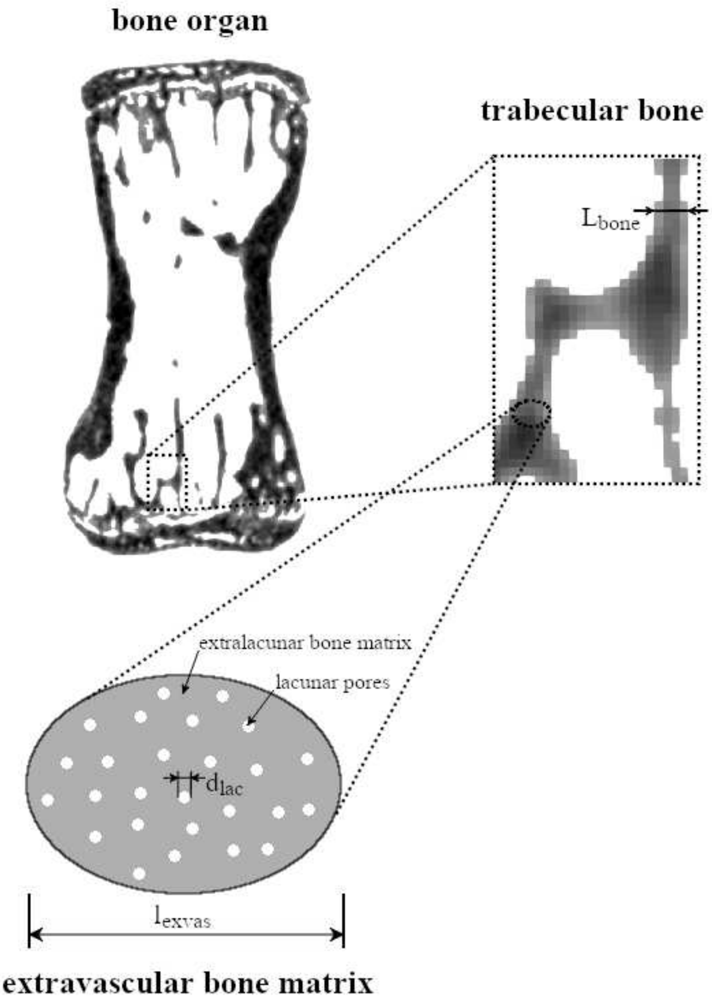

Fig. 6.2: Micromechanical representation of trabecular bone, based on which the poromicromechanical model is developed.

nomenclature is built as follows: Biot modulus $N_r^{j,k}$ considers the effect of the pressure in pore space k on the porosity change of pore space j, whereby both pore spaces are measured in RVE r. The Biot modulus is defined as

$$\frac{1}{N_{macro}^{lac,lac}} = -\mathbf{b}_{exlac}^{lac} : \left(\mathbb{C}_{exlac}\right)^{-1} : \left(f_{lac,0}\mathbf{b}^{lac} - \mathbf{b}_{macro}^{lac}\right) \tag{6.3}$$

with the Biot tensors

$$\mathbf{b}_{exlac}^{lac} = \mathbf{b}_{lac} = \mathbf{1} \qquad \mathbf{b}_{macro}^{lac} = \bar{f}_{lac}\mathbf{1} : \mathbb{A}_{lac} \tag{6.4}$$

whereby $\bar{f}_{lac}$ is the volume fraction of the lacunar pore space, quantified within the RVE of extravascular bone matrix, and $\mathbb{A}_{lac}$ the so-called concentration or “downscaling” tensor [98], relating extravascular strains to those in the extralacunar and (drained) lacunar spaces:

$$\mathbb{A}_{lac} = \mathbb{A}^{\infty}_{lac} : \left(f_{exlac,0} \mathbb{A}^{\infty}_{exlac} + f_{lac,0} \mathbb{A}^{\infty}_{lac} \right)^{-1} \tag{6.5}$$

$$\mathbb{A}^{\infty}_{lac} = \left(\mathbb{I} + \mathbb{P}^{0}_{lac} : \left(\mathbb{C}_{lac,drained} - \mathbb{C}_{exlac} \right) \right)^{-1} \tag{6.6}$$

$$\mathbb{A}^{\infty}_{exlac} = \mathbb{I} \tag{6.7}$$

$$\mathbb{C}_{lac,drained} = 0 \tag{6.8}$$

with the initial volume fraction of extralacunar matrix $f_{exlac,0}$, the stiffness tensor of the extralacunar matrix $\mathbb{C}_{exlac}$, the drained lacunar pore space (air) $\mathbb{C}_{lac,drained}$ and the Hill tensor $\mathbb{P}^{0}_{lac}$ for spherical inclusions in an isotropic auxiliary matrix [98].

Model input parameters

The mechanical properties of bone tissue vary strongly between species and are scale-dependent. The extralacunar stiffness is assumed to be isotropic and is estimated using the Young's modulus values described in Section 3.1 and a Poisson's ratio of $\nu = 0.3$.

To calculate the pore pressure, see Eq. (6.1), macroscopic strains are needed as input. These strains result from the FE analysis (see Section 5.1), using grey-scale images (see Section 3).

The volume fraction of lacunar pore space in trabecular bone is assumed to be $f_{lac,0} = 1.5\%$ [83, 100]. There are no clear differences between osteocyte lacunar sizes and numbers in trabecular and cortical bone [101]. The vascular porosity in murine cortical bone is 0.5–2% [83, 102]. The difference between the volume fraction of lacunar pore space quantified within the trabecular bone RVE and within the RVE of extravascular bone matrix is negligibly small, hence $f_{lac,0} = \bar{f}_{lac}$. The bulk modulus of the fluid contained in the lacunar pores is approximated by that of water $k_{lac} = 2.3\,\text{GPa}$ [23].

6.5 Results

Lacunar pore pressure

Because the Biot tensor $\mathbf{b}^{lac}_{macro}$ only has entries along the main diagonal, the pore pressure is calculated as

$$p = \mathrm{b}_{xx}\mathrm{E}_{xx} + \mathrm{b}_{yy}\mathrm{E}_{yy} + \mathrm{b}_{zz}\mathrm{E}_{zz} \tag{6.9}$$

The entries along the main diagonal of the Biot tensor are identical $\mathrm{b}_{xx} = \mathrm{b}_{yy} = \mathrm{b}_{zz}$. Considering $\mathrm{E}_{sum} = \mathrm{E}_{xx} + \mathrm{E}_{yy} + \mathrm{E}_{zz}$, the pore pressure from Eq. (6.9) is simplified as

$$p = \mathrm{b}_{xx}\mathrm{E}_{sum} \tag{6.10}$$

A histogram of E_{sum} is shown in Fig. 6.3(b). All voxels containing positive E_{sum} values are ignored, as the model does not account for “negative” pore pressure and possible effects like cavitation. Fig. 6.3(a) displays a histogram of the estimated lacunar pore pressure. Pore pressures of up to 3–4 MPa are found in very high strain regions.

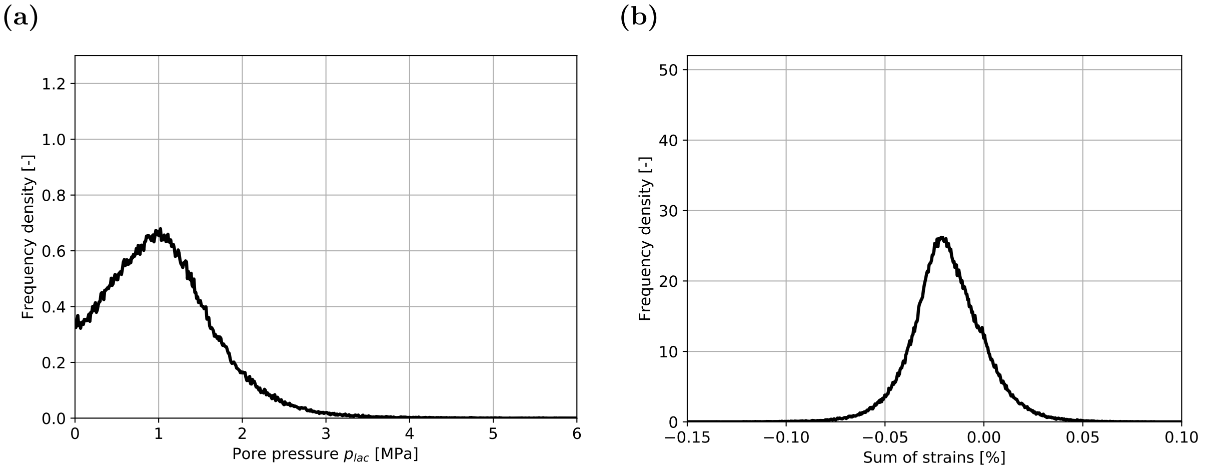

Fig. 6.3: **(a)** Density histogram of the pore pressure p_{lac} in the bone voxels of the trabecular bone region **(b)** Density histogram of the strains summed along the main diagonal ($\mathrm{E}_{sum} = \mathrm{E}_{xx} + \mathrm{E}_{yy} + \mathrm{E}_{zz}$) in the bone voxels of the trabecular bone region. Sample: Week m1, Mouse 02, 10 Hz dynamic-loading group.

Fig. 6.4 provides a summary of the pore pressure of all groups in each week. Additionally, Fig. 6.5 displays the pore pressure of each group over time. The discrepancy in pore pressure distribution between sham loading (control) and all other groups can be explained by the different loading in the FE analysis, i.e. 4 N for sham-loading and 8 N for all other groups (see Section 5.1). Notably, the amount of mechanical force applied to the bone can directly be linked to the pore pressure.

In addition, the peak of the pore pressure distribution in the dynamic loading groups moves closer to zero over time, see Fig. 6.5(c), (d) and (e). This can be explained by the trabecular bone adaptation in the dynamic-loading groups, which decreases the resulting strains (see Section 4.2). In contrast, the pore pressure distribution in the sham-loading (control) and static-loading groups does not change over time, see Fig. 6.5(a) and (b), because there is little to no bone adaptation occurring (see Section 4.2).

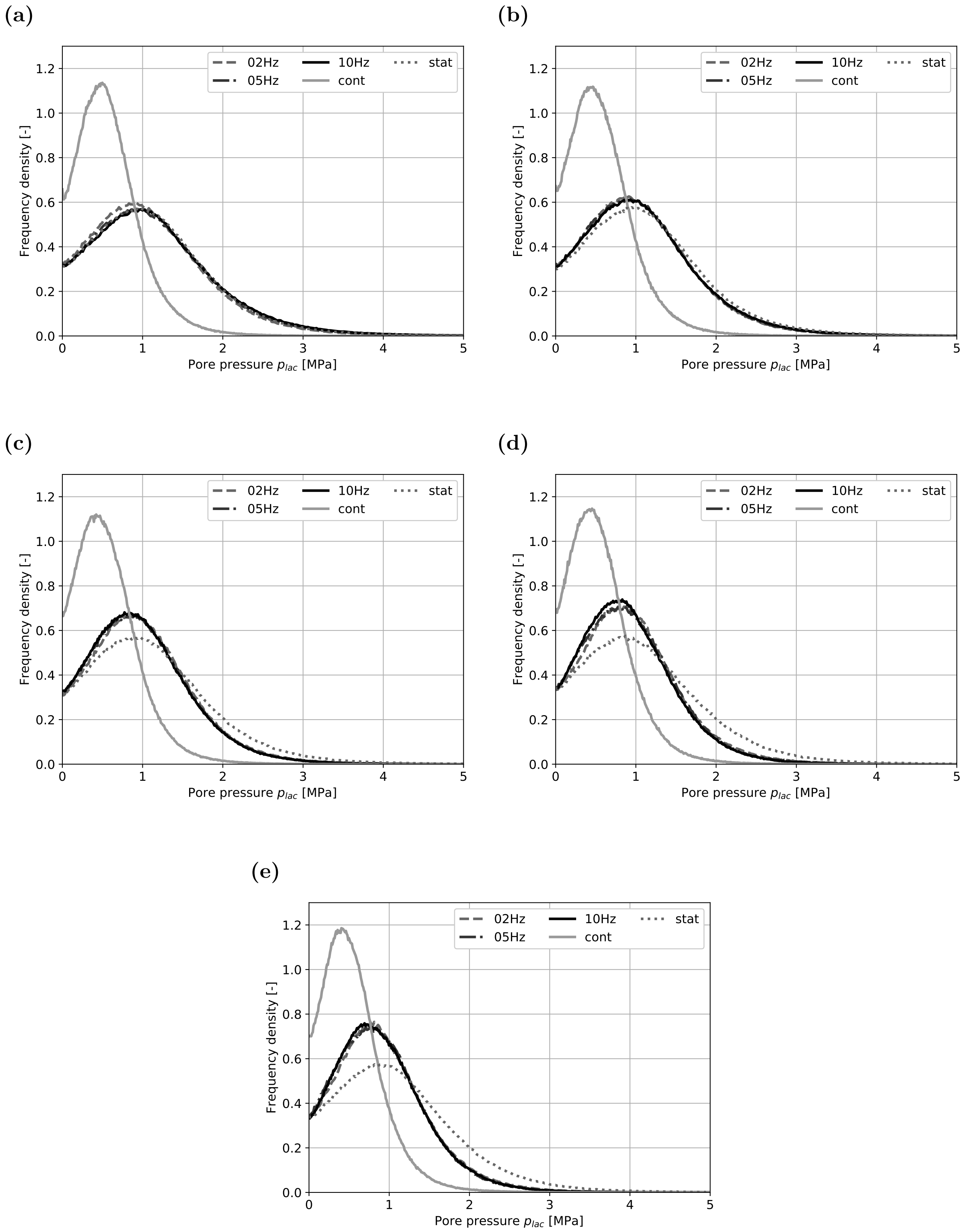

Fig. 6.4: Density histogram of the pore pressure in the bone voxels of the trabecular bone regions for all groups in week **(a)** m1 **(b)** m2 **(c)** m3 **(d)** m4 **(e)** m5.

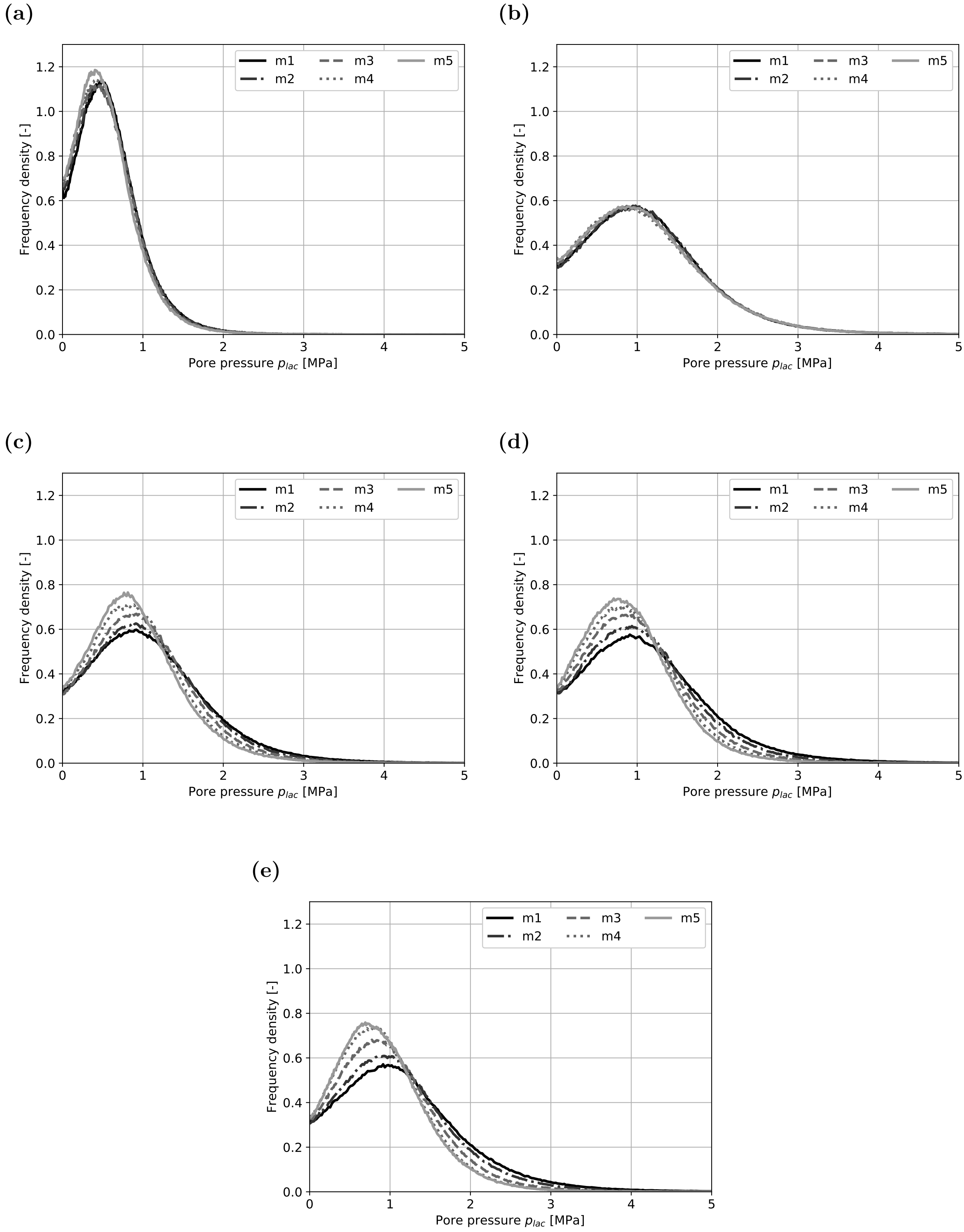

Fig. 6.5: Density histogram of the pore fluid velocity in the bone surface voxels of the trabecular bone regions over time in the **(a)** sham-loading (control) group **(b)** static-loading group **(c)** 2 Hz dynamic-loading group **(d)** 5 Hz dynamic-loading group **(e)** 10 Hz dynamic-loading group.

Chapter 7

Micromechanics-inspired computation of canalicular fluid flow

Information on the hierarchical organization of murine bone, pore spaces and the fundamental concept of continuum (poro-)micromechanics can be found in Sections 6.1 and 6.2.

7.1 Micromechanical representation of murine bone (for the sake of fluid flow computations)

Analogous to the model introduced in Section 6.3, a two-step homogenization scheme is used. This scheme is based on the previously used model, with an additional homogenization step being introduced, see Fig. 7.1. The extralacunar bone matrix is modelled as an homogeneous, isotropic, extracanalicular bone matrix with arbitrarily oriented, cylindrical inclusions [29]. Both intercrystalline and intermolecular pore spaces are neglected in this work.

As mentioned in Section 6.3, murine cortical bone does not fulfil all the required separation-of-scales conditions. Therefore, the model is only applied to bone voxels in the trabecular bone regions, see Section 4.1 and Fig. 4.1(a).

7.2 Relations between macroscopic pressure gradients and pore-scale fluid flow

The theoretical foundations of pressure gradient downscaling and the derivation of scaling relations can be found in [29].

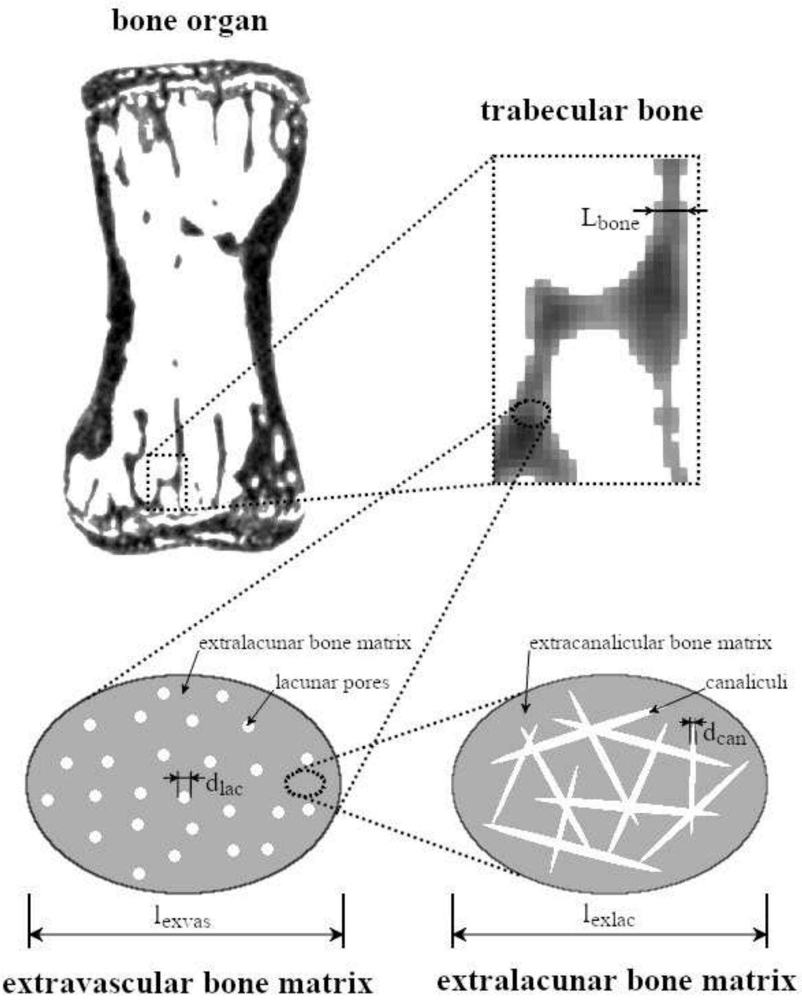

Fig. 7.1: Micromechanical representation of trabecular bone, based on which the poromicromechanical model is developed.

The results from the FE analysis (see Section 5.1), using grey-scale images (see Section 3), represent the macroscopic stresses acting on the macroscopic bone matrix and are used as input stresses. Hence, the macroscopic pressure gradient is assumed to be

$$(\mathbf{grad}\, p_{macro})_{i,j,k} = \left[\mathrm{tr}\left(\frac{\partial \mathbf{\Sigma}_{i,j,k}}{\partial x}\right), \mathrm{tr}\left(\frac{\partial \mathbf{\Sigma}_{i,j,k}}{\partial y}\right), \mathrm{tr}\left(\frac{\partial \mathbf{\Sigma}_{i,j,k}}{\partial z}\right) \right]^T \tag{7.1}$$

where the traces of stress gradients are the entries of the macroscopic pressure gradient vector. The stress gradient in the x-direction is calculated as

$$\frac{\partial \mathbf{\Sigma}_{i,j,k}}{\partial x} = \frac{\mathbf{\Sigma}_{i+1,j,k} - \mathbf{\Sigma}_{i-1,j,k}}{2a} \qquad \text{for voxel } 1 < i < N_x \tag{7.2}$$

where $\mathbf{\Sigma}_i$ is the macroscopic stress tensor of a voxel at x-position i, N_x the number of voxels in the x-direction and a the nominal resolution. The gradients in the y- and z-direction are calculated correspondingly (with $1 < j < N_y$ and $1 < k < N_z$). The stress tensors of the bone marrow voxels are negligibly small and therefore assumed $\mathbf{\Sigma} = 0$.

Furthermore, this macroscopic pressure gradient needs to be downscaled by means of the downscaling relations, introduced in [29], from the RVE of macroscopic bone matrix, which are

$$\mathbf{grad}\, p_{lac} = \mathbf{A}_{lac} \cdot \mathbf{grad}\, p_{macro} \tag{7.3}$$

and

$$\mathbf{grad}\, p_{exlac} = \mathbf{A}_{exlac} \cdot \mathbf{grad}\, p_{macro} \tag{7.4}$$

where $\mathbf{grad}\, p_{lac}$ and $\mathbf{grad}\, p_{exlac}$ are the pressure gradients in the lacunar pores and in the extralacunar bone matrix, $\mathbf{A}_{lac}$ and $\mathbf{A}_{exlac}$ are the concentration tensors of the lacunar pores and of the extralacunar bone matrix and $\mathbf{grad}\, p_{macro}$ is the pressure gradient on the RVE of the macroscopic trabecular bone matrix.

One scale below, the orientation-dependent pressure gradients in the canalicular pores $\mathbf{grad}\, p_{can}(\vartheta, \varphi)$ and the pressure gradient in the extracanalicular bone matrix $\mathbf{grad}\, p_{excan}$ are derived to be

$$\mathbf{grad}\, p_{can}(\vartheta, \varphi) = \mathbf{A}_{can}(\vartheta, \varphi) \cdot \mathbf{grad}\, p_{exlac} \tag{7.5}$$

and

$$\mathbf{grad}\, p_{excan} = \mathbf{A}_{excan} \cdot \mathbf{grad}\, p_{exlac} \tag{7.6}$$

where $\mathbf{A}_{can}(\vartheta, \varphi)$ is the orientation-dependent concentration tensor of the canalicular pores and $\mathbf{A}_{excan}$ is the concentration tensor of the extracanalicular bone matrix.

Because the canalicular pores are not oriented along one axis but arbitrarily, a pressure gradient for arbitrarily oriented canalicular pores is calculated:

$$\mathbf{grad}\, p_{can,arb} = \mathbf{A}_{can,arb} \cdot \mathbf{grad}\, p_{exlac} \tag{7.7}$$

where $\mathbf{A}_{can,arb}$ is the concentration tensor of arbitrarily oriented canalicular pores. $\mathbf{A}_{can,arb}$ is estimated by averaging $\mathbf{A}_{can}(\vartheta, \varphi)$ over 28 different needle orientations (Stroud's integration) [103].

Thus, to estimate the pore fluid velocities downscaled, the canalicular pressure gradients are inserted into

$$v_{can} = \frac{r_{can}^2}{8\eta} |\mathbf{grad}\, p_{can,arb}| \tag{7.8}$$

where r_{can} is the radius of the canaliculus, η is the dynamic fluid viscosity and $|\mathbf{grad}\, p_{can,arb}|$ is the norm of the pressure gradient in the arbitrarily oriented canalicular pores.

Model input parameters

The concentration tensors $\mathbf{A}_{lac}$, $\mathbf{A}_{exlac}$, $\mathbf{A}_{can}(\vartheta,\varphi)$, and $\mathbf{A}_{excan}$ are estimated according to the supplementary material in [29]. The following parameters are used in this calculation:

- $r_{can} = 0.1\,\mu\text{m}$ is the radius of the canaliculus [95–97].
- $r_{lac} = 4.5\,\mu\text{m}$ is the radius of the (spherical) lacunar pores [83, 92, 94].
- $\phi_{lac}^{exvas} = 1.5\%$ is the volume fraction of the lacunar pores quantified on the RVE of extravascular bone matrix [83, 100]. Due to the small vascular porosity (0.5–2% [83, 102]), the difference between the volume fraction of lacunar pore space quantified within the trabecular bone RVE and within the RVE of extravascular bone matrix is negligibly small, hence $\phi_{lac}^{exvas} = \phi_{lac}^{macro}$.
- $\phi_{can}^{exlac} = 1\%$ is the volume fraction of the canalicular pores quantified on the RVE of extralacunar bone matrix [100]. Due to the small vascular and lacunar porosity, the difference between the volume fraction of canalicular pore space quantified within the trabecular bone RVE and within the RVE of extralacunar bone matrix is negligibly small, hence $\phi_{can}^{exlac} = \phi_{can}^{macro}$.

Notably, r_{can} is difficult to define because of the rough, uneven canalicular walls [104] and the fact that canaliculi get thicker towards osteocyte lacunae [95, 104]. This may explain the variability in reported canaliculus diameter [100, 105]. Hence, the above-defined number for this radius should be considered as a rough approximation. Furthermore, considerations concerning the dynamic fluid viscosity $\eta = 0.007\,\text{Pa s}$ can be found in [29].

7.3 Results

Pressure gradient downscaling

First, the downscaling relations are studied on a general basis by considering a macroscopic pressure gradient from the upper range of the bone surface values of $\mathbf{grad}\,p_{macro} = [0, 0, 500]^T\,\text{kPa/mm}$. Fig. 7.2 displays the result in each material phase. The pressure gradient in the lacunar pores is zero, whereas in the extralacunar bone matrix it is slightly increased to 507.6 kPa/mm. This pressure gradient is then further amplified in the canalicular pores to 563.4 kPa/mm and almost remains the same in the extracanalicular bone matrix at 507.1 kPa/mm.

Pore fluid velocity

Fig. 7.3(a) shows the distribution of the pore fluid velocity of all bone voxels, whereas Fig. 7.3(b) displays the distribution of all bone surface voxels. The pressure gradient at the bone surface is greater because the neighbouring bone marrow voxels do not experience

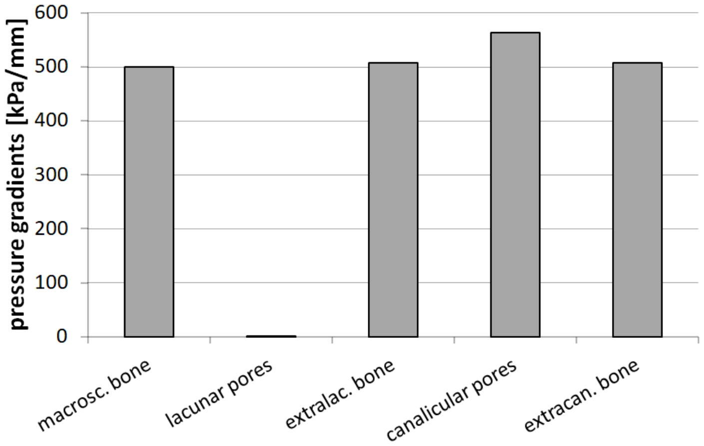

Fig. 7.2: Pressure gradient $\mathbf{grad}\, p_{macro} = [0, 0, 500]^T$ kPa/mm applied on the level of macroscopic bone tissue, and the corresponding pressure gradients in all material phases considered; thereby considering all possible canalicular pore orientations.

stress ($\boldsymbol{\Sigma} = 0$) and the pore fluid velocity is therefore greater. It is more interesting to investigate the fluid velocity at the bone surface, as this is where bone (re)modelling can be tracked with micro-CT scans.

Assuming that higher fluid velocity values induce bone adaptation, the important value range is about 70–120 μm/s, see Fig. 7.3(b); this is in the range of what was previously reported by Estermann et al. [29].

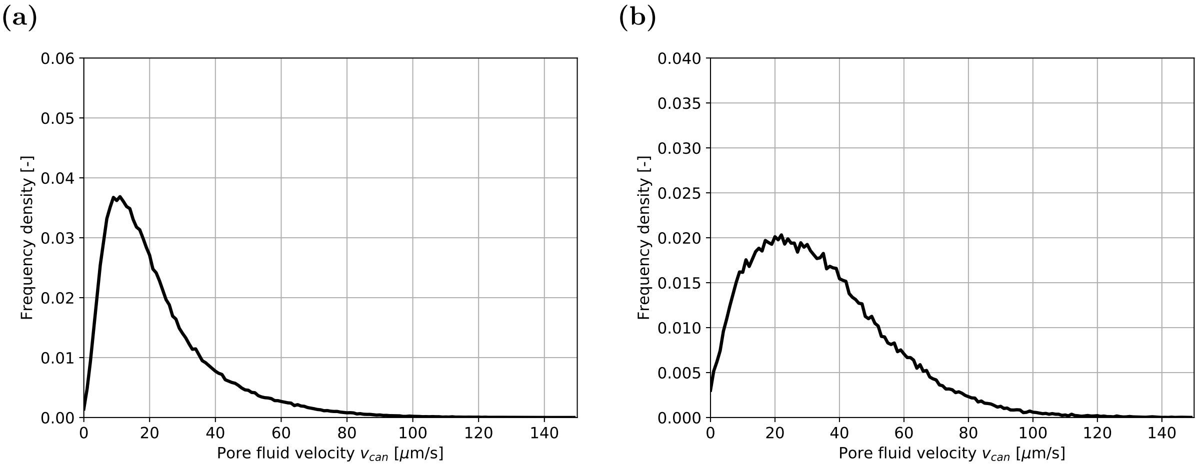

Fig. 7.3: **(a)** Density histogram of the canalicular fluid velocity v_{can} in the bone voxels of the trabecular bone region. **(b)** Density histogram of the canalicular fluid velocity v_{can} in the bone surface voxels of the trabecular bone region. Sample: Week m1, Mouse 02, 10 Hz dynamic-loading group.

Fig. 7.4 provides a summary of the pore fluid velocity of all groups in each week. In addition, Fig. 7.5 displays the pore fluid velocity of each group over time. The discrepancy in fluid velocity distribution between sham-loading (control) and all other groups can be explained by the different loading in the FE analysis, i.e. 4 N for sham-loading and 8 N for all other groups (see Section 5.1). Consequently, the amount of mechanical force applied to the bone can directly be linked to the occurring fluid velocity and becomes important when looking at the fluid velocities necessary to stimulate bone cells.

In addition, the peak of the fluid velocity distribution in the dynamic-loading groups moves closer to zero over time, see Fig. 7.5(c), (d) and (e). This can be explained by the trabecular bone adaptation in the dynamic-loading groups, which decreases the o strains (see Section 4.2). However, the fluid velocity distribution in the sham-loading (control) and static-loading groups, in contrast, does not change over time, see Fig. 7.5(a) and (b), because there is no to little bone adaptation happening (see Section 4.2).

Spatial distribution of lacunar pore pressure and canalicular pore fluid velocity

Fig. 7.6 shows a scatter plot of lacunar pore pressure and canalicular pore fluid velocity for one bone sample. While the plot in Fig. 7.6(a) considers all bone voxels, Fig. 7.6(b) only considers the bone surface voxels. Because of the small pressure gradient within the bone, a big cluster of non-correlating values occurs, see Fig. 7.6(a). Furthermore, Fig. 7.6(b) displays a correlation between the pore pressure and the pore fluid velocity in the bone surface voxels. This correlation also resulted from the same FE analysis results being used as input parameters.

In Section 6.5, it is stated that “negative” pore pressure is not considered in the results. From the scatter plot of the bone surface voxels, see Fig. 7.6(b), it can be observed that in cases of $p_{lac} < 0$ (macroscopic, tensile stress) the fluid velocity still provides information.

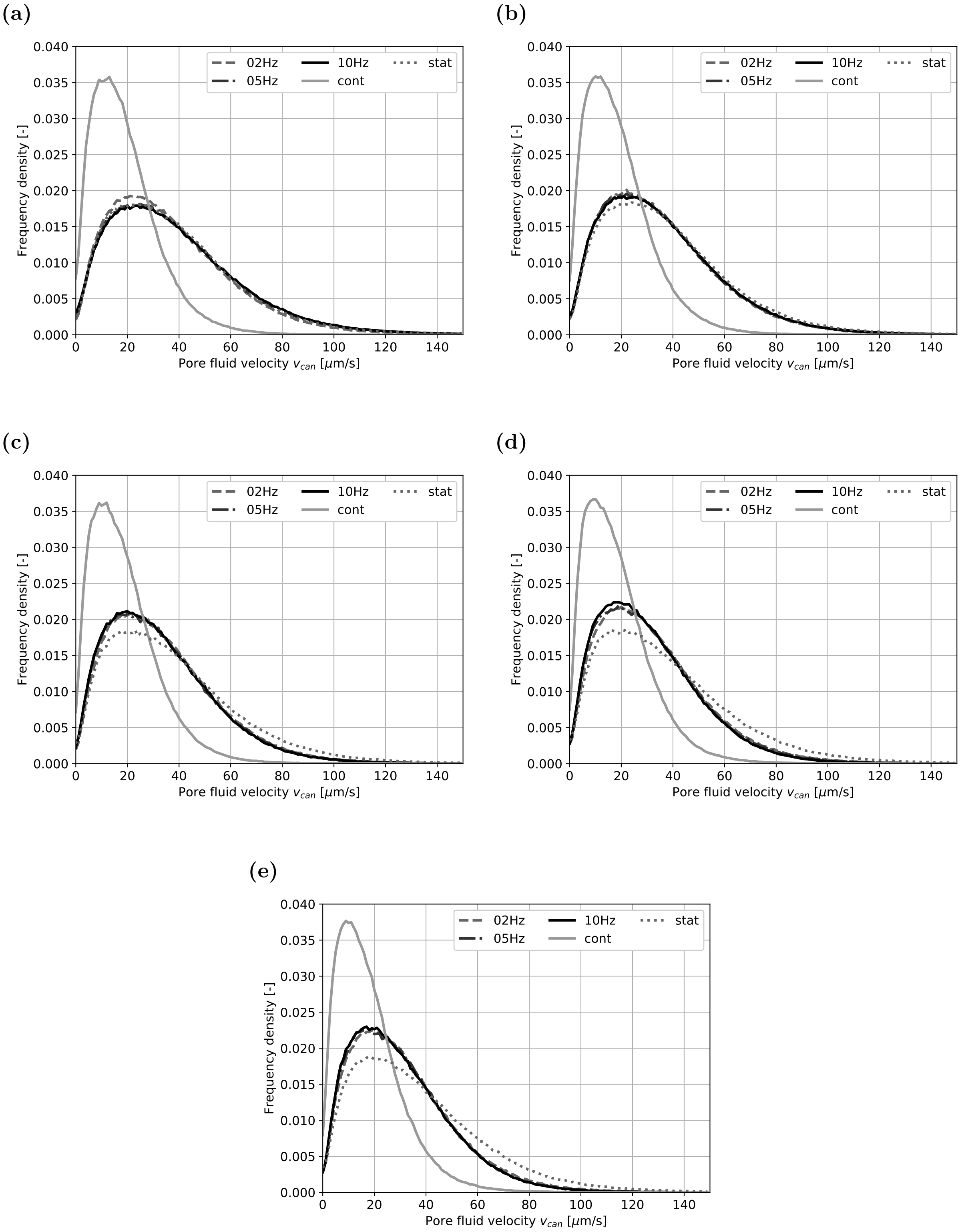

Fig. 7.4: Density histogram of the pore fluid velocity in the bone surface voxels of the trabecular bone regions for all groups in week **(a)** m1 **(b)** m2 **(c)** m3 **(d)** m4 **(e)** m5.

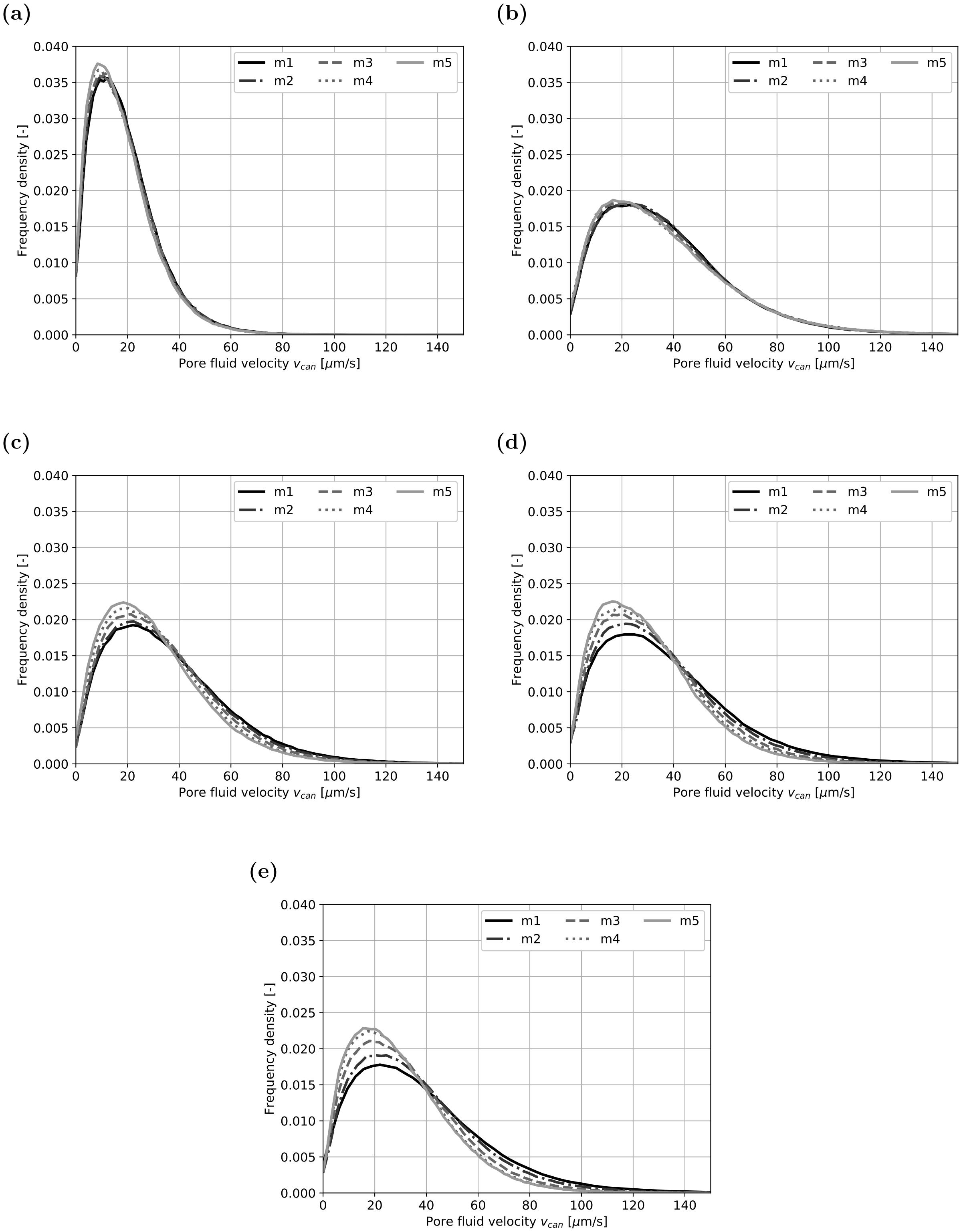

Fig. 7.5: Density histogram of the pore fluid velocity in the bone surface voxels of the trabecular bone regions over time in the **(a)** sham-loading/control group **(b)** static-loading group **(c)** 2 Hz dynamic-loading group **(d)** 5 Hz dynamic-loading group **(e)** 10 Hz dynamic-loading group.

(a)

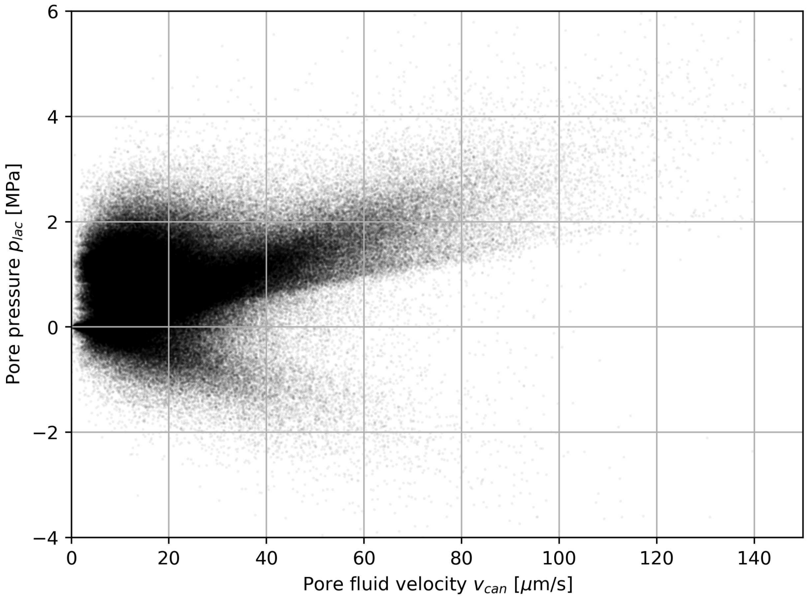

(b)

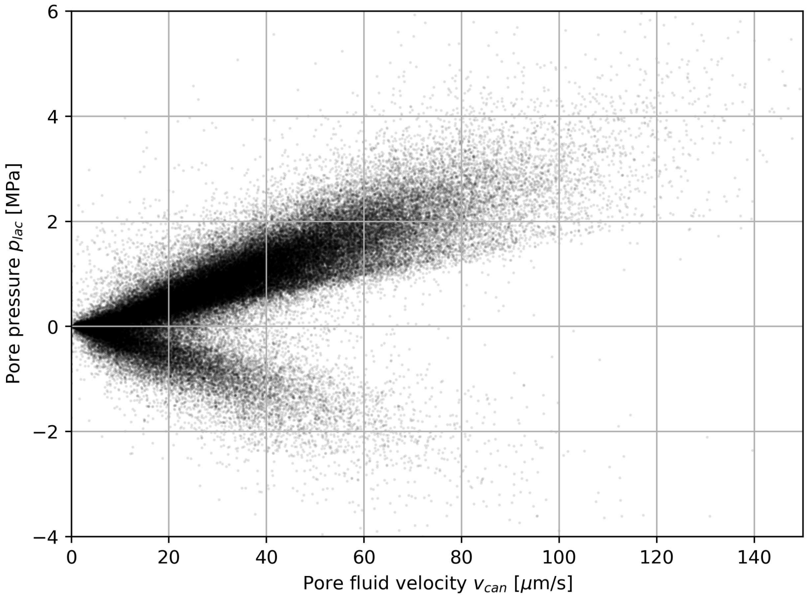

Fig. 7.6: Scatter plot of lacunar pore pressure and canalicular pore fluid velocity in **(a)** all bone voxels **(b)** all bone surface voxels. Sample: Week m1, Mouse 02, 10 Hz dynamic-loading group.

Chapter 8

Discussion

Image processing

An automated, equivalent image processing pipeline was established, which was extended with several ways to perform data analyses. The very small differences which occur, can be neglected, because they do not influence the results. As shown, registering the two halves of the vertebrae separately does not improve the visual results or the area under the ROC curve (AUC). Instead, it causes some problems with enlarging or trimming vertebrae in longitudinal direction. Given these points, registering the two halves separately is not a suitable approach.

Frequency dependency of bone adaptation

Static loading does not result in an increase of bone volume, see Fig. 4.2 and 4.7, also because it does not decrease bone resorption rate (BRR), see Fig. 4.3(b). This is consistent with other literature [106]. When superimposing static with physiological, dynamic load an adaptation seems to take place [107, 108]. Whether static loading causes bone loss cannot be concluded with certainty, but similar patterns have been reported before [109]. Hypoxia in osteocytes could be a reason for lacking decrease of bone resorption and suppressive effects on bone apposition [10, 109].

The differences in bone adaptation due to frequency can be explained by differences in strain rate, number of loading cycles and possibly strain amplification [25, 52, 53, 110]. However, the number of loading cycles probably has less impact, due to the high number of cycles even in the 2 Hz dynamic-loading group (600 cycles) [45, 110]. The temporal progression of bone net adaptation rate (BFR-BRR), see Fig. 4.3(c), and bone volume fraction (BV/TV), see Fig. 4.2(a), raises the question whether higher frequencies lead to faster bone adaptation or greater long-term bone adaptation.

The logarithmic frequency dependency of bone adaptation, observed in several parameters, might also be linked to the variable fluid flow between groups [112]. Notably, the strain rate is speculated to act as on of the influencers of fluid flow [111]. Similarly for other mechanical stimuli, a logarithmic or quadratic dependency on loading frequency has been reported before [56].

It was hypothesised that the greatest bone adaptation in cortical bone would be between 5–10 Hz, which has been confirmed in this study and could be also seen in trabecular bone [54]. In addition, it would be interesting to investigate a possible, inverted U-shaped relation between bone adaptation and loading frequency considering higher loading frequencies. In this case, a verification between applied and incoming loading frequencies should be conducted [48]. As fluid flow is also interacting with the porosity, there might be an optimal loading frequency for bone adaptation [54, 113]. In general, trabecular and cortical bone seem to respond to similar mechanical stimuli, with the option of small differences between parameters for greatest bone adaptation, see Fig. 4.2 and 4.7. Limitations when comparing the frequency dependency of cortical and trabecular bone are the high responders in the 5 Hz dynamic-loading group and lower parameter values in measurement m1 of the 5 Hz dynamic-loading group, leading to greater adaptation in the following weeks.

An applied, dynamic loading increased mineralising surface (MS) is also observed in other studies [114, 115]. This increase and a decrease in eroded surface (ES) is in accordance with the down-regulated expression of bone resorption and up-regulated expression of bone formation marker genes [116]. Furthermore, the exact frequency seems to play a role in this interaction, see Fig. 4.5. This work also suggests that the net bone formation rate (BFR-BRR) is linked to change in net active surface (MS-ES) rather than an increase of mineral apposition rate (MAR), see Fig. 4.6.

The bone morphometric and especially the dynamic morphometric parameters are limited by the way they are calculated. A triangulated mesh is generated to calculate these parameters. Depending on the algorithm, this can potentially cause problems with big curvatures, e.g. the trabeculae, and small or thin volumes, i.e. 3D formation and resorption regions. These volumes are the basis for the calculation of the dynamic parameters. Furthermore, the biochemical activity of the pin material was not tested, but would influence all groups equally.

Correlation of SED and its gradient with local bone (re)modelling behaviour

The conditional probabilities are in accordance with previous studies [50]. The (re)modelling rules in cortical and trabecular bone seem to be slightly different. Cortical bone appears to be more sensitive to mechanical stimuli, at least in case of dynamic loading.

In general, the differences in conditional probability between SED and its gradient (∇SED) are marginal. Dynamic loading evidently decreases the probability of non-targeted bone (re)modelling, which leads to an increase in bone formation and decrease in bone resorption for high SED values, see Fig. 5.5 and 5.6. Due to the differing mechanical stimuli in dynamic loading groups, regions of non-targeted bone (re)modelling rather tend towards bone formation. As bone is adapting and local mechanical stimuli, i.e. SED values become lower, this effect diminishes.

In contrast, the difference in conditional probability for the SED gradient between groups is not that distinct. ∇SED does not have a clear interpretation, because it is influenced by stress and strain. In previous studies the volumetric strain gradient was used to predict fluid flow, which makes sense because this directly calculates the change in volume between two locations, which therefore could drive fluid flow. There are still reasons why the SED gradient might give useful results, because it considers the SED values of surrounding voxels, which gives information of a broader mechanical environment. The distribution of SED in the bone marrow visually gives an impression of an even broader mechanical environment. The SED gradient partially considers this distribution. The higher sensitivity to ∇SED can be explained by the broader mechanical environment, which is observed. A higher sensitivity means a stronger correlation between bone region and mechanical quantity.

Limitations lie in the FE analyses, where bone is assumed to be a homogeneous material with linear elastic, isotropic mechanical behaviour. The applied load is static, because the FE solver could not handle dynamic loads. Frequency-dependent quantities could therefore not be investigated. From which the questions arises whether SED is suitable to use as a single, predicting quantity to combine different loading parameters, i.e. SED does not change with loading frequency. Applying the load with a disc is sufficient for the trabecular bone, but causes errors when analysing cortical bone. A different approach is required when studying adaptation of cortical bone in the future.

Area under the ROC curve (AUC)

The differences between groups can be explained by the amount of non-targeted bone (re)modelling, which is lower in dynamic-loading groups (2 Hz, 5 Hz, 10 Hz). Due to the differing mechanical stimuli in dynamic-loading groups, regions of random (re)modelling behaviour rather tend towards bone formation. This increases the modelling performance of SED and its gradient (∇SED) and therefore, the AUC values for resorption and formation region. Why the SED gradient has a better performance modelling resorption and formation is more difficult to argue. The reasons are probably similar to the reasoning of the conditional probability, because it considers the SED values of surrounding voxels and therefore partially the SED distribution in the marrow.

Due to the way in which formation and resorption regions are defined and calculated, a voxel overlap occurs. When calculating the AUC and the correlation of SED values with bone (re)modelling the bone formation volumes are dilated, while for the SED gradient the resorption bone volumes are dilated. The overlap could introduce noise to the AUC calculation. Furthermore, variations in the modelling performance arise, because the region size have an influence when evaluating the AUC, i.e. greater relative size (more voxels) in a region results in higher AUC values for that region.

Lacunar pore pressure fields

The lacunar pore pressure calculated in this work is greater than what is known to stimulate bone cells and greater than what was reported by Scheiner et al. [23]. The differences can be primarily explained by the great variation of input strains. The relation between input strains and lacunar pore pressure is (multi)linear.

The estimated strain from the FE analysis on the whole vertebra in longitudinal direction is about -320×10^{-6}. The input strains in the model are up to -750×10^{-6}, see Fig. 6.3(b). Scheiner et al. used strains of -10×10^{-6} from a gait analysis. Small strains ($< -10 \times 10^{-6}$) occur more frequently over the day, while large strains from high impact activity ($> -1000 \times 10^{-6}$) only happen a few times over the day [117], e.g. jumping from a platform can cause strains up to -600×10^{-6} in mice [44]. In fact, strains up to -3000×10^{-6} for high impact activities were reported [118]. Lacunar pore pressure is estimated up to 24 atm (2.43 MPa) for high strain rates (impact loading) [119]. This raises the question on whether even infrequent large strain can cause and are necessary for long-term bone adaptation. In addition, not only pressure itself is bone cell-stimulating, but could also play a roll in the strain amplification at the level of single lacuna.

One limitation is that osteocyte lacunar are not spherical [94], but this should not influence the results significantly. Pursuing this point, it would be interesting to evaluate the strain distribution in an ellipsoidal lacunar pore arising from hydrostatic pore pressure.

Canalicular fluid flow

The amount of mechanical force applied to the bone can directly be linked to the fluid velocity, see Fig. 7.4. The estimated canalicular fluid velocity values lie in the range of what was estimated before [29, 120–122]. The range up to 120 μm/s is not bone cell-stimulating by itself (summary of values in [29]).

The results in Section 4 suggest that dynamic loading is necessary for bone adaptation. One of the main differences between static and dynamic loading is the amount of canalicular fluid flow. Fluid flow and the resulting shear stress could therefore be key mechanical stimuli, when combined with other mechanical stimuli, e.g. lacunar pore pressure or deformations of the lacuno-canalicular network.

The theoretical foundation of permeability tensors, used for calculating the pore pressure gradient concentration tensor, could be applied to estimate the input permeability in poroelastic FE analysis models [113].

It was not possible to see differences between the dynamic-loading groups. The model is reliant on the FE analysis results, which are calculated for a static load. A FE analysis model considering poroviscoelastic material behaviour might be beneficial.

Conclusion

In conclusion it could be shown that dynamic loading is needed to induce bone adaptation. In order to maximize bone adaptation, a loading frequency from a certain range (5–10 Hz) is ideally applied. This range could possibly originate from the poroviscoelasticity of bone and the corresponding fluid motion. Furthermore, infrequent impact loading with high strain rates could be a key component of bone adaptation. High strain rates cause higher direct mechanical strains, and great lacunar pore pressure, which both influence bone adaptation positively.

Bibliography

[1] J. F. Vincent. *Structural Biomaterials*. London: The Macmillan Press Ltd, 1982.

[2] M. Elices, ed. *Structural biological materials. Design and structure-property relationships*. Oxford: Pergamon, 2000.

[3] R. L. Drake, A. W. Vogl, and A. W. Mitchell. *Gray's Anatomy for Students*. 3rd ed. Philadelphia, PA: Churchill Livingstone, 2015.

[4] J. Wolff. *The Law of Bone Remodelling*. Berlin: Springer-Verlag Berlin Heidelberg, 1986.

[5] J. P. Bilezikian, L. G. Raisz, and T. J. Martin-Third, eds. *Principles of Bone Biology*. 3rd ed. Elsevier Inc., 2008.

[6] J. Nagatomi. *Mechanobiology Handbook*. Boca Raton: CRC Press, 2011.

[7] J. Buckwalter, M. Glimcher, R. Cooper, and R. Recker. "Bone biology. Part II: formation, form, modeling, remodeling, and regulation of cell function". In: *The Journal of Bone and Joint Surgery* 77-A.8 (1995), pp. 1276–1289.

[8] L. F. Bonewald. "The amazing osteocyte". In: *Journal of Bone and Mineral Research* 26.2 (2011), pp. 229–238.

[9] D. B. Burr, R. B. Martin, M. B. Schaffler, and E. L. Radin. "Bone remodeling in response to in vivo fatigue microdamage". In: *Journal of Biomechanics* 18.3 (1985), pp. 189–200.

[10] J. S. Dodd, J. A. Raleigh, and T. Gross. "Osteocyte hypoxia: a novel mechanotransduction pathway". In: *American Journal of Physiology* 277.3 (1999), pp. C598–C602.

[11] J. E. Compston. "Sex steroids and bone". In: *Physiological Reviews* 81.1 (2001), pp. 419–447.

[12] N. Rosa, R. Simoes, F. D. Magalhães, and A. T. Marques. "From mechanical stimulus to bone formation: a review". In: *Medical Engineering and Physics* 37.8 (2015), pp. 719–728.

[13] M. I. Pastrama, S. Scheiner, P. Pivonka, and C. Hellmich. “A mathematical multiscale model of bone remodeling, accounting for pore space-specific mechanosensation”. In: *Bone* 107 (2018), pp. 208–221.

[14] J. Wang, D. Lü, D. Mao, and M. Long. “Mechanomics: an emerging field between biology and biomechanics”. In: *Protein and Cell* 5.7 (2014), pp. 518–531.

[15] C. R. Jacobs, S. Temiyasathit, and A. B. Castillo. “Osteocyte mechanobiology and pericellular mechanics”. In: *Annual Review of Biomedical Engineering* 12.1 (2010), pp. 369–400.

[16] A. Santos, A. D. Bakker, and J. Klein-Nulend. “The role of osteocytes in bone mechanotransduction”. In: *Osteoporosis International* 20 (2009), pp. 1027–1031.

[17] S. D. Tan, T. J. de Vries, A. M. Kuijpers-Jagtman, C. M. Semeins, V. Everts, and J. Klein-Nulend. “Osteocytes subjected to fluid flow inhibit osteoclast formation and bone resorption”. In: *Bone* 41.5 (2007), pp. 745–751.

[18] M. L. Knothe Tate. “"Whither flows the fluid in bone?" An osteocyte’s perspective”. In: *Journal of Biomechanics* 36.10 (2003), pp. 1409–1424.

[19] S. C. Cowin. “Mechanosensation and fluid transport in living bone”. In: *Journal of Musculoskeletal Neuronal Interactions* 2.3 (2002), pp. 256–260.

[20] J. Klein-Nulend, A. Van der Plas, C. M. Semeins, N. E. Ajubi, J. A. Frangos, P. J. Nijweide, and E. H. Burger. “Sensitivity of osteocytes to biomechanical stress in vitro”. In: *FASEB Journal* 9.5 (1995), pp. 441–445.

[21] C. Liu, Y. Zhao, W. Y. Cheung, R. Gandhi, L. Wang, and L. You. “Effects of cyclic hydraulic pressure on osteocytes”. In: *Bone* 46.5 (2010), pp. 1449–1456.

[22] J. R. Henstock, M. Rotherham, J. B. Rose, and A. J. El Haj. “Cyclic hydrostatic pressure stimulates enhanced bone development in the foetal chick femur in vitro”. In: *Bone* 53.2 (2013), pp. 468–477.

[23] S. Scheiner, P. Pivonka, and C. Hellmich. “Poromicromechanics reveals that physiological bone strains induce osteocyte-stimulating lacunar pressure”. In: *Biomechanics and Modeling in Mechanobiology* 15.1 (2016), pp. 9–28.

[24] G. R. Paul, A. Malhotra, and R. Müller. “Mechanical stimuli in the local in vivo environment in bone: computational approaches linking organ-scale loads to cellular signals”. In: *Current Osteoporosis Reports* 16.4 (2018), pp. 395–403.

[25] L. Wang, J. Dong, and C. J. Xian. “Strain amplification analysis of an osteocyte under static and cyclic loading: a finite element study”. In: *BioMed Research International* 2015 (2015).

[26] A. Rath Bonivtch, L. F. Bonewald, and D. P. Nicolella. “Tissue strain amplification at the osteocyte lacuna: a microstructural finite element analysis”. In: *Journal of Biomechanics* 40.10 (2007), pp. 2199–2206.

[27] C. Hellmich, J. F. Barthélémy, and L. Dormieux. “Mineral-collagen interactions in elasticity of bone ultrastructure - a continuum micromechanics approach”. In: *European Journal of Mechanics, A/Solids* 23.5 (2004), pp. 783–810.

[28] C. Hellmich, D. Celundova, and F.-J. Ulm. “Multiporoelasticity of Hierarchically Structured Materials: Micromechanical Foundations and Application to Bone”. In: *Journal of Engineering Mechanics* 135.5 (2009), pp. 382–394.

[29] S.-J. Estermann and S. Scheiner. “Multiscale modeling provides differentiated insights to fluid flow-driven stimulation of bone cellular activities”. In: *Frontiers in Physics* 6.76 (2018).

[30] B. Aoubiza, J. M. Crolet, and A. Meunier. “On the mechanical characterization of compact bone structure using the homogenization theory”. In: *Journal of Biomechanics* 29.12 (1996), pp. 1539–1547.

[31] J. M. Crolet, B. Aoubiza, and A. Meunier. “Compact bone: Numerical simulation of mechanical characteristics”. In: *Journal of Biomechanics* 26.6 (1993), pp. 677–687.

[32] L. Dormieux, D. Kondo, and F.-J. Ulm. *Microporomechanics*. Chichester: John Wiley and Sons, Ltd., 2006.

[33] S. C. Cowin. “Bone poroelasticity. Survey Article”. In: *Journal of Biomechanics* 32 (1999), pp. 217–238.

[34] A. Scheuren, E. Wehrle, F. Flohr, and R. Müller. “Bone mechanobiology in mice: toward single-cell in vivo mechanomics”. In: *Biomechanics and Modeling in Mechanobiology* 16.6 (2017), pp. 2017–2034.

[35] Hart R T, Davy D T, and Heiple K G. “A computational method for stress analysis of adaptive elastic materials with a view toward applications in strain-induced bone remodeling”. In: *Journal of Biomechanical Engineering* 106.4 (1984), pp. 342–350.

[36] D. R. Carter, T. E. Orr, and D. P. Fyhrie. “Relationships between loading history and femoral cancellous bone architecture”. In: *Journal of Bomechanics* 22.3 (1989), pp. 231–244.

[37] T. E. D. S. Gross, J. L. Edwards, K. J. Mcleod, and C. T. Rubin. “Strain gradients correlate with sites of exercise”. In: *Journal of Bone and Mineral Research* 12.6 (1997), pp. 982–988.

[38] R. Huiskes, R. Ruimerman, G. H. van Lenthe, and J. D. Janssen. “Effects of mechanical forces on maintenance and adaptatin of form in trabecular bone”. In: *Nature* 405.6787 (2000), pp. 704–706.

[39] J. H. Waarsing, J. S. Day, J. C. V. D. Linden, A. G. Ederveen, C. Spanjers, N. D. Clerck, A. Sasov, J. A. N. Verhaar, and H. Weinans. “Detecting and tracking local changes in the tibiae of individual rats : a novel method to analyse longitudinal in vivo micro-CT data”. In: *Bone* 34 (2004), pp. 163–169.

[40] M. L. Bouxsein, S. K. Boyd, B. A. Christiansen, R. E. Guldberg, K. J. Jepsen, and R. Müller. “Guidelines for assessment of bone microstructure in rodents using micro-computed tomography”. In: *Journal of Bone and Mineral Research* 25.7 (2010), pp. 1468–1486.

[41] C. H. Turner, M. R. Forwood, J. Y. Rho, and T. Yoshikawa. “Mechanical loading thresholds for lamellar and woven bone formation”. In: *Journal of Bone and Mineral Research* 9.1 (1994), pp. 87–97.

[42] J. R. Mosley, B. M. March, J. Lynch, and L. E. Lanyon. “Strain magnitude related changes in whole bone architecture in growing rats”. In: *Bone* 20.3 (1997), pp. 191–198.

[43] T. S. Gross, S. Srinivasan, C. C. Liu, and T. L. Clemens. “Noninvasive loading of the murine tibia: an in vivo model for the study of mechanotransduction”. In: *Journal of Bone and Mineral Research* 17.3 (2002), pp. 493–501.

[44] R. L. De Souza, M. Matsuura, F. Eckstein, S. C. Rawlinson, L. E. Lanyon, and A. A. Pitsillides. “Non-invasive axial loading of mouse tibiae increases cortical bone formation and modifies trabecular organization: a new model to study cortical and cancellous compartments in a single loaded element”. In: *Bone* 37.6 (2005), pp. 810–818.

[45] Y. Umemura, T. Ishiko, T. Yamauchi, M. Kurono, and S. Mashiko. “Five jumps per day increase bone mass and breaking force in rats”. In: *Journal of Bone and Mineral Research* 12.9 (1997), pp. 1480–1485.

[46] J. M. Wallace, R. M. Rajachar, M. R. Allen, S. A. Bloomfield, P. G. Robey, M. F. Young, and D. H. Kohn. “Exercise-induced changes in the cortical bone of growing mice are bone- and gender-specific”. In: *Bone* 40.4 (2007), pp. 1120–1127.

[47] T. J. Chambers, M. Evans, T. N. Gardner, A. Turner-Smith, and J. W. Chow. “Induction of bone formation in rat tail vertebrae by mechanical loading”. In: *Bone and Mineral* 20.2 (1993), pp. 167–178.

[48] D. J. Webster, P. L. Morley, G. H. van Lenthe, and R. Müller. "A novel in vivo mouse model for mechanically stimulated bone adaptation – a combined experimental and computational validation study". In: *Computer Methods in Biomechanics and Biomedical Engineering* 11.5 (2008), pp. 435–441.

[49] K. M. Melville, A. G. Robling, and M. C. van der Meulen. "In vivo axial loading of the mouse tibia". In: *Methods in Molecular Biology* 1226 (2015), pp. 99–115.

[50] F. A. Schulte, D. Ruffoni, F. M. Lambers, D. Christen, D. J. Webster, G. Kuhn, and R. Müller. "Local Mechanical Stimuli Regulate Bone Formation and Resorption in Mice at the Tissue Level". In: *PLoS ONE* 8.4 (2013).

[51] C. T. Rubin and L. E. Lanyon. "Regulation of bone mass by mechanical strain magnitude". In: *Calcified Tissue International* 37.4 (1985), pp. 411–417.

[52] C. H. Turner, I. Owan, and Y. Takano. "Mechanotransduction in bone: role of strain rate". In: *American Journal of Physiology* 269.3.1 (1995), E438–E442.

[53] J. R. Mosley and L. E. Lanyon. "Strain rate as a controlling influence on adaptive modeling in response to dynamic loading of the ulna in growing male rats". In: *Bone* 23.4 (1998), pp. 313–318.

[54] S. J. Warden and C. H. Turner. "Mechanotransduction in the cortical bone is most efficient at loading frequencies of 5-10 Hz". In: *Bone* 34.2 (2004), pp. 261–270.

[55] F. Mcdonald, A. L. Yettram, and K. Macleod. "The response of bone to external loading regimen". In: *Medical Engineering and Physics* 16 (1994), pp. 384–397.

[56] C. H. Turner, M. R. Forwood, and M. W. Otter. "Mechanotransduction in bone: do bone cells act as sensors of fluid flow?" In: *FASEB Journal* 8.11 (1994), pp. 875–878.

[57] F. M. Lambers, G. Kuhn, C. Weigt, K. M. Koch, F. A. Schulte, and R. Müller. "Bone adaptation to cyclic loading in murine caudal vertebrae is maintained with age and directly correlated to the local micromechanical environment". In: *Journal of Biomechanics* 48.6 (2015), pp. 1179–1187.

[58] W. K. Pratt. *Digital Image Processing*. 3rd ed. New York: John Wiley and Sons, Inc., 2001, p. 738.

[59] E. Reinhard, G. Ward, S. Pattanaik, P. Debevec, W. Heidrich, and K. Myszkowski. *High Dynamic Range Imaging*. 2nd ed. Burlington, USA: Elsevier Inc., 2010, p. 650.

[60] F. M. Lambers, F. A. Schulte, G. Kuhn, D. J. Webster, and R. Müller. "Mouse tail vertebrae adapt to cyclic mechanical loading by increasing bone formation rate and decreasing bone resorption rate as shown by time-lapsed in vivo imaging of dynamic bone morphometry". In: *Bone* 49.6 (2011), pp. 1340–1350.

[61] F. M. Lambers, K. Koch, G. Kuhn, D. Ruffoni, C. Weigt, F. A. Schulte, and R. Müller. “Trabecular bone adapts to long-term cyclic loading by increasing stiffness and normalization of dynamic morphometric rates”. In: *Bone* 55.2 (2013), pp. 325–334.

[62] K. K. Nishiyama, G. M. Campbell, R. J. Klinck, and S. K. Boyd. “Reproducibility of bone micro-architecture measurements in rodents by in vivo micro-computed tomography is maximized with three-dimensional image registration”. In: *Bone* 46.1 (2010), pp. 155–161.

[63] L. Shapiro and G. Stockman. *Computer Vision*. 1st ed. Upper Saddle River, New Jersey: Prentice Hall, Inc., 2001, p. 638.

[64] J. H. Waarsing, J. S. Day, and H. Weinans. “An improved segmentation method for in vivo μCT imaging”. In: *Journal of Bone and Mineral Research* 19.10 (2004), pp. 1640–1650.

[65] B. A. Christiansen. “Effect of micro-computed tomography voxel size and segmentation method on trabecular bone microstructure measures in mice”. In: *Bone Reports* 5 (2016), pp. 136–140.

[66] M. Ding, A. Odgaard, and I. Hvid. “Accuracy of cancellous bone volume fraction measured by micro-CT scanning”. In: *Journal of Biomechanics* 32.3 (1999), pp. 323–326.

[67] C. A. Glasbey. “An analysis of histogram-based thresholding algorithms”. In: *CVGIP: Graphical Models and Image Processing* 55.6 (Nov. 1993), pp. 532–537.

[68] J. Weszka, R. Nagel, and A. Rosenfeld. “A threshold selection technique”. In: *IEEE Transcations on Computers* 23.December (1974), pp. 1322–1326.

[69] K. L. Beaucage, S. I. Pollmann, S. M. Sims, S. J. Dixon, and D. W. Holdsworth. “Quantitative in vivo micro-computed tomography for assessment of age-dependent changes in murine whole-body composition”. In: *Bone Reports* 5 (2016), pp. 70–80.

[70] J. J. Moré, B. S. Garbow, and K. E. Hillstrom. *User guide for MINPACK-1*. 1980. URL: `http://cdsweb.cern.ch/record/126569` (visited on 09/22/2019).

[71] L. Mulder, J. H. Koolstra, J. M. den Toonder, and T. M. van Eijden. “Intratrabecular distribution of tissue stiffness and mineralization in developing trabecular bone”. In: *Bone* 41.2 (2007), pp. 256–265.

[72] F. A. Schulte, F. M. Lambers, T. L. Mueller, M. Stauber, and R. Müller. *Image interpolation allows accurate quantitative bone morphometry in registered micro-computed tomography scans*. 2014.

[73] D. W. Dempster, J. E. Compston, M. K. Drezner, F. H. Glorieux, J. A. Kanis, H. Malluche, P. J. Meunier, S. M. Ott, R. R. Recker, and A. M. Parfitt. “Standardized nomenclature, symbols, and units for bone histomorphometry: a 2012 update of the report of the ASBMR Histomorphometry Nomenclature Committee”. In: *Journal of Bone and Mineral Research* 28.1 (2013), pp. 1–16.

[74] J. M. Somerville, R. M. Aspden, K. E. Armour, K. J. Armour, and D. M. Reid. “Growth of C57Bl/6 mice and the material and mechanical properties of cortical bone from the tibia”. In: *Calcified Tissue International* 74.5 (2004), pp. 469–475.

[75] R. Huiskes. “If bone is the answer, then what is the question?” In: *Journal of Anatomy* 197.2 (2000), pp. 145–156.

[76] P. Christen, B. Van Rietbergen, F. M. Lambers, R. Müller, and K. Ito. “Bone morphology allows estimation of loading history in a murine model of bone adaptation”. In: *Biomechanics and Modeling in Mechanobiology* 11.3-4 (2012), pp. 483–492.

[77] C. Flaig. *ParOSol*. URL: `https://bitbucket.org/cflaig/parosol/src/default/` (visited on 10/19/2019).

[78] R. H. Kufahl and S. Saha. “A theoretical model for stress-generated fluid flow in the canaliculi-lacunae network in bone tissue”. In: *Journal of Biomechanics* 23.2 (1990), pp. 171–180.

[79] D. Webster, F. A. Schulte, F. M. Lambers, G. Kuhn, and R. Müller. “Strain energy density gradients in bone marrow predict osteoblast and osteoclast activity: a finite element study”. In: *Journal of Biomechanics* 48.5 (2015), pp. 866–874.

[80] J. Fogarty, R. S. Baker, and S. E. Hudson. “Case studies in the use of ROC curve analysis for sensor-based estimates in human computer interaction”. In: *Proceedings of Graphics Interface* (2005), pp. 129–136.

[81] S. J. Mason and N. E. Graham. “Areas beneath the relative operating characteristics (ROC) and relative operating levels (ROL) curves: statistical significance and interpretation”. In: *Quarterly Journal of the Royal Meteorological Society* 128 (2002), pp. 2145–2166.

[82] R. L. Jilka. “The relevance of mouse models for investigating age-related bone loss in humans”. In: *Journals of Gerontology - Series A Biological Sciences and Medical Sciences* 68.10 (2013), pp. 1209–1217.

[83] H. Hemmatian, M. R. Laurent, S. Ghazanfari, D. Vanderschueren, A. D. Bakker, J. Klein-Nulend, and G. H. Van Lenthe. “Accuracy and reproducibility of mouse cortical bone microporosity as quantified by desktop microcomputed tomography”. In: *PLoS ONE* 12.8 (2017).

[84] L. M. Calvi, N. A. Sims, J. L. Hunzelman, M. C. Knight, A. Giovannetti, J. M. Saxton, H. M. Kronenberg, R. Baron, and E. Schipani. “Activated parathyroid hormoneparathyroid hormone-related protein receptor in osteoblastic cells differentially affects cortical and trabecular bone”. In: *The Journal of Clinical Investigation* 107.3 (2001), pp. 277–286.

[85] G. Jadhav, D. Teguh, J. Kenny, J. Tickner, and J. Xu. “Morc3 mutant mice exhibit reduced cortical area and thickness, accompanied by altered haematopoietic stem cells niche and bone cell differentiation”. In: *Scientific Reports* 6.April (2016), pp. 1–13.

[86] B. Hesse, P. Varga, M. Langer, A. Pacureanu, S. Schrof, N. Männicke, H. Suhonen, P. Maurer, P. Cloetens, F. Peyrin, and K. Raum. “Canalicular network morphology is the major determinant of the spatial distribution of mass density in human bone tissue: evidence by means of synchrotron radiation phase-contrast nano-CT”. In: *Journal of Bone and Mineral Research* 30.2 (2015), pp. 346–356.

[87] R. Hill. “Elastic properties of reinforced solids: some theoretical principles”. In: *Journal of the Mechanics and Physics of Solids* 11.5 (1963), pp. 357–372.

[88] A. Zaoui. “Continuum micromechanics: survey”. In: *Journal of Engineering Mechanics* 128.8 (2002), pp. 808–816.

[89] W. J. Drugan and J. R. Willis. “A micromechanics-based nonlocal constitutive equation and estimates of representative volume element size for elastic composites”. In: *Journal of the Mechanics and Physics of Solids* 44.4 (1996), pp. 497–524.

[90] C. Kohlhauser and C. Hellmich. “Ultrasonic contact pulse transmission for elastic wave velocity and stiffness determination: influence of specimen geometry and porosity”. In: *Engineering Structures* 47 (2013), pp. 115–133.

[91] J. A. Núñez, A. Goring, E. Hesse, P. J. Thurner, P. Schneider, and C. E. Clarkin. “Simultaneous visualisation of calcified bone microstructure and intracortical vasculature using synchrotron X-ray phase contrast-enhanced tomography”. In: *Scientific Reports* 7.1 (2017).

[92] H. Mosey, J. A. Núñez, A. Goring, C. E. Clarkin, K. A. Staines, P. D. Lee, A. A. Pitsillides, and B. Javaheri. “Sost deficiency does not alter bone’s lacunar or vascular porosity in mice”. In: *Frontiers in Materials* 4.27 (2017).

[93] P. Schneider, T. Krucker, E. Meyer, A. Ulmann-Schuler, B. Weber, M. Stampanoni, and R. Müller. “Simultaneous 3D visualization and quantification of murine bone and bone vasculature using micro-computed tomography and vascular replica”. In: *Microscopy Research and Technique* 72.9 (2009), pp. 690–701.

[94] C. M. Heveran, A. Rauff, K. B. King, R. D. Carpenter, and V. L. Ferguson. “A new open-source tool for measuring 3D osteocyte lacunar geometries from confocal laser scanning microscopy reveals age-related changes to lacunar size and shape in cortical mouse bone”. In: *Bone* 110 (2018), pp. 115–127.

[95] L. D. You, S. Weinbaum, S. C. Cowin, and M. B. Schaffler. “Ultrastructure of the osteocyte process and its pericellular matrix”. In: *Anatomical Record - Part A* 278A.2 (2004), pp. 505–513.

[96] Y. Lin and S. Xu. “AFM analysis of the lacunar-canalicular network in demineralized compact bone”. In: *Journal of Microscopy* 241.3 (2011), pp. 291–302.

[97] P. Schneider, M. Meier, R. Wepf, and R. Müller. “Serial FIB/SEM imaging for quantitative 3D assessment of the osteocyte lacuno-canalicular network”. In: *Bone* 49.2 (2011), pp. 304–311.

[98] C. Morin and C. Hellmich. “A multiscale poromicromechanical approach to wave propagation and attenuation in bone”. In: *Ultrasonics* 54.5 (2014), pp. 1251–1269.

[99] B. Pichler and C. Hellmich. “Estimation of influence tensors for eigenstressed multiphase elastic media with nonaligned inclusion phases of arbitrary ellipsoidal shape”. In: *Journal of Engineering Mechanics* 136.8 (2010), pp. 1043–1053.

[100] M. Benalla, P. E. Palacio-Mancheno, S. P. Fritton, L. Cardoso, and S. C. Cowin. “Dynamic permeability of the lacunar-canalicular system in human cortical bone”. In: *Biomechanics and Modeling in Mechanobiology* 13.4 (2014), pp. 801–812.

[101] R. B. Martin, D. B. Burr, N. A. Sharkey, and D. P.-. Fyhrie. *Skeletal Tissue Mechanics*. 2nd ed. New York: Springer Science+Business Media LLC, 2015, p. 392.

[102] L. Cardoso, S. P. Fritton, G. Gailani, M. Benalla, and S. C. Cowin. “A review of recent advances in the assessment of bone porosity, permeability, and interstitial fluid flow”. In: *Journal of Biomechanics* 46.2 (2013), pp. 253–265.

[103] C. Morin, V. Vass, and C. Hellmich. “Micromechanics of elastoplastic porous polycrystals: theory, algorithm, and application to osteonal bone”. In: *International Journal of Plasticity* 91 (2017), pp. 238–267.

[104] E. J. Anderson and M. L. Knothe Tate. “Idealization of pericellular fluid space geometry and dimension results in a profound underprediction of nano-microscale stresses imparted by fluid drag on osteocytes”. In: *Journal of Biomechanics* 41.8 (2008), pp. 1736–1746.

[105] P. Schneider, M. Meier, R. Wepf, and R. Müller. “Towards quantitative 3D imaging of the osteocyte lacuno-canalicular network”. In: *Bone* 47.5 (2010), pp. 848–858.

[106] L. E. Lanyon and C. T. Rubin. “Static vs dynamic loads as an influence on bone remodelling”. In: *Journal of Biomechanics* 17.12 (1984), pp. 897–905.

[107] J. B. Meade, S. C. Cowin, J. J. Klawitter, W. C. Van Buskirk, and H. B. Skinner. “Bone remodelling due to contiuously applied loads”. In: *Calcified Tissue International* 36 (1984), pp. 25–30.

[108] P. Trisi and A. Rebaudi. “Progressive bone adaptation of titanium implants during and after orthodontic load in humans.” In: *International Journal of Periodontics & Restorative Dentistry* 22.1 (2002), pp. 31–43.

[109] A. G. Robling, K. M. Duijvelaar, J. V. Geevers, N. Ohashi, and C. H. Turner. “Modulation of appositional and longitudinal bone growth in the rat ulna by applied static and dynamic force”. In: *Bone* 29.2 (2001), pp. 105–113.

[110] C. H. Turner. “Three rules for bone adaptation to mechanical stimuli”. In: *Bone* 23.5 (1998), pp. 399–407.

[111] V. H. Nguyen, T. Lemaire, and S. Naili. “Poroelastic behaviour of cortical bone under harmonic axial loading: A finite element study at the osteonal scale”. In: *Medical Engineering and Physics* 32.4 (2010), pp. 384–389.

[112] E. Malachanne, D. Dureisseix, and F. Jourdan. “Numerical model of bone remodeling sensitive to loading frequency through a poroelastic behavior and internal fluid movements”. In: *Journal of the Mechanical Behavior of Biomedical Materials* 4.6 (2011), pp. 849–857.

[113] A. F. Pereira and S. J. Shefelbine. “The influence of load repetition in bone mechanotransduction using poroelastic finite-element models: the impact of permeability”. In: *Biomechanics and Modeling in Mechanobiology* 13.1 (2014), pp. 215–225.

[114] M. D. Brodt and M. J. Silva. “Aged mice have enhanced endocortical response and normal periosteal response compared with young-adult mice following 1 week of axial tibial compression”. In: *Journal of Bone and Mineral Research* 25.9 (2010), pp. 2006–2015.

[115] A. I. Birkhold, H. Razi, G. N. Duda, R. Weinkamer, S. Checa, and B. M. Willie. “Mineralizing surface is the main target of mechanical stimulation independent of age: 3D dynamic in vivo morphometry”. In: *Bone* 66 (2014), pp. 15–25.

[116] C. Kesavan, S. Mohan, S. Oberholtzer, J. E. Wergedal, and D. J. Baylink. “Mechanical loading-induced gene expression and BMD changes are different in two inbred mouse strains”. In: *Journal of Applied Physiology* 99.5 (2005), pp. 1951–1957.

[117] S. P. Fritton, K. J. McLeod, and C. T. Rubin. “Quantifying the strain history of bone:spatial uniformity and self-similarity of low-magnitude strains”. In: *Journal of Biomechanics* 33.3 (2000), pp. 317–325.

[118] P. J. Ehrlich and L. E. Lanyon. “Mechanical strain and bone cell function: a review”. In: *Osteoporosis International* 13 (2002), pp. 688–700.

[119] D. Zhang, S. Weinbaum, and S. C. Cowin. “Estimates of the peak pressures in bone pore water”. In: *Journal of Biomechanical Engineering* 120 (1998), pp. 697–703.

[120] R. Y. Kwon and J. A. Frangos. “Quantification of lacunar–canalicular interstitial fluid flow through computational modeling of fluorescence recovery after photobleaching”. In: *Cellular and Molecular Bioengineering* 3.3 (2010), pp. 296–306.

[121] C. Price, X. Zhou, W. Li, and L. Wang. “Real-time measurement of solute transport within the lacunar-canalicular system of mechanically loaded bone: direct evidence for load-induced fluid flow”. In: *Journal of Bone and Mineral Research* 26.2 (2011), pp. 277–285.

[122] B. Wang, X. Zhou, C. Price, W. Li, J. Pan, and L. Wang. “Quantifying load-induced solute transport and solute-matrix interaction within the osteocyte lacunar-canalicular system”. In: *Journal of Bone and Mineral Research* 28.5 (2013), pp. 1075–1086.

Appendix A

Supplementary figures

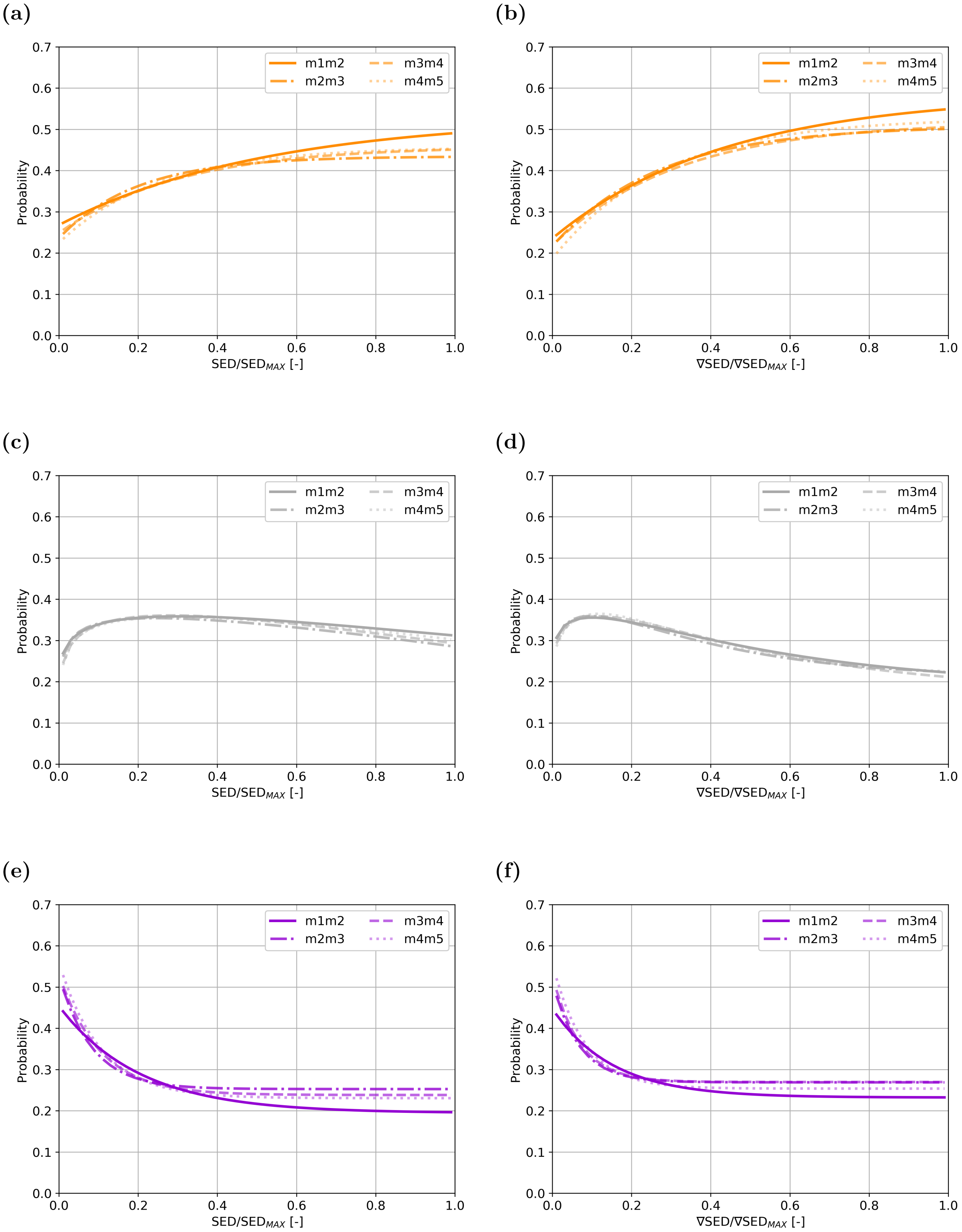

Supplementary Figure S1: Regression lines for conditional probability over time (10 Hz dynamic-loading group, trabecular bone) for: **(a)** formation, SED **(b)** formation, SED gradient **(c)** quiescence, SED **(d)** quiescence, SED gradient **(e)** resorption, SED **(f)** resorption, SED gradient

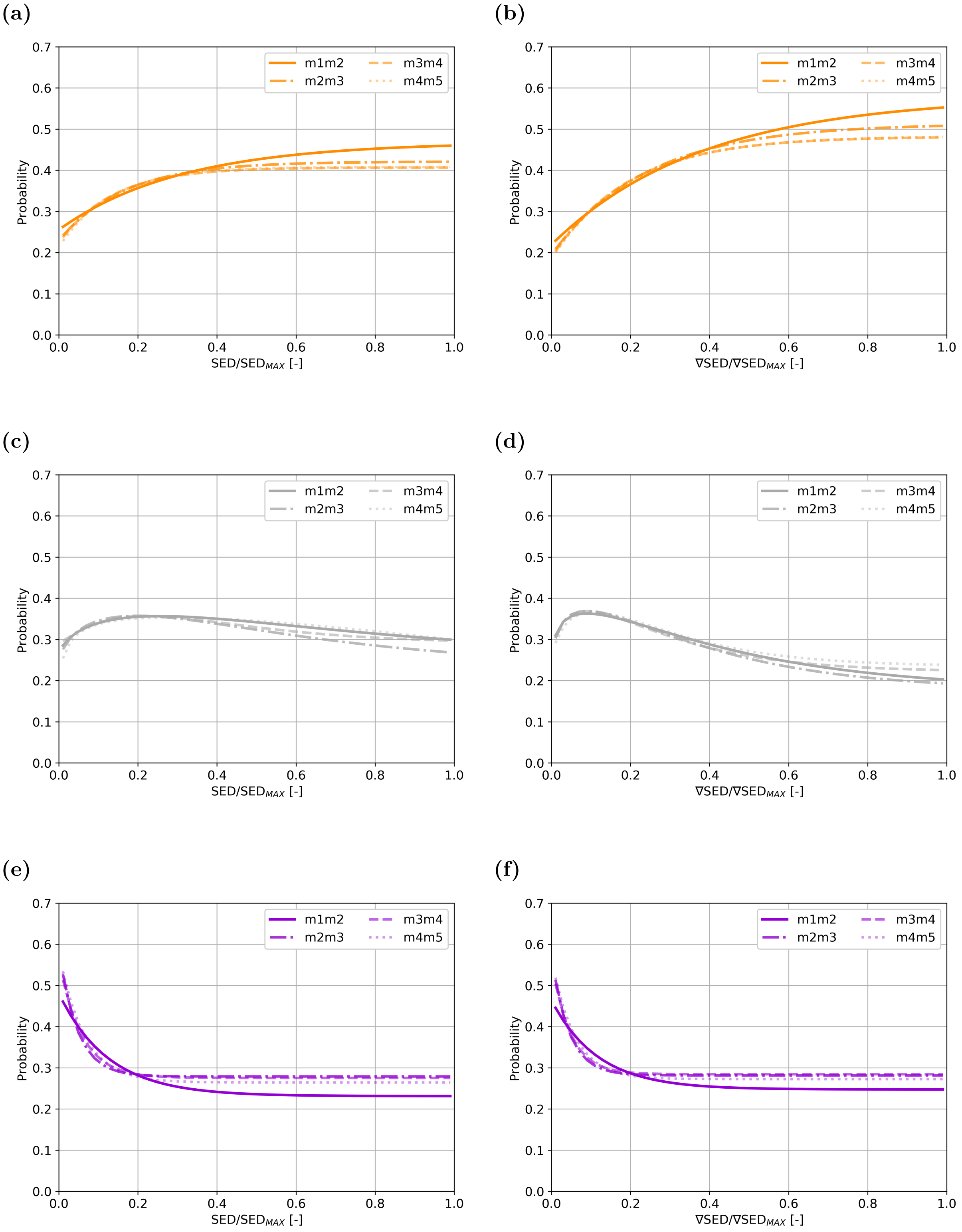

Supplementary Figure S2: Regression lines for conditional probability over time (5 Hz dynamic-loading group, trabecular bone) for: **(a)** formation, SED **(b)** formation, SED gradient **(c)** quiescence, SED **(d)** quiescence, SED gradient **(e)** resorption, SED **(f)** resorption, SED gradient

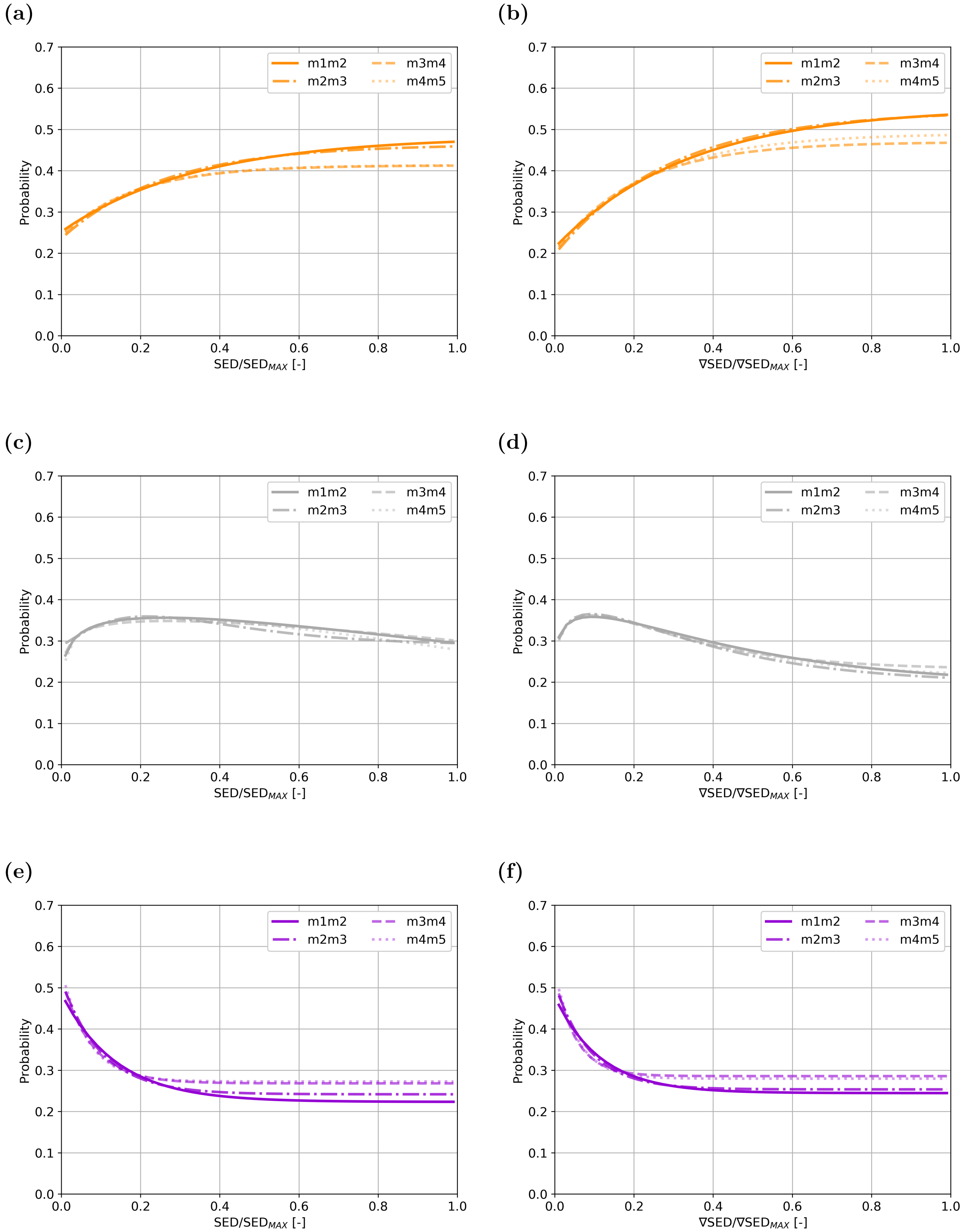

Supplementary Figure S3: Regression lines for conditional probability over time (2 Hz dynamic-loading group, trabecular bone) for: **(a)** formation, SED **(b)** formation, SED gradient **(c)** quiescence, SED **(d)** quiescence, SED gradient **(e)** resorption, SED **(f)** resorption, SED gradient

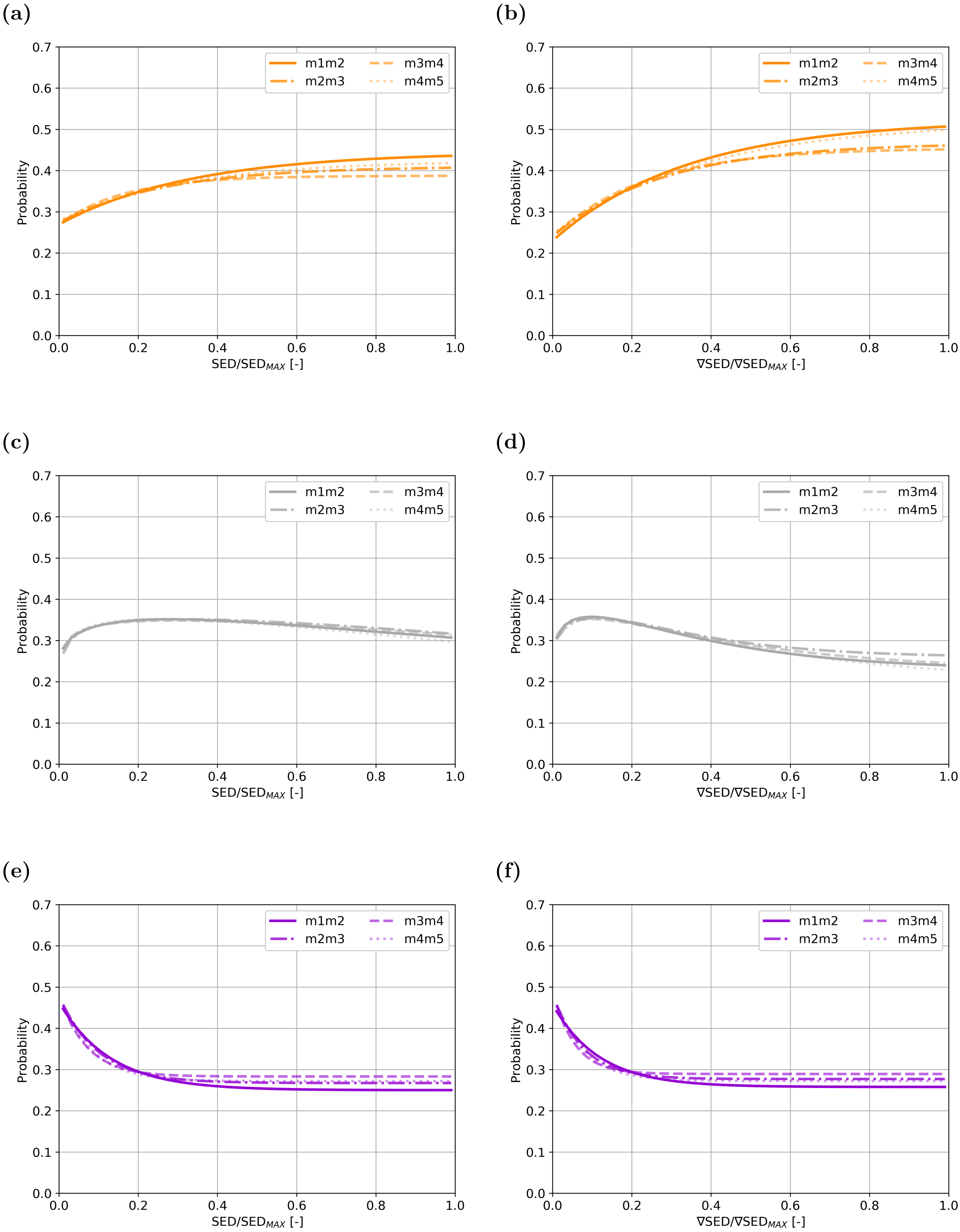

Supplementary Figure S4: Regression lines for conditional probability over time (static-loading group, trabecular bone) for: **(a)** formation, SED **(b)** formation, SED gradient **(c)** quiescence, SED **(d)** quiescence, SED gradient **(e)** resorption, SED **(f)** resorption, SED gradient

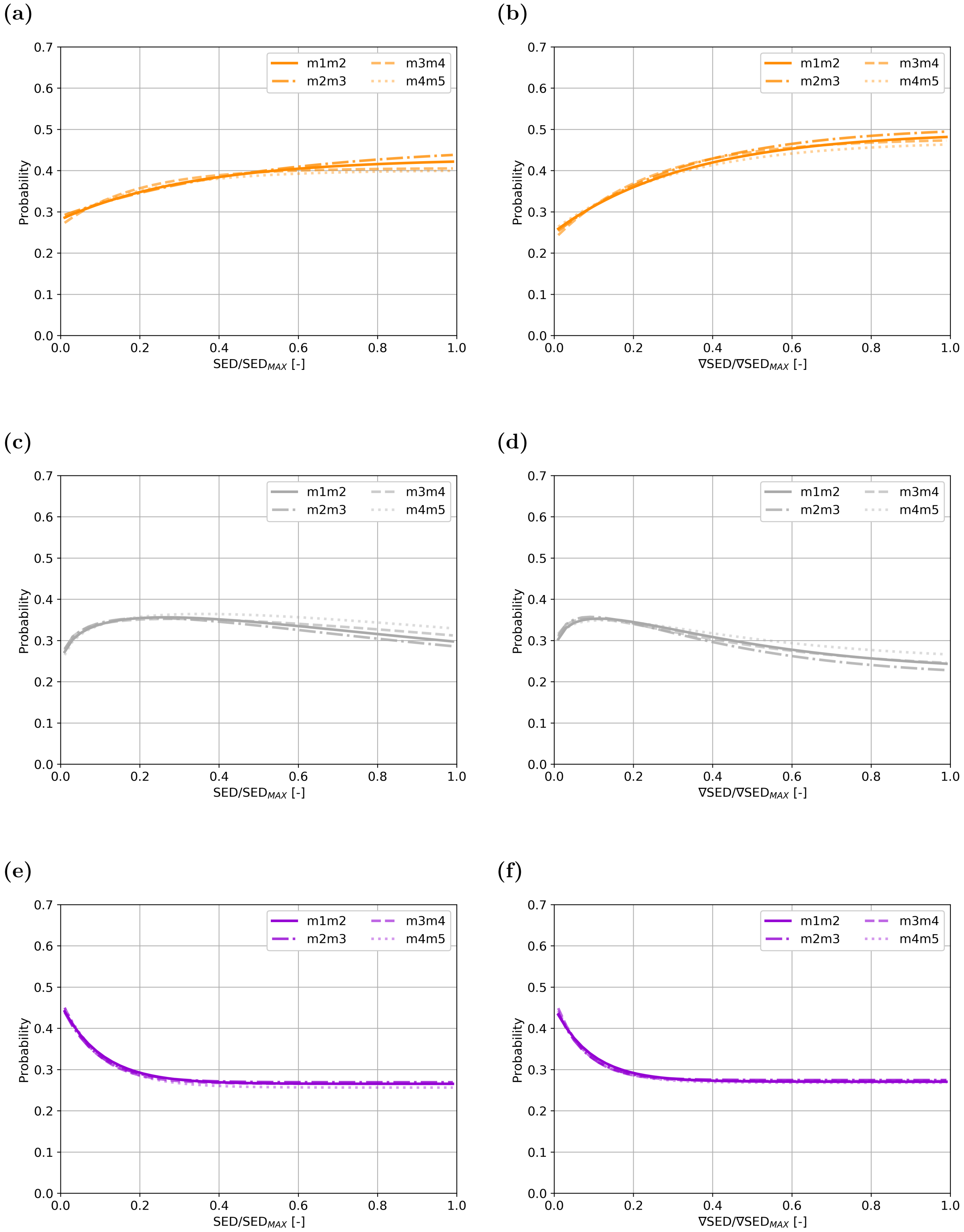

Supplementary Figure S5: Regression lines for conditional probability over time (sham-loading/control group, trabecular bone) for: **(a)** formation, SED **(b)** formation, SED gradient **(c)** quiescence, SED **(d)** quiescence, SED gradient **(e)** resorption, SED **(f)** resorption, SED gradient

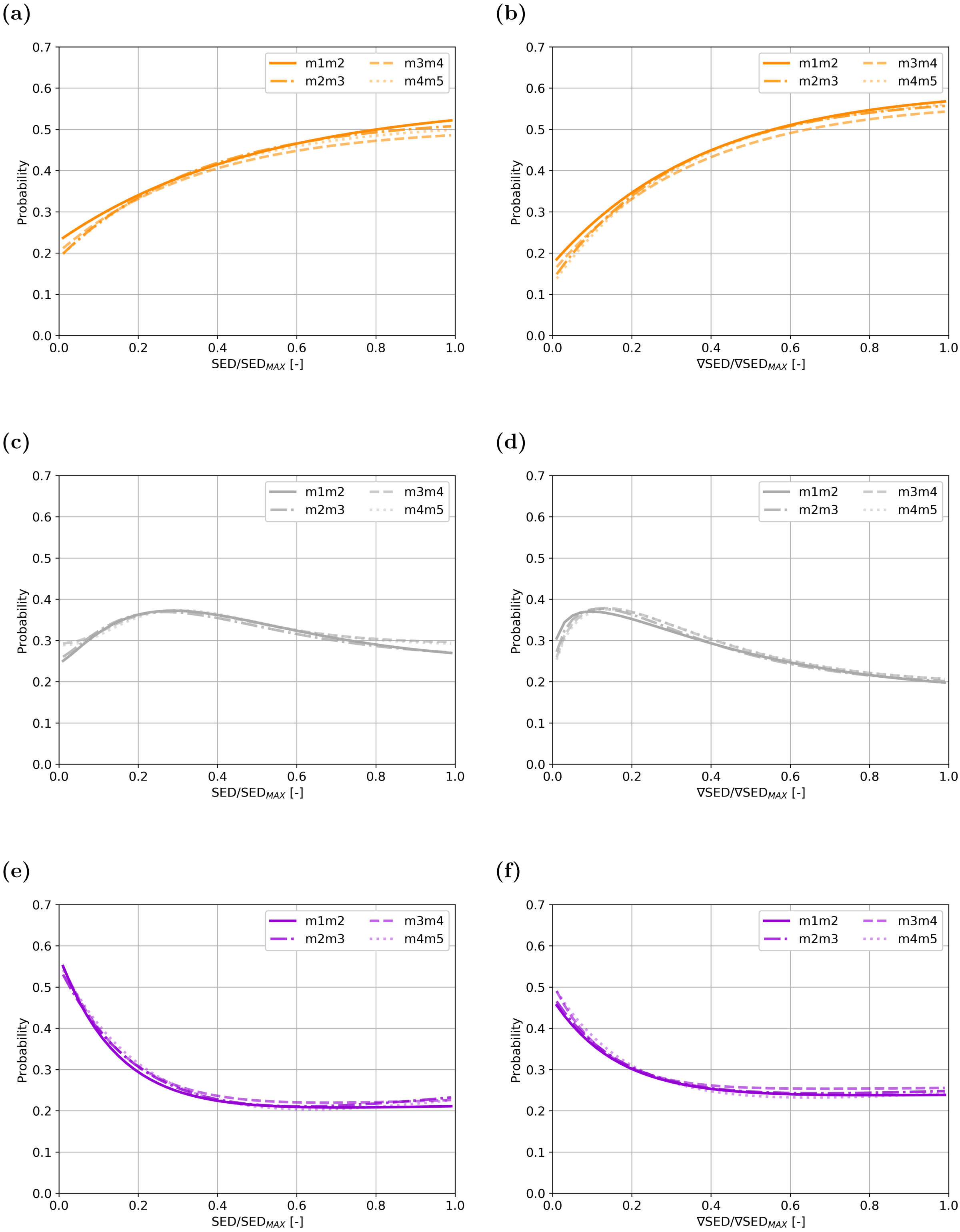

Supplementary Figure S6: Regression lines for conditional probability over time (10 Hz dynamic-loading group, cortical bone) for: **(a)** formation, SED **(b)** formation, SED gradient **(c)** quiescence, SED **(d)** quiescence, SED gradient **(e)** resorption, SED **(f)** resorption, SED gradient

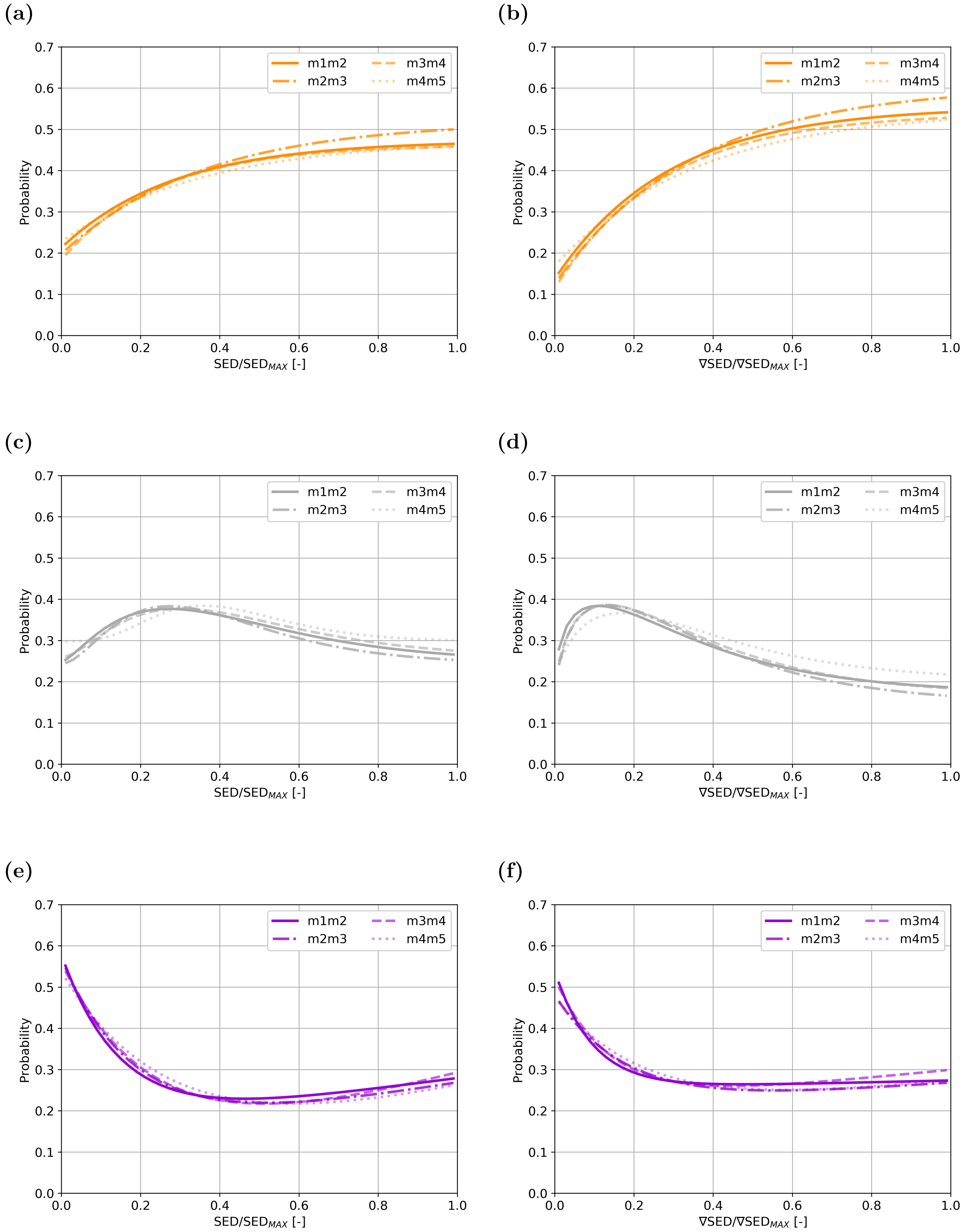

Supplementary Figure S7: Regression lines for conditional probability over time (5 Hz dynamic-loading group, cortical bone) for: **(a)** formation, SED **(b)** formation, SED gradient **(c)** quiescence, SED **(d)** quiescence, SED gradient **(e)** resorption, SED **(f)** resorption, SED gradient

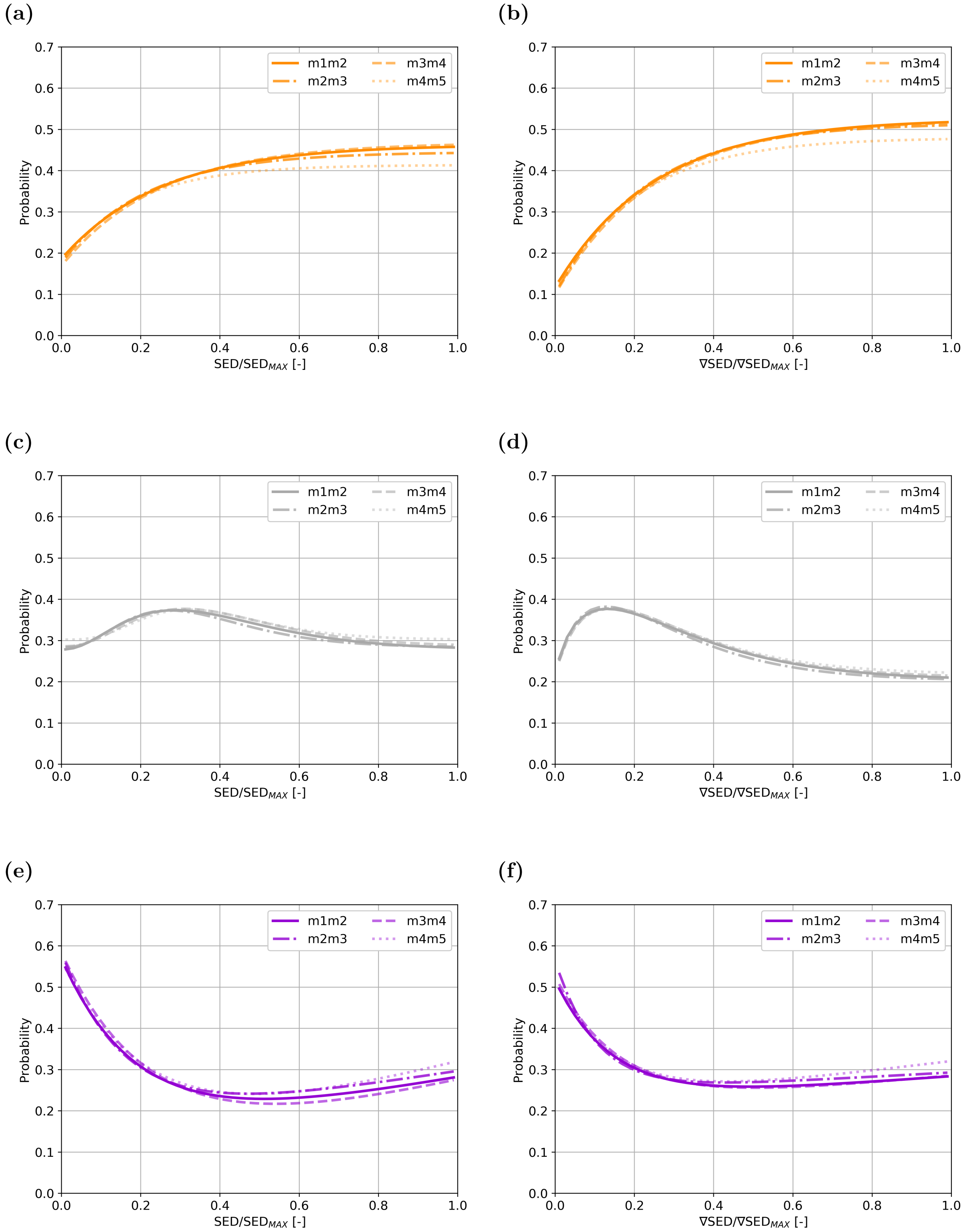

Supplementary Figure S8: Regression lines for conditional probability over time (2 Hz dynamic-loading group, cortical bone) for: **(a)** formation, SED **(b)** formation, SED gradient **(c)** quiescence, SED **(d)** quiescence, SED gradient **(e)** resorption, SED **(f)** resorption, SED gradient

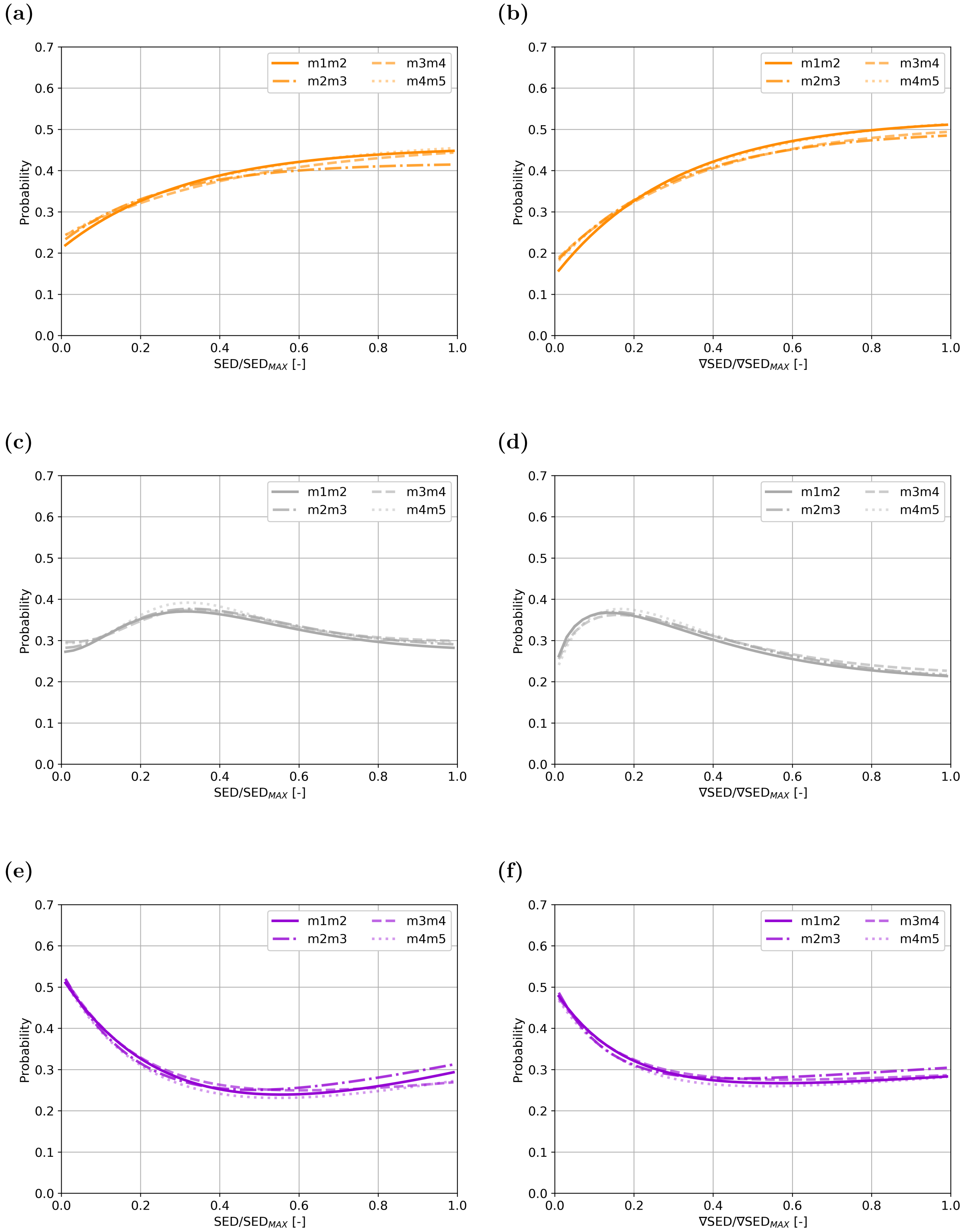

Supplementary Figure S9: Regression lines for conditional probability over time (static-loading group, cortical bone) for: **(a)** formation, SED **(b)** formation, SED gradient **(c)** quiescence, SED **(d)** quiescence, SED gradient **(e)** resorption, SED **(f)** resorption, SED gradient

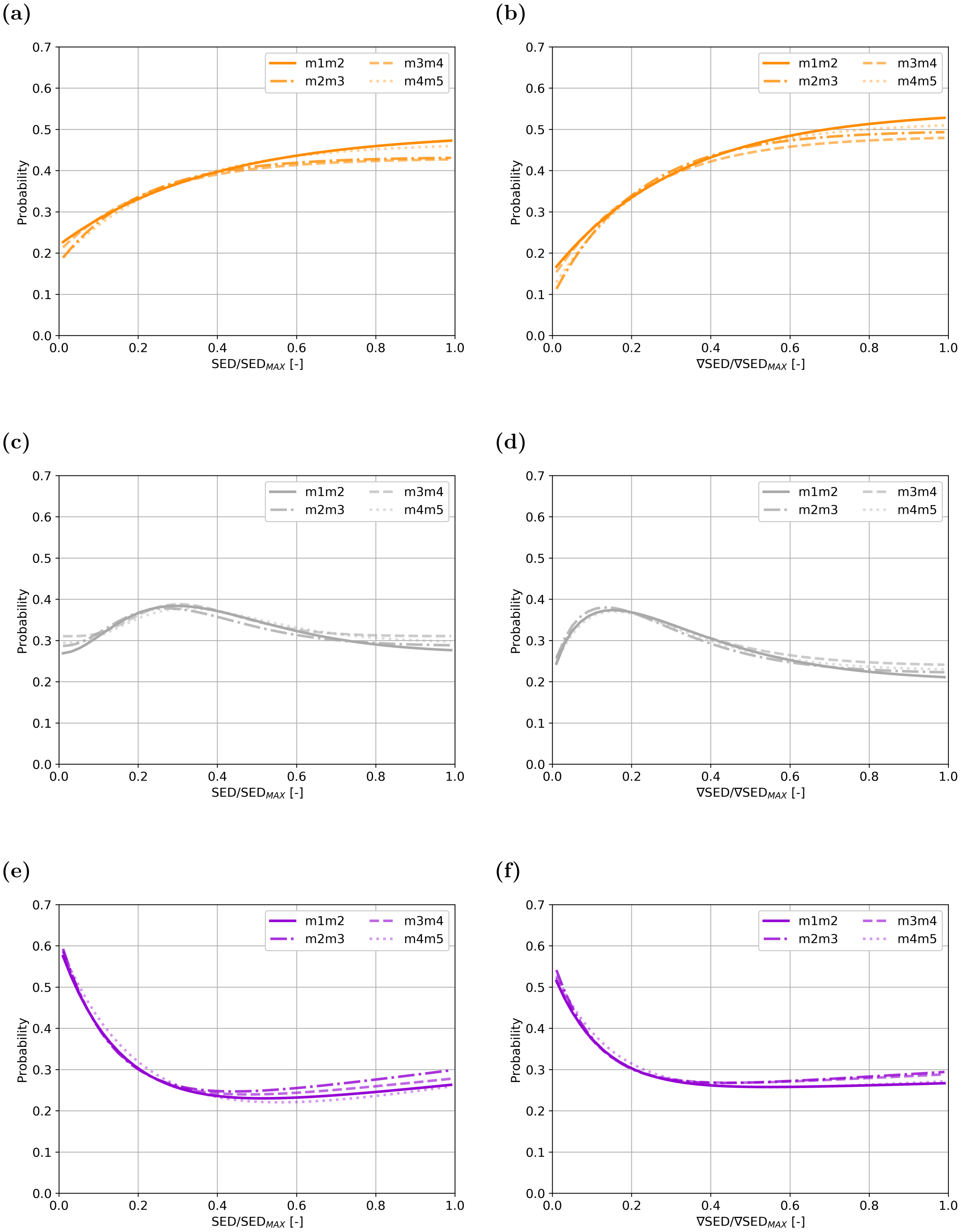

Supplementary Figure S10: Regression lines for conditional probability over time (sham-loading/control group, cortical bone) for: **(a)** formation, SED **(b)** formation, SED gradient **(c)** quiescence, SED **(d)** quiescence, SED gradient **(e)** resorption, SED **(f)** resorption, SED gradient

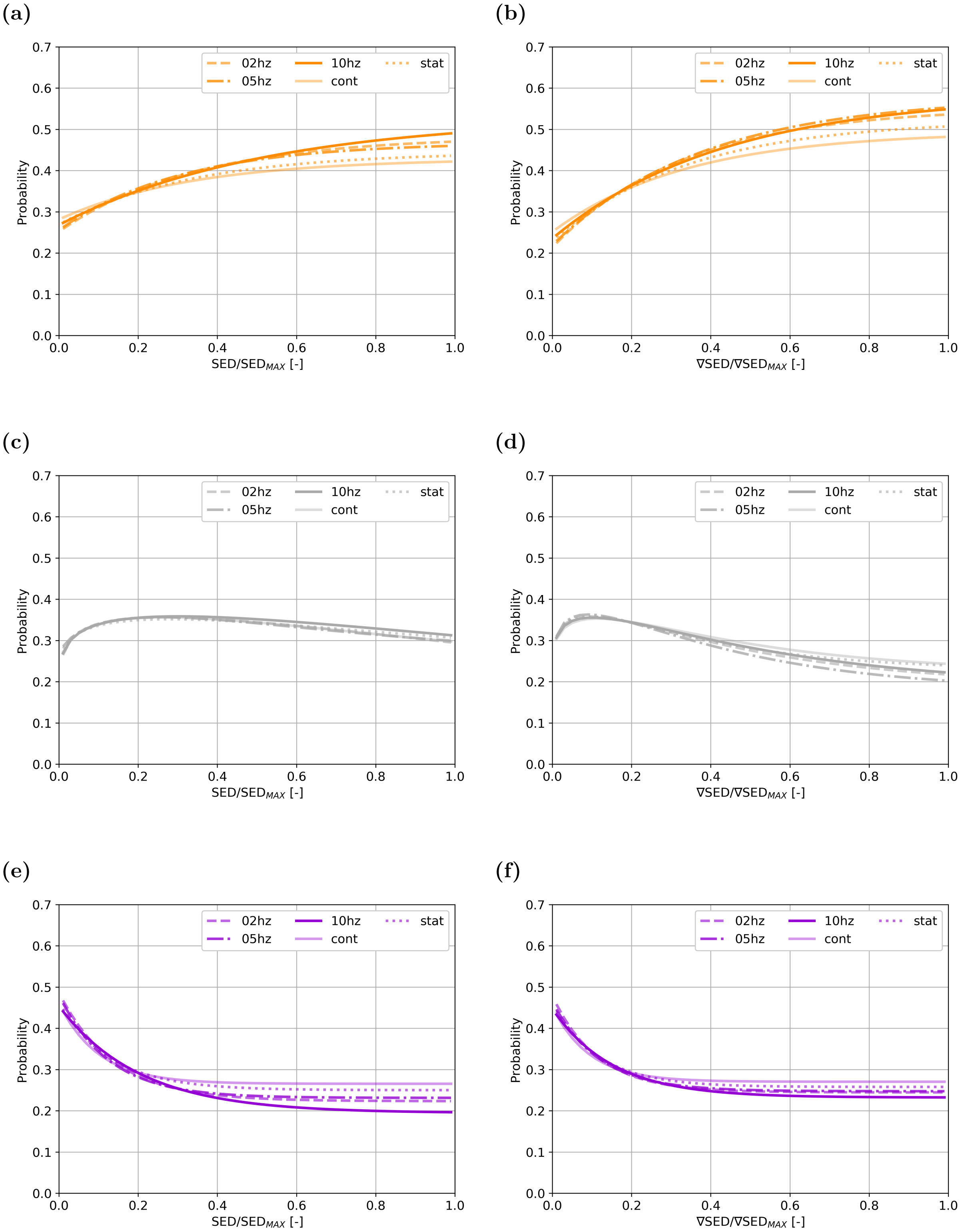

Supplementary Figure S11: Regression lines for conditional probability for all groups (Week m1m2, trabecular bone): **(a)** formation, SED **(b)** formation, SED gradient **(c)** quiescence, SED **(d)** quiescence, SED gradient **(e)** resorption, SED **(f)** resorption, SED gradient.

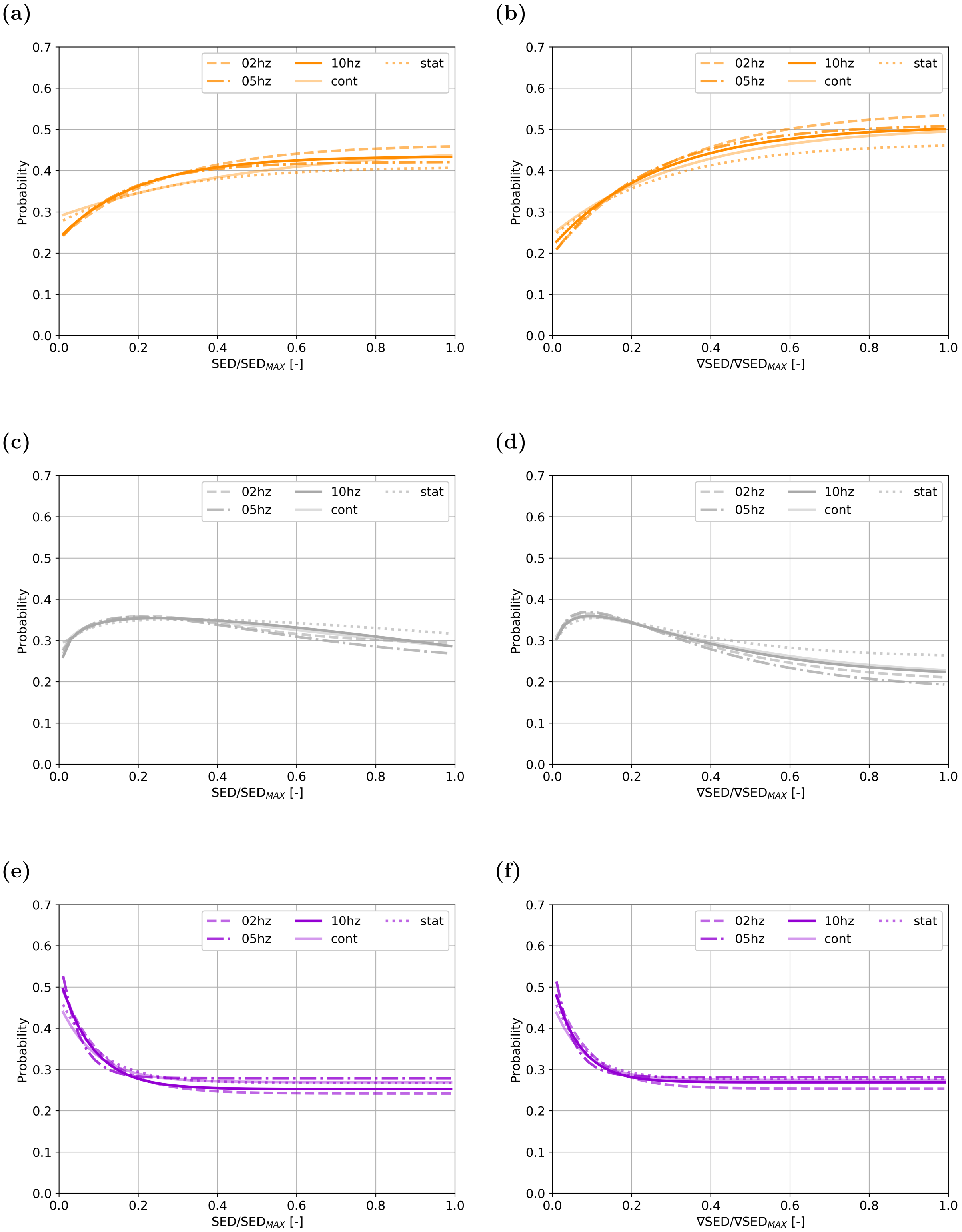

Supplementary Figure S12: Regression lines for conditional probability for all groups (Week m2m3, trabecular bone): **(a)** formation, SED **(b)** formation, SED gradient **(c)** quiescence, SED **(d)** quiescence, SED gradient **(e)** resorption, SED **(f)** resorption, SED gradient.

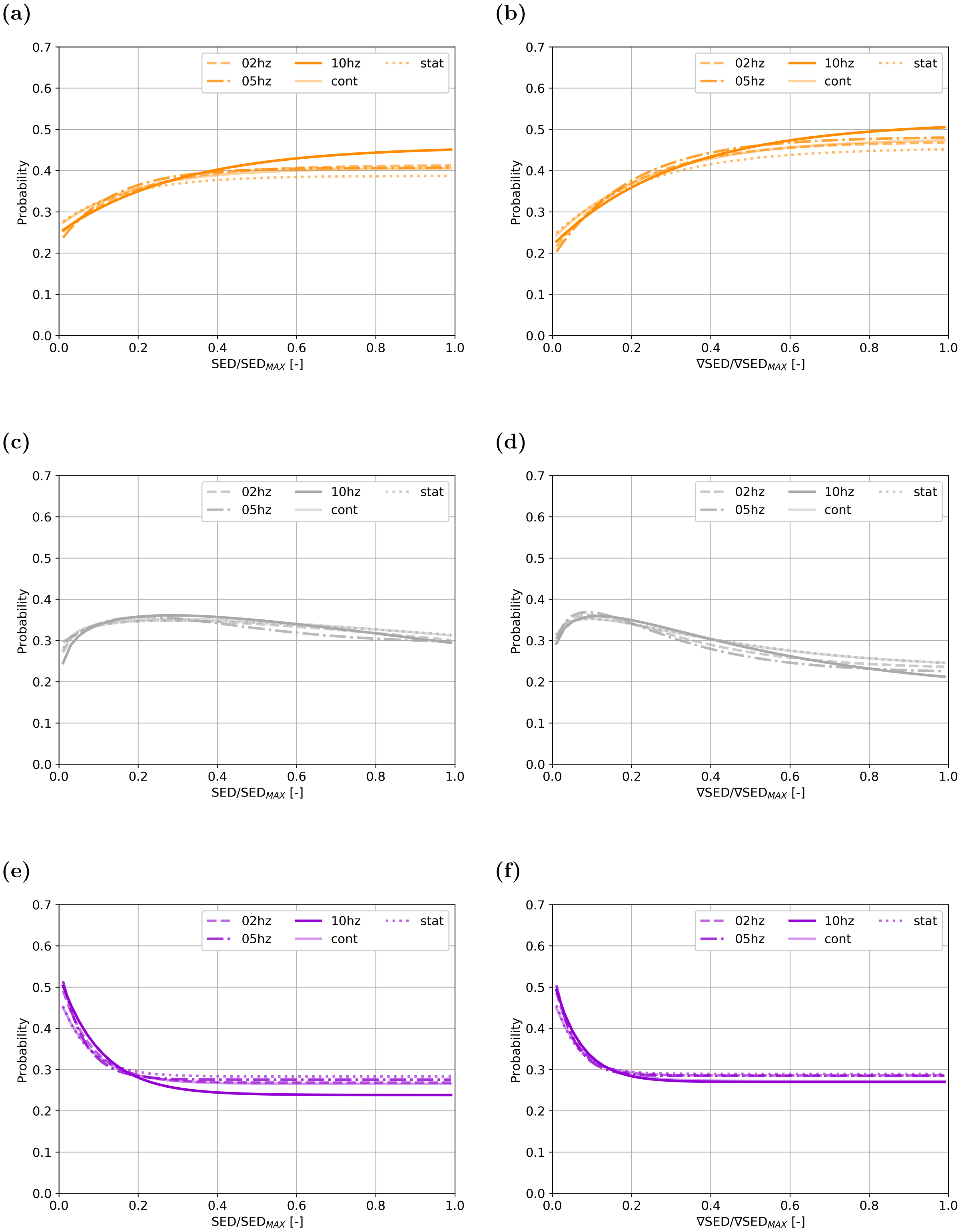

Supplementary Figure S13: Regression lines for conditional probability for all groups (Week m3m4, trabecular bone): **(a)** formation, SED **(b)** formation, SED gradient **(c)** quiescence, SED **(d)** quiescence, SED gradient **(e)** resorption, SED **(f)** resorption, SED gradient.

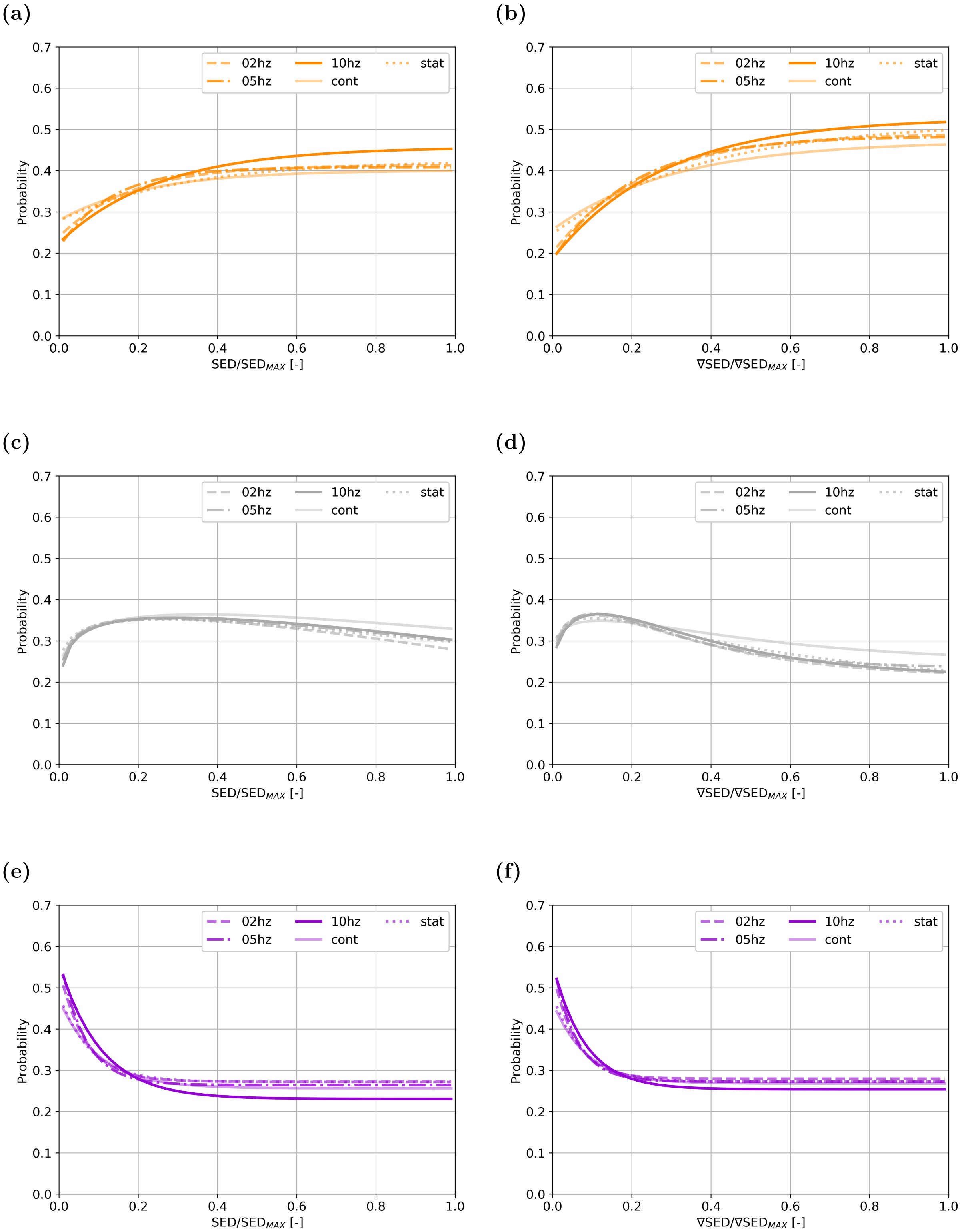

Supplementary Figure S14: Regression lines for conditional probability for all groups (Week m4m5, trabecular bone): **(a)** formation, SED **(b)** formation, SED gradient **(c)** quiescence, SED **(d)** quiescence, SED gradient **(e)** resorption, SED **(f)** resorption, SED gradient.

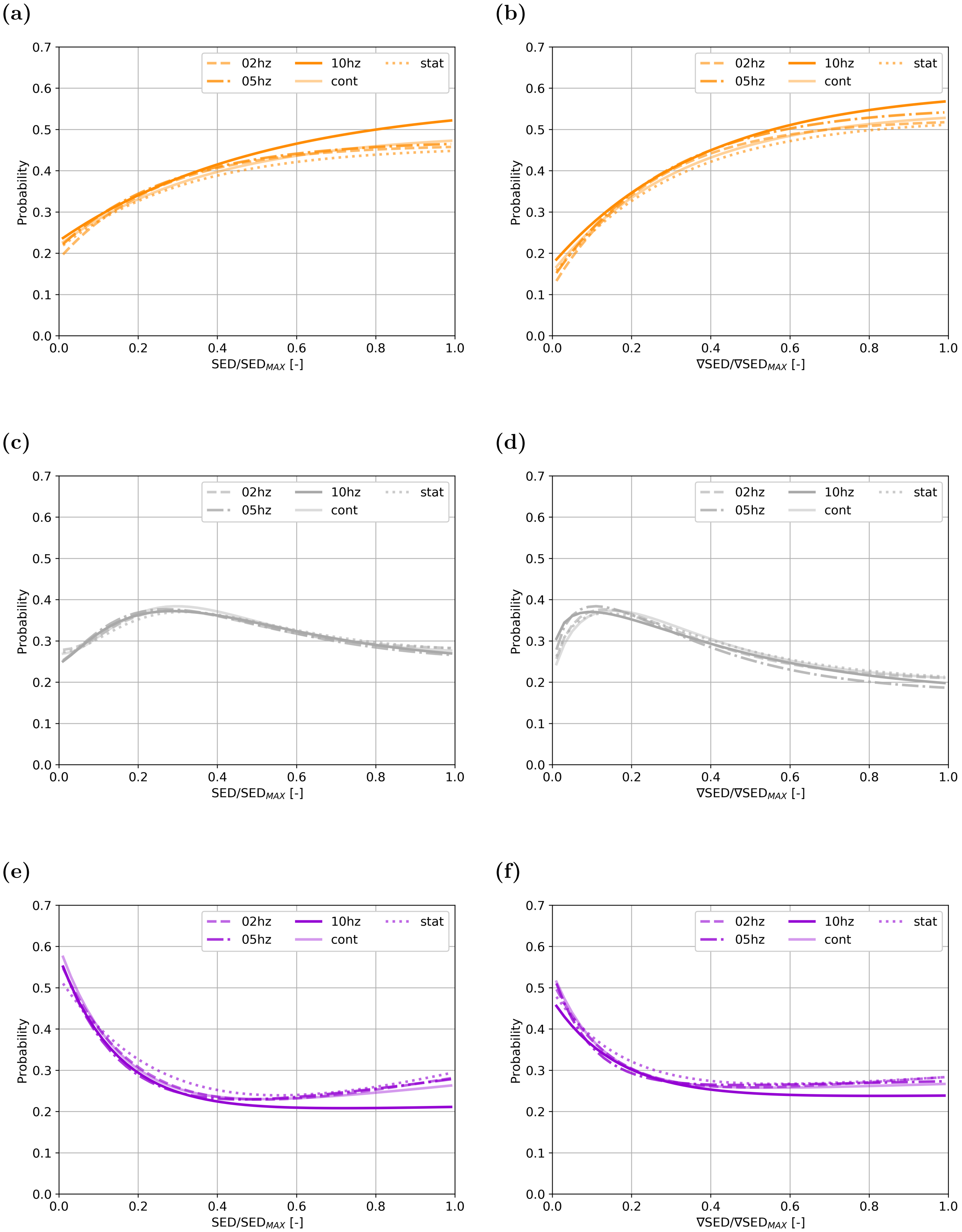

Supplementary Figure S15: Regression lines for conditional probability for all groups (Week m1m2, cortical bone): **(a)** formation, SED **(b)** formation, SED gradient **(c)** quiescence, SED **(d)** quiescence, SED gradient **(e)** resorption, SED **(f)** resorption, SED gradient.

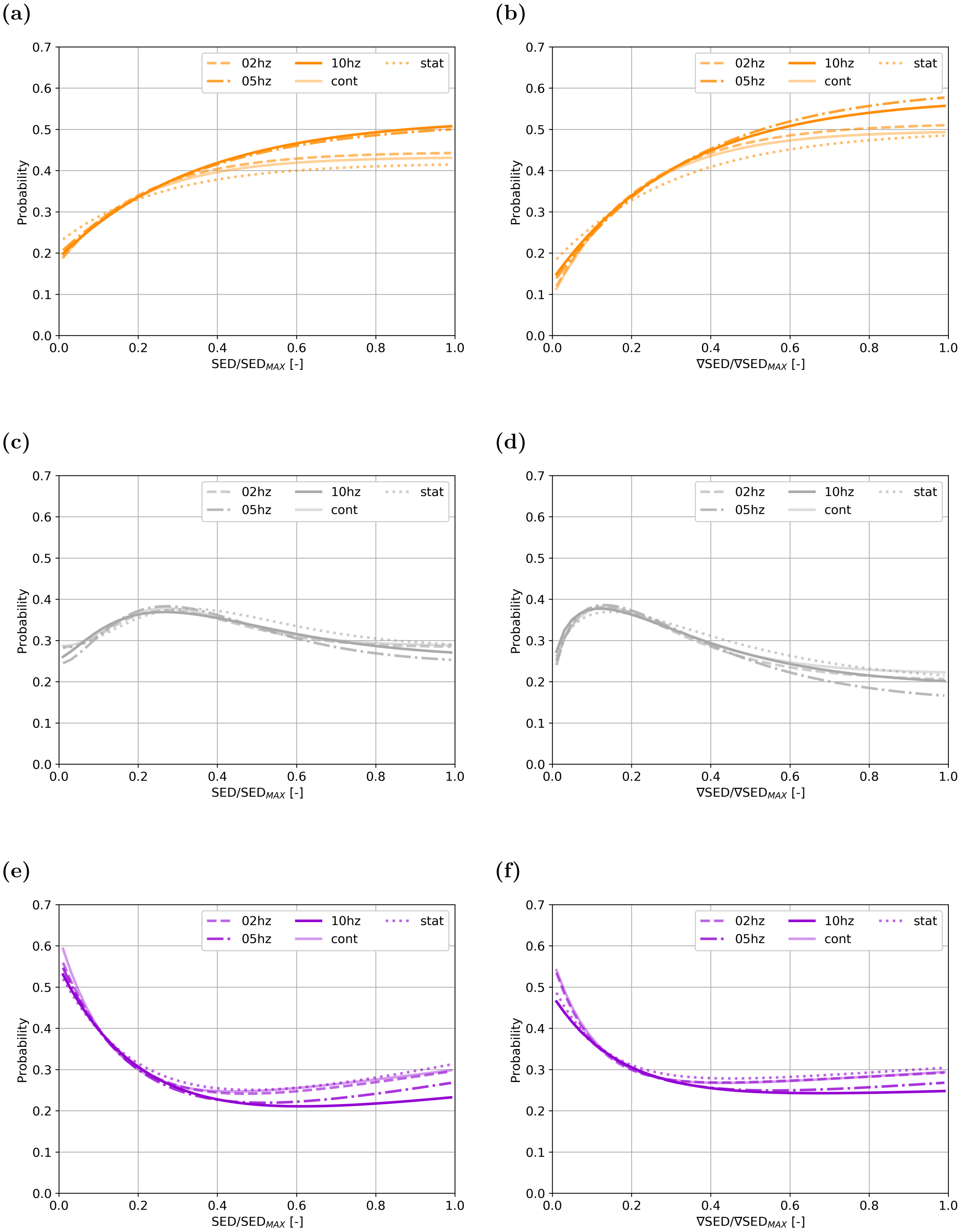

Supplementary Figure S16: Regression lines for conditional probability for all groups (Week m2m3, cortical bone): **(a)** formation, SED **(b)** formation, SED gradient **(c)** quiescence, SED **(d)** quiescence, SED gradient **(e)** resorption, SED **(f)** resorption, SED gradient.

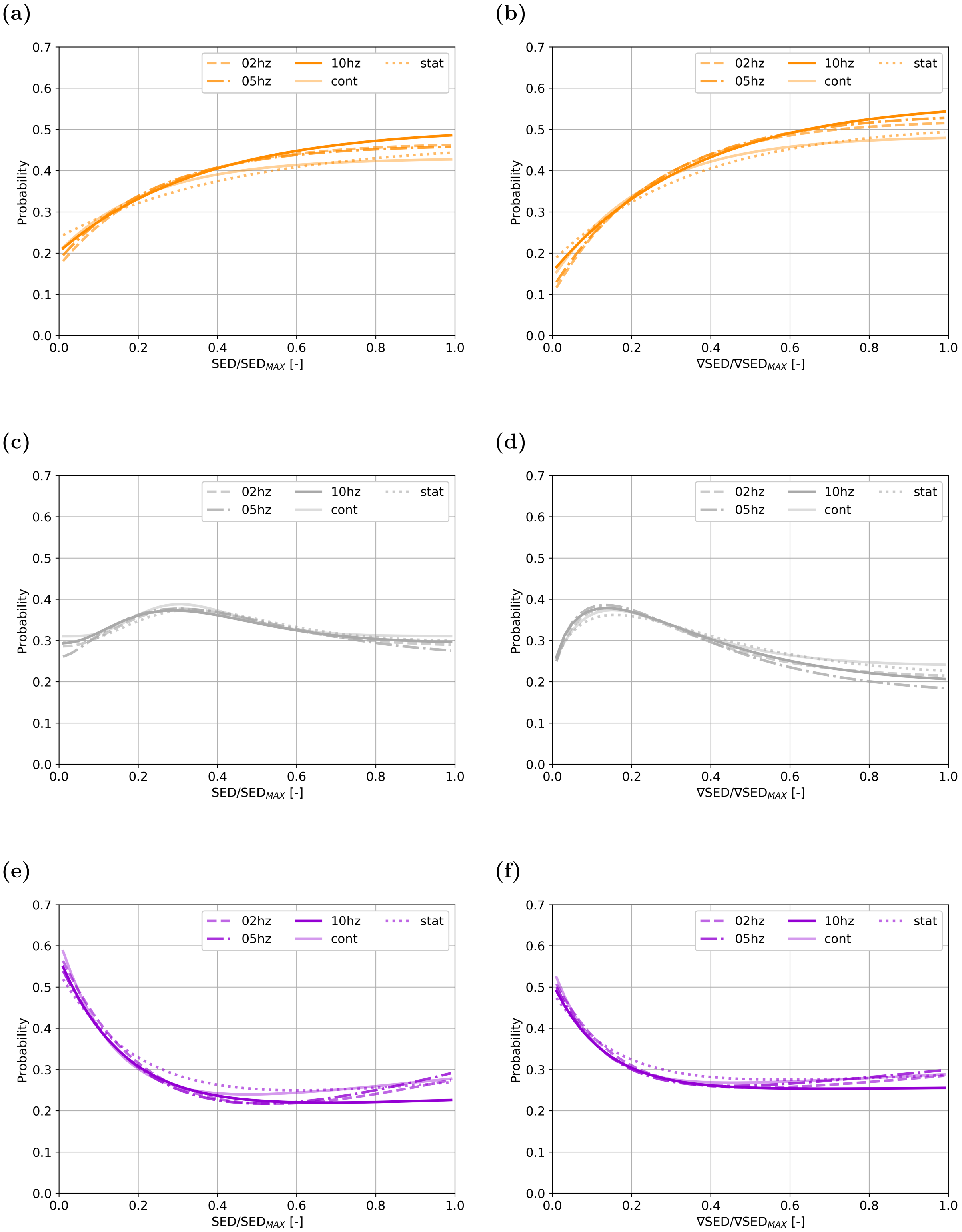

Supplementary Figure S17: Regression lines for conditional probability for all groups (Week m3m4, cortical bone): **(a)** formation, SED **(b)** formation, SED gradient **(c)** quiescence, SED **(d)** quiescence, SED gradient **(e)** resorption, SED **(f)** resorption, SED gradient.

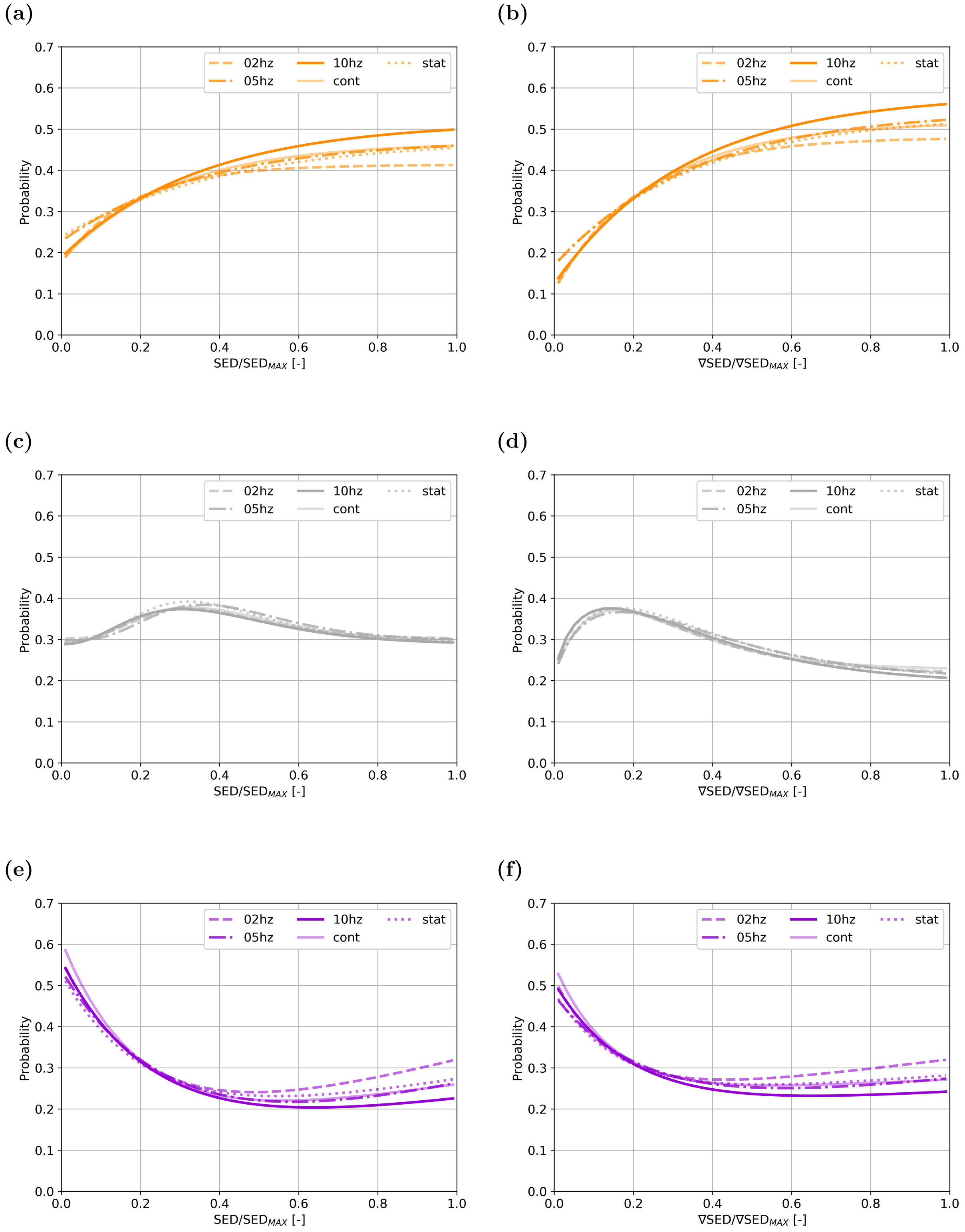

Supplementary Figure S18: Regression lines for conditional probability for all groups (Week m4m5, cortical bone): **(a)** formation, SED **(b)** formation, SED gradient **(c)** quiescence, SED **(d)** quiescence, SED gradient **(e)** resorption, SED **(f)** resorption, SED gradient.

Appendix B

Supplementary tables

Supplementary Table S1: Summary of non-linear regression functions and corresponding parameters for the conditional probability (SED) in trabecular bone.

Region	**Formation**					**Resorption**				
Regression line	$F = a*(1-\exp(-b*SED/SED_{MAX}))+y_0$					$R = a*\exp(-b*SED/SED_{MAX})+y_0$				
Week	**m1m2**	**m2m3**	**m3m4**	**m4m5**	**m1m5**	**m1m2**	**m2m3**	**m3m4**	**m4m5**	**m1m5**
Control group - CONT										
a	0.148	0.173	0.140	0.121	0.139	0.194	0.190	0.207	0.214	0.201
b	2.968	1.975	5.271	4.467	3.471	9.890	11.137	11.578	10.035	10.609
y_0	0.282	0.289	0.266	0.280	0.281	0.266	0.269	0.266	0.257	0.264
R^2	0.972	0.915	0.945	0.850	0.979	0.943	0.915	0.908	0.933	0.964
Static loading - STAT										
a	0.176	0.136	0.118	0.146	0.141	0.213	0.211	0.197	0.211	0.206
b	2.970	3.756	6.089	3.196	3.742	7.780	10.282	14.416	12.558	10.806
y_0	0.270	0.274	0.270	0.279	0.274	0.250	0.268	0.283	0.272	0.269
R^2	0.960	0.942	0.879	0.940	0.973	0.955	0.964	0.917	0.909	0.980
Dynamic loading - 02Hz										
a	0.231	0.228	0.171	0.174	0.197	0.263	0.275	0.254	0.272	0.262
b	2.900	3.828	5.445	5.606	4.160	7.272	9.877	13.113	15.091	10.853
y_0	0.252	0.236	0.243	0.240	0.244	0.224	0.242	0.268	0.273	0.253
R^2	0.981	0.971	0.968	0.965	0.992	0.968	0.964	0.947	0.915	0.982
Dynamic loading - 05Hz										
a	0.213	0.191	0.183	0.194	0.189	0.249	0.308	0.284	0.316	0.284
b	3.224	6.079	7.363	7.606	5.664	7.998	21.523	17.505	15.864	15.033
y_0	0.256	0.230	0.224	0.214	0.234	0.232	0.279	0.276	0.265	0.264
R^2	0.969	0.949	0.908	0.952	0.979	0.952	0.802	0.854	0.928	0.949
Dynamic loading - 10Hz										
a	0.262	0.198	0.210	0.232	0.217	0.259	0.273	0.291	0.329	0.284
b	1.908	5.063	3.278	3.964	3.381	4.907	12.011	9.665	9.552	8.764
y_0	0.268	0.237	0.249	0.225	0.247	0.195	0.253	0.239	0.231	0.232
R^2	0.978	0.974	0.962	0.974	0.988	0.966	0.916	0.956	0.980	0.981

Supplementary Table S2: Summary of non-linear regression functions and corresponding parameters for the conditional probability (SED gradient) in trabecular bone.

Region	**Formation**					**Resorption**				
Regression line	$F = a*(1-exp(-b*\nabla SED/\nabla SED_{MAX}))+y_0$					$R = a*exp(-b*\nabla SED/\nabla SED_{MAX})+y_0$				
Week	**m1m2**	**m2m3**	**m3m4**	**m4m5**	**m1m5**	**m1m2**	**m2m3**	**m3m4**	**m4m5**	**m1m5**
Control group - CONT										
a	0.243	0.262	0.244	0.215	0.240	0.181	0.186	0.202	0.197	0.191
b	2.943	3.011	4.043	3.257	3.287	10.718	13.158	13.476	11.951	12.289
y_0	0.252	0.246	0.234	0.257	0.248	0.271	0.275	0.272	0.268	0.272
R^2	0.982	0.974	0.967	0.963	0.993	0.952	0.933	0.942	0.923	0.975
Static loading - STAT										
a	0.293	0.227	0.215	0.271	0.249	0.200	0.205	0.200	0.210	0.202
b	2.920	3.577	4.244	2.644	3.244	8.605	13.045	18.362	13.585	12.919
y_0	0.230	0.241	0.240	0.247	0.240	0.258	0.277	0.290	0.273	0.275
R^2	0.990	0.972	0.941	0.965	0.990	0.970	0.945	0.933	0.943	0.981
Dynamic loading - 02Hz										
a	0.340	0.349	0.266	0.288	0.307	0.233	0.255	0.241	0.260	0.245
b	2.977	3.416	4.877	4.297	3.775	8.767	11.330	18.467	17.673	13.431
y_0	0.214	0.198	0.204	0.202	0.205	0.245	0.254	0.286	0.280	0.267
R^2	0.988	0.980	0.982	0.981	0.995	0.966	0.951	0.935	0.946	0.983
Dynamic loading - 05Hz										
a	0.360	0.317	0.293	0.298	0.311	0.216	0.292	0.271	0.294	0.264
b	2.618	4.131	5.081	4.964	4.045	8.544	22.965	21.170	17.577	16.915
y_0	0.220	0.196	0.189	0.186	0.200	0.248	0.282	0.285	0.273	0.273
R^2	0.979	0.974	0.958	0.973	0.993	0.935	0.841	0.865	0.948	0.964
Dynamic loading - 10Hz										
a	0.348	0.291	0.299	0.341	0.316	0.215	0.244	0.258	0.303	0.252
b	2.299	3.730	3.165	3.570	3.147	6.599	14.889	14.559	12.390	11.770
y_0	0.236	0.217	0.219	0.187	0.216	0.232	0.269	0.270	0.254	0.258
R^2	0.983	0.975	0.990	0.986	0.996	0.960	0.942	0.965	0.981	0.984

Supplementary Table S3: Summary of non-linear regression functions and corresponding parameters for the conditional probability (SED) in cortical bone.

Region	**Formation**					**Resorption**				
Regression line	$F = a*(1-exp(-b*SED/SED_{MAX}))+y_0$					$R = a*exp(-b*SED/SED_{MAX}) +c*(SED/SED_{MAX}+d)+y_0$				
Week	**m1m2**	**m2m3**	**m3m4**	**m4m5**	**m1m5**	**m1m2**	**m2m3**	**m3m4**	**m4m5**	**m1m5**
Control group - CONT										
a	0.273	0.257	0.226	0.288	0.256	0.438	0.450	0.447	0.439	0.501
b	2.619	4.859	4.366	3.642	3.782	6.489	6.539	7.539	7.214	5.096
c	-	-	-	-	-	0.100	0.113	0.122	0.101	0.149
d	-	-	-	-	-	0.145	0.144	0.156	0.164	0.134
y_0	0.220	0.177	0.204	0.180	0.197	0.149	0.146	0.158	0.161	0.088
R^2	0.920	0.756	0.818	0.810	0.846	-	-	-	-	-
Static loading - STAT										
a	0.248	0.193	0.230	0.238	0.223	0.505	0.419	0.422	0.360	0.422
b	3.130	3.906	2.223	2.411	2.845	3.415	4.410	4.855	4.900	4.482
c	-	-	-	-	-	0.259	0.170	0.194	0.091	0.163
d	-	-	-	-	-	0.017	0.105	0.098	0.161	0.123
y_0	0.212	0.226	0.239	0.238	0.230	0.015	0.095	0.097	0.161	0.086
R^2	0.835	0.799	0.860	0.898	0.866	-	-	-	-	-
Dynamic loading - 02Hz										
a	0.277	0.268	0.299	0.237	0.269	0.462	0.480	0.437	0.544	0.504
b	3.962	4.690	3.968	5.569	4.478	5.113	4.981	6.143	4.311	4.493
c	-	-	-	-	-	0.173	0.196	0.149	0.229	0.254
d	-	-	-	-	-	0.115	0.103	0.136	0.051	0.057
y_0	0.187	0.177	0.169	0.177	0.178	0.087	0.075	0.127	0.029	0.047
R^2	0.899	0.896	0.883	0.756	0.877	-	-	-	-	-
Dynamic loading - 05Hz										
a	0.260	0.322	0.279	0.248	0.274	0.428	0.477	0.463	0.546	0.525
b	3.518	2.815	4.049	2.796	3.254	6.713	4.607	5.260	4.140	3.512
c	-	-	-	-	-	0.128	0.198	0.161	0.272	0.236
d	-	-	-	-	-	0.134	0.068	0.091	0.010	0.010
y_0	0.213	0.198	0.184	0.228	0.207	0.134	0.062	0.091	0.010	0.010
R^2	0.949	0.958	0.929	0.946	0.959	-	-	-	-	-
Dynamic loading - 10Hz										
a	0.341	0.339	0.302	0.330	0.325	0.385	0.406	0.425	0.382	0.467
b	1.958	2.828	2.770	2.861	2.618	6.789	5.448	4.843	6.165	4.330
c	-	-	-	-	-	0.020	0.066	0.106	0.036	0.128
d	-	-	-	-	-	0.143	0.163	0.111	0.170	0.096
y_0	0.230	0.189	0.204	0.189	0.203	0.188	0.146	0.112	0.183	0.081
R^2	0.979	0.954	0.966	0.964	0.975	-	-	-	-	

Supplementary Table S4: Summary of non-linear regression functions and corresponding parameters for the conditional probability (SED gradient) in cortical bone.

Region	**Formation**					**Resorption**				
Regression line	$F = a*(1-\exp(-b*\nabla SED/\nabla SED_{MAX}))+y_0$					$R = a*\exp(-b*\nabla SED/\nabla SED_{MAX})$ $+c*(\nabla SED/\nabla SED_{MAX}+d)+y_0$				
Week	**m1m2**	**m2m3**	**m3m4**	**m4m5**	**m1m5**	**m1m2**	**m2m3**	**m3m4**	**m4m5**	**m1m5**
Control group - CONT										
a	0.392	0.403	0.345	0.405	0.383	0.299	0.334	0.308	0.325	0.314
b	3.063	4.688	4.283	3.903	3.943	8.160	9.087	8.911	6.988	8.227
c	-	-	-	-	-	0.028	0.059	0.048	0.047	0.045
d	-	-	-	-	-	0.251	0.224	0.230	0.213	0.253
y_0	0.155	0.095	0.140	0.114	0.128	0.232	0.222	0.230	0.215	0.225
R^2	0.918	0.793	0.843	0.840	0.860	-	-	-	-	-
Static loading - STAT										
a	0.381	0.323	0.334	0.363	0.350	0.271	0.263	0.243	0.274	0.261
b	3.221	3.216	2.803	2.864	3.021	5.647	7.709	6.123	5.861	6.346
c	-	-	-	-	-	0.062	0.063	0.042	0.072	0.057
d	-	-	-	-	-	0.228	0.228	0.234	0.206	0.207
y_0	0.146	0.175	0.180	0.172	0.169	0.207	0.228	0.234	0.194	0.220
R^2	0.883	0.879	0.881	0.913	0.896	-	-	-	-	-
Dynamic loading - 02Hz										
a	0.409	0.414	0.423	0.372	0.404	0.301	0.323	0.328	0.314	0.312
b	3.967	4.361	4.037	4.749	4.259	6.907	9.557	6.251	6.649	7.334
c	-	-	-	-	-	0.069	0.052	0.087	0.118	0.077
d	-	-	-	-	-	0.212	0.220	0.179	0.172	0.185
y_0	0.117	0.102	0.100	0.108	0.107	0.200	0.230	0.182	0.183	0.204
R^2	0.914	0.915	0.893	0.842	0.899	-	-	-	-	-
Dynamic loading - 05Hz										
a	0.417	0.480	0.425	0.376	0.422	0.286	0.282	0.315	0.311	0.282
b	3.439	2.869	3.637	2.840	3.170	10.304	5.639	7.095	4.404	6.637
c	-	-	-	-	-	0.022	0.069	0.094	0.106	0.062
d	-	-	-	-	-	0.209	0.186	0.174	0.179	0.209
y_0	0.138	0.126	0.115	0.169	0.138	0.248	0.186	0.189	0.147	0.203
R^2	0.942	0.952	0.928	0.956	0.954	-	-	-	-	-
Dynamic loading - 10Hz										
a	0.426	0.443	0.415	0.460	0.435	0.242	0.263	0.264	0.322	0.268
b	2.599	3.082	2.769	2.991	2.872	6.114	5.800	7.729	5.190	6.804
c	-	-	-	-	-	0.010	0.030	0.010	0.056	0.010
d	-	-	-	-	-	0.205	0.211	0.140	0.175	0.192
y_0	0.174	0.136	0.155	0.125	0.147	0.226	0.211	0.244	0.175	0.232
R^2	0.973	0.955	0.964	0.964	0.968	-	-	-	-	-

Appendix C

Supplementary data

Supplementary Data S1: Data - bone morphometric parameters in trabecular bone

Group	Mouse	Measurement	BV [mm^3]	TV [mm^3]	BV/TV [-]
cont	02	m1	0.316	1.705	0.185
cont	03	m1	0.274	1.612	0.170
cont	04	m1	0.238	1.284	0.185
cont	05	m1	0.305	1.513	0.202
cont	06	m1	0.206	1.585	0.130
cont	07	m1	0.249	1.509	0.165
cont	08	m1	0.281	1.783	0.158
cont	09	m1	0.263	1.614	0.163
stat	01	m1	0.322	1.599	0.202
stat	02	m1	0.278	1.530	0.182
stat	03	m1	0.284	1.517	0.187
stat	04	m1	0.276	1.569	0.176
stat	05	m1	0.322	1.728	0.186
stat	06	m1	0.257	1.558	0.165
stat	07	m1	0.249	1.549	0.161
stat	08	m1	0.270	1.665	0.162
02Hz	01	m1	0.236	1.496	0.158
02Hz	06	m1	0.377	1.605	0.235
02Hz	09	m1	0.264	1.474	0.179
02Hz	10	m1	0.288	1.427	0.202
02Hz	11	m1	0.240	1.388	0.173
02Hz	12	m1	0.226	1.503	0.151

Continued on next page

Supplementary Data S1: Data - bone morphometric parameters in trabecular bone (continued)

Group	Mouse	Measurement	BV [mm^3]	TV [mm^3]	BV/TV [-]
02Hz	13	m1	0.301	1.790	0.168
05Hz	01	m1	0.283	1.795	0.158
05Hz	02	m1	0.306	1.688	0.181
05Hz	08	m1	0.311	1.563	0.199
05Hz	09	m1	0.320	1.680	0.191
05Hz	10	m1	0.343	1.643	0.208
10Hz	01	m1	0.277	1.738	0.159
10Hz	02	m1	0.263	1.440	0.183
10Hz	04	m1	0.307	1.483	0.207
10Hz	05	m1	0.236	1.421	0.166
10Hz	06	m1	0.259	1.477	0.175
10Hz	07	m1	0.248	1.657	0.150
10Hz	08	m1	0.279	1.775	0.157
10Hz	09	m1	0.250	1.535	0.163
cont	02	m2	0.307	1.746	0.176
cont	03	m2	0.259	1.618	0.160
cont	04	m2	0.244	1.305	0.187
cont	05	m2	0.303	1.560	0.194
cont	06	m2	0.229	1.678	0.137
cont	07	m2	0.244	1.549	0.157
cont	08	m2	0.276	1.821	0.151
cont	09	m2	0.271	1.596	0.170
stat	01	m2	0.319	1.634	0.195
stat	02	m2	0.269	1.500	0.179
stat	03	m2	0.298	1.537	0.194
stat	04	m2	0.265	1.590	0.167
stat	05	m2	0.331	1.786	0.185
stat	06	m2	0.250	1.536	0.163
stat	07	m2	0.262	1.554	0.169
stat	08	m2	0.271	1.651	0.164
02Hz	01	m2	0.251	1.519	0.165
02Hz	06	m2	0.401	1.621	0.247

Continued on next page

Supplementary Data S1: Data - bone morphometric parameters in trabecular bone (continued)

Group	Mouse	Measurement	BV [mm^3]	TV [mm^3]	BV/TV [-]
02Hz	09	m2	0.271	1.444	0.187
02Hz	10	m2	0.303	1.404	0.216
02Hz	11	m2	0.236	1.322	0.178
02Hz	12	m2	0.223	1.480	0.151
02Hz	13	m2	0.278	1.783	0.156
05Hz	01	m2	0.302	1.766	0.171
05Hz	02	m2	0.308	1.650	0.187
05Hz	08	m2	0.322	1.552	0.208
05Hz	09	m2	0.337	1.630	0.207
05Hz	10	m2	0.343	1.653	0.207
10Hz	01	m2	0.276	1.731	0.159
10Hz	02	m2	0.278	1.444	0.192
10Hz	04	m2	0.317	1.480	0.214
10Hz	05	m2	0.238	1.425	0.167
10Hz	06	m2	0.270	1.431	0.189
10Hz	07	m2	0.283	1.603	0.177
10Hz	08	m2	0.279	1.665	0.167
10Hz	09	m2	0.251	1.461	0.172
cont	02	m3	0.302	1.724	0.175
cont	03	m3	0.261	1.616	0.161
cont	04	m3	0.257	1.327	0.194
cont	05	m3	0.301	1.587	0.190
cont	06	m3	0.229	1.741	0.132
cont	07	m3	0.244	1.596	0.153
cont	08	m3	0.280	1.831	0.153
cont	09	m3	0.283	1.625	0.174
stat	01	m3	0.307	1.669	0.184
stat	02	m3	0.275	1.491	0.185
stat	03	m3	0.307	1.560	0.197
stat	04	m3	0.260	1.675	0.155
stat	05	m3	0.337	1.817	0.186
stat	06	m3	0.256	1.582	0.162

Continued on next page

Supplementary Data S1: Data - bone morphometric parameters in trabecular bone (continued)

Group	Mouse	Measurement	BV [mm^3]	TV [mm^3]	BV/TV [-]
stat	07	m3	0.258	1.515	0.171
stat	08	m3	0.262	1.635	0.161
02Hz	01	m3	0.253	1.517	0.167
02Hz	06	m3	0.410	1.600	0.256
02Hz	09	m3	0.298	1.450	0.206
02Hz	10	m3	0.306	1.389	0.220
02Hz	11	m3	0.246	1.328	0.186
02Hz	12	m3	0.254	1.529	0.166
02Hz	13	m3	0.297	1.756	0.169
05Hz	01	m3	0.331	1.713	0.193
05Hz	02	m3	0.311	1.603	0.194
05Hz	08	m3	0.320	1.503	0.213
05Hz	09	m3	0.364	1.588	0.229
05Hz	10	m3	0.348	1.660	0.210
10Hz	01	m3	0.295	1.723	0.171
10Hz	02	m3	0.299	1.444	0.207
10Hz	04	m3	0.343	1.464	0.234
10Hz	05	m3	0.261	1.431	0.182
10Hz	06	m3	0.309	1.448	0.213
10Hz	07	m3	0.325	1.561	0.209
10Hz	08	m3	0.305	1.661	0.184
10Hz	09	m3	0.269	1.435	0.187
cont	02	m4	0.301	1.714	0.176
cont	03	m4	0.272	1.621	0.168
cont	04	m4	0.260	1.341	0.194
cont	05	m4	0.296	1.600	0.185
cont	06	m4	0.215	1.725	0.125
cont	07	m4	0.245	1.596	0.154
cont	08	m4	0.277	1.857	0.149
cont	09	m4	0.269	1.623	0.166
stat	01	m4	0.292	1.672	0.175
stat	02	m4	0.284	1.486	0.191

Continued on next page

Supplementary Data S1: Data - bone morphometric parameters in trabecular bone (continued)

Group	Mouse	Measurement	BV [mm^3]	TV [mm^3]	BV/TV [-]
stat	03	m4	0.310	1.570	0.198
stat	04	m4	0.257	1.728	0.148
stat	05	m4	0.327	1.846	0.177
stat	06	m4	0.250	1.597	0.157
stat	07	m4	0.263	1.536	0.171
stat	08	m4	0.268	1.638	0.164
02Hz	01	m4	0.257	1.504	0.171
02Hz	06	m4	0.437	1.601	0.273
02Hz	09	m4	0.310	1.439	0.215
02Hz	10	m4	0.301	1.383	0.218
02Hz	11	m4	0.261	1.325	0.197
02Hz	12	m4	0.261	1.534	0.170
02Hz	13	m4	0.307	1.690	0.181
05Hz	01	m4	0.354	1.685	0.210
05Hz	02	m4	0.320	1.582	0.202
05Hz	08	m4	0.332	1.499	0.221
05Hz	09	m4	0.390	1.558	0.250
05Hz	10	m4	0.365	1.660	0.220
10Hz	01	m4	0.311	1.680	0.185
10Hz	02	m4	0.305	1.415	0.215
10Hz	04	m4	0.380	1.481	0.257
10Hz	05	m4	0.273	1.396	0.196
10Hz	06	m4	0.329	1.431	0.230
10Hz	07	m4	0.365	1.571	0.233
10Hz	08	m4	0.328	1.658	0.198
10Hz	09	m4	0.298	1.441	0.207
cont	02	m5	0.310	1.713	0.181
cont	03	m5	0.293	1.628	0.180
cont	04	m5	0.260	1.329	0.195
cont	05	m5	0.288	1.576	0.183
cont	06	m5	0.209	1.791	0.117
cont	07	m5	0.244	1.583	0.154

Continued on next page

Supplementary Data S1: Data - bone morphometric parameters in trabecular bone (continued)

Group	Mouse	Measurement	BV [mm^3]	TV [mm^3]	BV/TV [-]
cont	08	m5	0.268	1.858	0.144
cont	09	m5	0.263	1.622	0.162
stat	01	m5	0.292	1.684	0.174
stat	02	m5	0.285	1.481	0.193
stat	03	m5	0.290	1.585	0.183
stat	04	m5	0.237	1.730	0.137
stat	05	m5	0.314	1.844	0.170
stat	06	m5	0.242	1.619	0.150
stat	07	m5	0.253	1.540	0.164
stat	08	m5	0.267	1.660	0.161
02Hz	01	m5	0.263	1.498	0.176
02Hz	06	m5	0.438	1.566	0.280
02Hz	09	m5	0.331	1.473	0.225
02Hz	10	m5	0.299	1.377	0.217
02Hz	11	m5	0.263	1.301	0.202
02Hz	12	m5	0.266	1.535	0.173
02Hz	13	m5	0.340	1.683	0.202
05Hz	01	m5	0.371	1.684	0.220
05Hz	02	m5	0.324	1.549	0.209
05Hz	08	m5	0.326	1.490	0.219
05Hz	09	m5	0.405	1.528	0.265
05Hz	10	m5	0.372	1.653	0.225
10Hz	01	m5	0.319	1.728	0.185
10Hz	02	m5	0.319	1.411	0.226
10Hz	04	m5	0.389	1.446	0.269
10Hz	05	m5	0.291	1.390	0.209
10Hz	06	m5	0.326	1.392	0.234
10Hz	07	m5	0.377	1.631	0.231
10Hz	08	m5	0.330	1.636	0.201
10Hz	09	m5	0.294	1.415	0.208

Supplementary Data S2: Data - bone dynamic, morphometric parameters in trabecular bone

Group	Mouse	Week	BFR [%/day]	BRR [%/day]	MAR [μm/day]	MRR [μm/day]	MS [%]	ES [%]
cont	02	m1m2	1.356	2.512	2.317	3.438	35.267	37.735
cont	03	m1m2	1.857	2.759	2.735	3.180	36.114	38.225
cont	04	m1m2	1.170	1.449	1.845	2.577	41.268	28.856
cont	05	m1m2	0.909	1.730	1.851	2.711	35.382	35.799
cont	06	m1m2	2.178	2.335	2.109	3.171	42.254	28.227
cont	07	m1m2	1.239	2.119	2.041	2.876	36.242	35.980
cont	08	m1m2	1.811	2.857	2.424	3.450	36.769	34.822
cont	09	m1m2	1.637	1.409	1.998	2.803	46.299	26.244
stat	01	m1m2	0.781	1.448	1.771	2.486	33.346	35.951
stat	02	m1m2	1.252	1.486	1.772	2.771	44.771	27.603
stat	03	m1m2	1.380	1.408	1.913	2.653	45.213	31.492
stat	04	m1m2	1.475	2.074	2.206	2.748	37.120	41.506
stat	05	m1m2	0.961	1.538	1.831	2.610	38.228	32.528
stat	06	m1m2	1.227	1.569	1.814	2.967	43.615	28.565
stat	07	m1m2	1.954	1.660	1.995	3.082	49.556	24.529
stat	08	m1m2	1.810	1.700	2.174	2.956	46.172	27.507
02Hz	01	m1m2	0.732	0.572	1.629	1.801	35.029	25.251
02Hz	06	m1m2	1.490	1.205	1.947	2.808	49.065	26.521
02Hz	09	m1m2	1.444	0.995	1.882	3.102	53.139	20.282
02Hz	10	m1m2	1.591	1.077	1.863	3.194	53.294	21.266
02Hz	11	m1m2	1.654	1.400	2.095	3.154	47.306	26.514
02Hz	12	m1m2	1.676	1.581	1.961	2.951	47.136	25.275
02Hz	13	m1m2	2.084	2.929	2.404	3.851	40.694	31.502
05Hz	01	m1m2	1.587	0.990	1.882	2.493	49.546	20.945
05Hz	02	m1m2	1.173	0.854	1.891	2.469	45.543	24.657
05Hz	08	m1m2	1.209	0.902	1.761	3.162	52.873	20.139
05Hz	09	m1m2	1.941	0.996	2.051	3.237	56.355	17.042
05Hz	10	m1m2	0.835	1.081	1.747	2.763	38.909	27.911
10Hz	01	m1m2	1.203	1.490	1.853	2.679	41.149	29.423
10Hz	02	m1m2	1.163	0.814	1.791	2.441	47.895	25.103
10Hz	04	m1m2	1.277	0.965	1.925	2.524	47.513	26.642

Continued on next page

Supplementary Data S2: Data - bone dynamic, morphometric parameters in trabecular bone (continued)

Group	Mouse	Week	BFR [%/day]	BRR [%/day]	MAR [μm/day]	MRR [μm/day]	MS [%]	ES [%]
10Hz	05	m1m2	2.051	2.345	2.874	3.146	38.587	35.291
10Hz	06	m1m2	2.831	5.862	6.697	4.314	19.888	69.700
10Hz	07	m1m2	3.160	0.849	2.250	3.468	63.594	12.824
10Hz	08	m1m2	1.784	0.663	2.105	2.316	51.858	21.157
10Hz	09	m1m2	2.050	1.024	2.300	2.323	47.556	25.246
cont	02	m2m3	1.035	1.352	1.777	2.803	43.224	27.198
cont	03	m2m3	1.269	1.336	1.845	2.647	44.427	27.339
cont	04	m2m3	1.570	1.543	2.053	2.772	44.595	30.691
cont	05	m2m3	0.972	1.568	1.815	2.805	38.684	31.263
cont	06	m2m3	1.715	2.736	1.982	3.623	41.730	27.442
cont	07	m2m3	1.448	2.259	1.934	3.056	40.000	32.467
cont	08	m2m3	1.813	1.925	2.450	2.911	40.171	32.544
cont	09	m2m3	1.566	1.614	2.038	2.829	43.256	31.672
stat	01	m2m3	0.929	2.100	1.722	3.273	38.615	30.948
stat	02	m2m3	1.967	1.841	2.361	2.731	42.110	33.670
stat	03	m2m3	1.618	1.367	2.108	2.646	44.938	32.135
stat	04	m2m3	1.433	2.960	2.397	3.443	33.435	38.923
stat	05	m2m3	1.422	1.808	2.097	2.914	41.327	31.692
stat	06	m2m3	1.446	2.110	1.983	3.306	42.925	31.653
stat	07	m2m3	1.746	1.718	2.192	2.990	44.670	30.159
stat	08	m2m3	1.464	1.855	1.929	3.151	45.698	29.733
02Hz	01	m2m3	0.801	0.811	1.660	2.142	35.414	27.164
02Hz	06	m2m3	1.487	1.043	1.975	2.808	49.560	26.188
02Hz	09	m2m3	1.669	1.181	2.091	3.158	55.120	22.214
02Hz	10	m2m3	1.339	1.491	1.877	3.307	50.827	25.234
02Hz	11	m2m3	1.524	1.188	2.152	2.753	47.828	25.977
02Hz	12	m2m3	1.811	1.581	1.914	3.267	53.127	23.849
02Hz	13	m2m3	2.141	1.362	2.113	3.091	54.430	20.301
05Hz	01	m2m3	2.006	0.658	1.904	2.964	63.119	12.405
05Hz	02	m2m3	1.011	0.561	1.641	2.510	53.420	15.879
05Hz	08	m2m3	1.252	1.056	1.877	3.206	51.166	23.053
05Hz	09	m2m3	1.904	0.851	2.055	3.164	58.119	17.314

Continued on next page

Supplementary Data S2: Data - bone dynamic, morphometric parameters in trabecular bone (continued)

Group	Mouse	Week	BFR [%/day]	BRR [%/day]	MAR [μm/day]	MRR [μm/day]	MS [%]	ES [%]
05Hz	10	m2m3	1.168	1.365	1.776	2.889	47.816	24.979
10Hz	01	m2m3	1.334	0.914	1.775	2.677	51.045	19.755
10Hz	02	m2m3	1.552	1.040	2.178	2.498	48.107	29.495
10Hz	04	m2m3	1.789	0.638	2.179	2.445	56.768	20.467
10Hz	05	m2m3	2.953	1.597	3.074	2.768	46.880	32.344
10Hz	06	m2m3	2.013	1.304	1.953	3.164	53.938	18.486
10Hz	07	m2m3	2.527	0.768	2.128	3.285	65.124	12.332
10Hz	08	m2m3	1.969	1.087	2.125	3.290	54.792	22.156
10Hz	09	m2m3	1.686	0.841	1.804	3.110	59.133	13.966
cont	02	m3m4	1.336	1.591	2.177	2.774	39.488	33.470
cont	03	m3m4	1.540	1.179	2.076	2.474	44.476	29.915
cont	04	m3m4	1.091	1.192	1.827	2.501	41.853	30.733
cont	05	m3m4	0.986	1.587	1.797	2.651	38.879	32.028
cont	06	m3m4	1.679	2.269	2.075	3.064	40.030	30.310
cont	07	m3m4	1.371	1.666	1.839	2.786	41.992	27.485
cont	08	m3m4	1.298	1.700	1.940	2.635	40.108	32.176
cont	09	m3m4	1.341	2.082	1.988	3.147	42.368	32.663
stat	01	m3m4	1.102	1.941	1.797	2.930	39.774	30.840
stat	02	m3m4	1.391	1.085	1.986	2.276	44.127	29.574
stat	03	m3m4	1.116	1.467	1.908	2.557	40.648	34.691
stat	04	m3m4	1.266	2.306	2.069	2.941	36.116	37.223
stat	05	m3m4	0.955	1.781	1.726	2.959	40.488	31.253
stat	06	m3m4	1.282	1.916	1.975	2.939	39.562	33.951
stat	07	m3m4	1.778	1.909	2.270	2.848	42.551	34.870
stat	08	m3m4	1.490	1.607	2.026	2.938	44.633	29.602
02Hz	01	m3m4	1.015	0.737	1.716	2.162	39.709	23.865
02Hz	06	m3m4	1.393	0.897	1.893	2.717	54.728	21.340
02Hz	09	m3m4	1.745	1.117	2.458	3.337	52.906	23.986
02Hz	10	m3m4	1.541	1.829	2.188	3.238	43.953	32.679
02Hz	11	m3m4	1.219	0.674	1.827	2.319	49.199	22.524
02Hz	12	m3m4	1.601	1.714	1.964	3.507	52.143	25.014
02Hz	13	m3m4	1.781	0.986	1.869	3.415	59.794	13.928

Continued on next page

Supplementary Data S2: Data - bone dynamic, morphometric parameters in trabecular bone (continued)

Group	Mouse	Week	BFR [%/day]	BRR [%/day]	MAR [μm/day]	MRR [μm/day]	MS [%]	ES [%]
05Hz	01	m3m4	1.427	0.699	1.724	3.007	61.449	13.821
05Hz	02	m3m4	1.019	0.555	1.719	2.211	50.103	19.894
05Hz	08	m3m4	1.080	0.819	1.789	2.573	49.988	23.204
05Hz	09	m3m4	1.809	0.776	2.151	2.840	57.710	20.234
05Hz	10	m3m4	1.319	1.313	1.814	3.093	51.770	21.998
10Hz	01	m3m4	1.926	0.837	2.154	2.584	54.374	21.393
10Hz	02	m3m4	1.701	0.897	2.274	2.434	50.987	27.924
10Hz	04	m3m4	1.560	0.711	2.190	2.504	54.607	22.962
10Hz	05	m3m4	1.377	0.530	1.791	2.127	52.760	19.397
10Hz	06	m3m4	2.172	1.170	1.981	3.307	61.215	16.469
10Hz	07	m3m4	2.012	1.225	2.285	3.592	56.172	22.131
10Hz	08	m3m4	1.350	0.955	1.786	3.385	57.490	19.313
10Hz	09	m3m4	1.680	0.771	1.996	2.619	54.017	21.388
cont	02	m4m5	2.109	1.503	2.538	2.882	46.229	32.266
cont	03	m4m5	1.836	0.991	2.341	2.333	46.206	28.595
cont	04	m4m5	1.649	1.596	2.334	2.642	41.732	35.412
cont	05	m4m5	1.582	1.799	2.237	2.783	41.307	33.494
cont	06	m4m5	1.853	3.286	2.191	3.694	38.425	32.343
cont	07	m4m5	1.300	1.448	1.817	2.643	43.044	26.906
cont	08	m4m5	1.037	1.525	1.834	2.736	38.544	30.735
cont	09	m4m5	1.121	1.523	1.838	2.640	40.680	31.710
stat	01	m4m5	1.649	2.094	2.107	3.020	43.510	30.138
stat	02	m4m5	1.167	1.163	1.956	2.372	41.971	30.095
stat	03	m4m5	0.663	1.505	1.696	2.412	33.105	37.844
stat	04	m4m5	1.285	2.393	1.906	3.147	40.534	30.914
stat	05	m4m5	1.299	2.211	2.004	3.496	42.051	30.746
stat	06	m4m5	1.557	2.497	2.282	3.194	37.421	35.798
stat	07	m4m5	1.144	1.936	1.884	2.907	39.379	33.036
stat	08	m4m5	1.221	1.767	1.869	3.169	44.276	29.186
02Hz	01	m4m5	1.145	1.107	1.742	2.465	42.238	25.454
02Hz	06	m4m5	0.829	0.649	1.660	2.440	48.777	21.637
02Hz	09	m4m5	1.276	1.011	2.065	3.170	52.182	24.346

Continued on next page

Supplementary Data S2: Data - bone dynamic, morphometric parameters in trabecular bone (continued)

Group	Mouse	Week	BFR [%/day]	BRR [%/day]	MAR [μm/day]	MRR [μm/day]	MS [%]	ES [%]
02Hz	10	m4m5	1.498	1.661	2.248	3.293	45.708	30.261
02Hz	11	m4m5	0.959	0.761	1.739	2.528	45.844	24.546
02Hz	12	m4m5	1.204	1.217	1.776	3.230	51.390	22.841
02Hz	13	m4m5	2.207	0.932	2.413	2.657	53.792	23.815
05Hz	01	m4m5	1.237	1.016	1.774	3.305	57.076	18.589
05Hz	02	m4m5	0.968	0.651	1.771	2.253	47.282	24.782
05Hz	08	m4m5	0.814	1.106	1.810	2.777	41.522	29.656
05Hz	09	m4m5	1.617	1.083	2.297	2.668	48.319	30.771
05Hz	10	m4m5	1.168	1.087	1.748	2.880	51.995	22.207
10Hz	01	m4m5	0.720	1.133	1.726	2.531	37.106	31.674
10Hz	02	m4m5	1.354	1.108	2.058	2.991	50.974	27.999
10Hz	04	m4m5	1.120	0.557	1.852	2.323	53.952	23.258
10Hz	05	m4m5	0.968	0.468	1.720	2.068	49.616	19.658
10Hz	06	m4m5	1.435	0.916	1.819	3.038	58.634	18.325
10Hz	07	m4m5	1.180	1.713	2.222	3.736	43.364	33.950
10Hz	08	m4m5	1.064	1.084	1.883	3.089	47.093	26.888
10Hz	09	m4m5	1.109	1.117	1.962	2.635	44.637	29.657

Supplementary Data S3: Data - bone morphometric parameters in cortical bone

Group	Mouse	Measurement	Tt.Ar [mm^2]	Ct.Ar [mm^2]	Ct.Ar/Tt.Ar [%]	Ct.Th [mm]
cont	02	m1	1.861	0.746	41.165	0.141
cont	03	m1	1.857	0.780	43.315	0.153
cont	04	m1	1.652	0.754	46.969	0.159
cont	05	m1	1.850	0.830	46.093	0.159
cont	06	m1	1.773	0.703	40.903	0.144
cont	07	m1	1.749	0.696	41.121	0.139
cont	08	m1	1.926	0.768	41.272	0.148
cont	09	m1	1.768	0.710	41.642	0.145
stat	01	m1	1.829	0.735	41.214	0.144

Continued on next page

Supplementary Data S3: Data - bone morphometric parameters in cortical bone (continued)

Group	Mouse	Measurement	Tt.Ar [mm^2]	Ct.Ar [mm^2]	Ct.Ar/Tt.Ar [%]	Ct.Th [mm]
stat	02	m1	1.777	0.754	43.741	0.150
stat	03	m1	1.870	0.839	45.781	0.158
stat	04	m1	1.793	0.739	42.390	0.144
stat	05	m1	1.935	0.806	42.924	0.150
stat	06	m1	1.805	0.741	42.209	0.145
stat	07	m1	1.718	0.675	40.727	0.140
stat	08	m1	1.807	0.725	41.533	0.147
02Hz	01	m1	1.736	0.720	42.629	0.146
02Hz	06	m1	1.847	0.762	42.466	0.145
02Hz	09	m1	1.719	0.755	45.167	0.157
02Hz	10	m1	1.697	0.718	43.864	0.147
02Hz	11	m1	1.646	0.717	44.968	0.149
02Hz	12	m1	1.773	0.754	43.412	0.150
02Hz	13	m1	1.915	0.760	40.883	0.143
05Hz	01	m1	1.877	0.710	39.015	0.135
05Hz	02	m1	1.935	0.824	43.767	0.153
05Hz	08	m1	1.792	0.746	42.989	0.148
05Hz	09	m1	1.721	0.617	37.527	0.126
05Hz	10	m1	1.918	0.804	43.045	0.147
10Hz	01	m1	1.851	0.724	40.304	0.139
10Hz	02	m1	1.804	0.826	47.014	0.160
10Hz	04	m1	1.893	0.858	46.403	0.159
10Hz	05	m1	1.771	0.802	46.482	0.155
10Hz	06	m1	1.728	0.701	41.794	0.139
10Hz	07	m1	1.667	0.614	38.556	0.132
10Hz	08	m1	1.926	0.797	42.888	0.155
10Hz	09	m1	1.706	0.691	41.885	0.148
cont	02	m2	1.865	0.750	41.341	0.142
cont	03	m2	1.866	0.799	44.117	0.156
cont	04	m2	1.652	0.757	47.122	0.161
cont	05	m2	1.854	0.824	45.709	0.159
cont	06	m2	1.789	0.694	39.975	0.142

Continued on next page

Supplementary Data S3: Data - bone morphometric parameters in cortical bone (continued)

Group	Mouse	Measurement	Tt.Ar [mm^2]	Ct.Ar [mm^2]	Ct.Ar/Tt.Ar [%]	Ct.Th [mm]
cont	07	m2	1.759	0.700	41.094	0.138
cont	08	m2	1.937	0.777	41.471	0.150
cont	09	m2	1.770	0.723	42.265	0.146
stat	01	m2	1.836	0.729	40.826	0.144
stat	02	m2	1.786	0.777	44.721	0.153
stat	03	m2	1.870	0.835	45.601	0.158
stat	04	m2	1.794	0.726	41.729	0.143
stat	05	m2	1.934	0.787	42.005	0.151
stat	06	m2	1.808	0.750	42.620	0.147
stat	07	m2	1.747	0.700	41.402	0.143
stat	08	m2	1.813	0.732	41.755	0.148
02Hz	01	m2	1.754	0.732	42.971	0.148
02Hz	06	m2	1.858	0.769	42.571	0.145
02Hz	09	m2	1.728	0.773	45.974	0.159
02Hz	10	m2	1.698	0.739	45.041	0.152
02Hz	11	m2	1.646	0.747	46.697	0.154
02Hz	12	m2	1.798	0.788	44.665	0.154
02Hz	13	m2	1.908	0.759	40.928	0.146
05Hz	01	m2	1.879	0.733	40.076	0.139
05Hz	02	m2	1.934	0.839	44.568	0.154
05Hz	08	m2	1.810	0.773	44.010	0.151
05Hz	09	m2	1.741	0.656	39.238	0.132
05Hz	10	m2	1.924	0.811	43.300	0.149
10Hz	01	m2	1.862	0.739	40.816	0.140
10Hz	02	m2	1.813	0.836	47.385	0.163
10Hz	04	m2	1.903	0.865	46.504	0.160
10Hz	05	m2	1.768	0.809	46.955	0.158
10Hz	06	m2	1.738	0.727	43.012	0.144
10Hz	07	m2	1.694	0.652	40.088	0.136
10Hz	08	m2	1.930	0.829	44.398	0.157
10Hz	09	m2	1.722	0.723	43.206	0.149
cont	02	m3	1.873	0.764	41.888	0.143

Continued on next page

Supplementary Data S3: Data - bone morphometric parameters in cortical bone (continued)

Group	Mouse	Measurement	Tt.Ar [mm^2]	Ct.Ar [mm^2]	Ct.Ar/Tt.Ar [%]	Ct.Th [mm]
cont	03	m3	1.867	0.804	44.334	0.157
cont	04	m3	1.667	0.768	47.368	0.162
cont	05	m3	1.864	0.820	45.279	0.158
cont	06	m3	1.797	0.682	39.059	0.141
cont	07	m3	1.784	0.707	40.973	0.139
cont	08	m3	1.942	0.781	41.543	0.151
cont	09	m3	1.788	0.735	42.458	0.147
stat	01	m3	1.847	0.731	40.732	0.146
stat	02	m3	1.796	0.795	45.430	0.156
stat	03	m3	1.896	0.846	45.602	0.158
stat	04	m3	1.800	0.708	40.698	0.142
stat	05	m3	1.953	0.792	41.814	0.150
stat	06	m3	1.820	0.753	42.460	0.147
stat	07	m3	1.747	0.719	42.436	0.146
stat	08	m3	1.826	0.750	42.456	0.150
02Hz	01	m3	1.752	0.734	43.112	0.148
02Hz	06	m3	1.868	0.790	43.458	0.150
02Hz	09	m3	1.748	0.796	46.696	0.163
02Hz	10	m3	1.715	0.765	46.134	0.156
02Hz	11	m3	1.662	0.761	47.064	0.156
02Hz	12	m3	1.827	0.807	45.065	0.159
02Hz	13	m3	1.931	0.801	42.529	0.153
05Hz	01	m3	1.897	0.769	41.593	0.143
05Hz	02	m3	1.939	0.859	45.435	0.158
05Hz	08	m3	1.812	0.799	45.344	0.159
05Hz	09	m3	1.752	0.695	41.131	0.138
05Hz	10	m3	1.941	0.827	43.804	0.152
10Hz	01	m3	1.873	0.760	41.671	0.144
10Hz	02	m3	1.815	0.851	48.129	0.166
10Hz	04	m3	1.905	0.885	47.412	0.165
10Hz	05	m3	1.787	0.815	46.778	0.158
10Hz	06	m3	1.765	0.758	44.164	0.150

Continued on next page

Supplementary Data S3: Data - bone morphometric parameters in cortical bone (continued)

Group	Mouse	Measurement	Tt.Ar [mm^2]	Ct.Ar [mm^2]	Ct.Ar/Tt.Ar [%]	Ct.Th [mm]
10Hz	07	m3	1.715	0.699	42.202	0.145
10Hz	08	m3	1.960	0.872	45.839	0.164
10Hz	09	m3	1.745	0.764	44.892	0.153
cont	02	m4	1.870	0.777	42.587	0.146
cont	03	m4	1.879	0.812	44.497	0.158
cont	04	m4	1.682	0.777	47.447	0.163
cont	05	m4	1.876	0.825	45.256	0.160
cont	06	m4	1.805	0.687	39.169	0.141
cont	07	m4	1.792	0.718	41.356	0.141
cont	08	m4	1.950	0.781	41.298	0.150
cont	09	m4	1.801	0.751	43.095	0.151
stat	01	m4	1.861	0.746	41.175	0.147
stat	02	m4	1.803	0.806	45.824	0.158
stat	03	m4	1.886	0.843	45.705	0.158
stat	04	m4	1.813	0.700	39.996	0.142
stat	05	m4	1.968	0.797	41.834	0.151
stat	06	m4	1.833	0.760	42.552	0.149
stat	07	m4	1.761	0.730	42.726	0.149
stat	08	m4	1.831	0.763	43.136	0.153
02Hz	01	m4	1.764	0.745	43.501	0.149
02Hz	06	m4	1.895	0.817	44.289	0.153
02Hz	09	m4	1.766	0.817	47.391	0.168
02Hz	10	m4	1.723	0.791	47.396	0.162
02Hz	11	m4	1.668	0.778	47.890	0.159
02Hz	12	m4	1.842	0.819	45.259	0.161
02Hz	13	m4	1.950	0.844	44.226	0.160
05Hz	01	m4	1.910	0.796	42.670	0.148
05Hz	02	m4	1.943	0.881	46.396	0.163
05Hz	08	m4	1.827	0.821	46.168	0.162
05Hz	09	m4	1.778	0.738	42.876	0.146
05Hz	10	m4	1.953	0.845	44.448	0.155
10Hz	01	m4	1.891	0.783	42.435	0.147

Continued on next page

Supplementary Data S3: Data - bone morphometric parameters in cortical bone (continued)

Group	Mouse	Measurement	Tt.Ar [mm^2]	Ct.Ar [mm^2]	Ct.Ar/Tt.Ar [%]	Ct.Th [mm]
10Hz	02	m4	1.834	0.871	48.666	0.168
10Hz	04	m4	1.933	0.911	48.030	0.170
10Hz	05	m4	1.792	0.836	47.812	0.160
10Hz	06	m4	1.780	0.789	45.558	0.156
10Hz	07	m4	1.736	0.737	43.876	0.154
10Hz	08	m4	1.973	0.896	46.742	0.169
10Hz	09	m4	1.772	0.791	45.715	0.158
cont	02	m5	1.885	0.784	42.586	0.147
cont	03	m5	1.895	0.820	44.477	0.158
cont	04	m5	1.684	0.779	47.463	0.163
cont	05	m5	1.867	0.828	45.580	0.162
cont	06	m5	1.819	0.682	38.604	0.141
cont	07	m5	1.794	0.728	41.828	0.143
cont	08	m5	1.958	0.790	41.657	0.151
cont	09	m5	1.805	0.756	43.266	0.152
stat	01	m5	1.870	0.755	41.429	0.149
stat	02	m5	1.824	0.830	46.644	0.163
stat	03	m5	1.886	0.832	45.140	0.157
stat	04	m5	1.819	0.700	39.785	0.141
stat	05	m5	1.947	0.782	41.480	0.150
stat	06	m5	1.825	0.757	42.562	0.150
stat	07	m5	1.765	0.737	42.954	0.150
stat	08	m5	1.838	0.768	43.271	0.154
02Hz	01	m5	1.780	0.762	44.089	0.153
02Hz	06	m5	1.905	0.839	45.146	0.155
02Hz	09	m5	1.786	0.826	47.363	0.170
02Hz	10	m5	1.738	0.805	47.758	0.165
02Hz	11	m5	1.683	0.801	48.785	0.163
02Hz	12	m5	1.861	0.832	45.538	0.161
02Hz	13	m5	1.975	0.867	44.850	0.164
05Hz	01	m5	1.927	0.816	43.291	0.154
05Hz	02	m5	1.949	0.897	47.120	0.166

Continued on next page

Supplementary Data S3: Data - bone morphometric parameters in cortical bone (continued)

Group	Mouse	Measurement	Tt.Ar [mm^2]	Ct.Ar [mm^2]	Ct.Ar/Tt.Ar [%]	Ct.Th [mm]
05Hz	08	m5	1.842	0.842	47.001	0.163
05Hz	09	m5	1.780	0.766	44.339	0.151
05Hz	10	m5	1.964	0.859	44.949	0.159
10Hz	01	m5	1.890	0.765	41.587	0.144
10Hz	02	m5	1.849	0.893	49.442	0.170
10Hz	04	m5	1.921	0.914	48.500	0.172
10Hz	05	m5	1.805	0.854	48.449	0.163
10Hz	06	m5	1.784	0.814	46.801	0.163
10Hz	07	m5	1.770	0.747	43.567	0.158
10Hz	08	m5	1.985	0.921	47.717	0.173
10Hz	09	m5	1.776	0.811	46.686	0.163